SANDIA REPORT
SAND2001-8108
Unlimited Release
Printed January 2001

High-Resolution Modeling of Multiscale Transient Phenomena in Turbulent Boundary Layers

Alan R. Kerstein, Rodney C. Schmidt, Scott Wunsch, William T. Ashurst, Vebjorn Nilsen, and Thomas D. Dreeben

Prepared by
Sandia National Laboratories
Albuquerque, New Mexico 87185 and Livermore, California 94550

Sandia is a multiprogram laboratory operated by Sandia Corporation, a Lockheed Martin Company, for the United States Department of Energy under Contract DE-AC04-94AL85000.

Issued by Sandia National Laboratories, operated for the United States Department of Energy by Sandia Corporation.

Available to DOE and DOE contractors from
U.S. Department of Energy
Office of Scientific and Technical Information
P.O. Box 62
Oak Ridge, TN 37831

Telephone: (865)576-8401
Facsimile: (865)576-5728
E-Mail: reports@adonis.osti.gov
Online ordering: http://www.doe.gov/bridge

Available to the public from
U.S. Department of Commerce
National Technical Information Service
5285 Port Royal Rd
Springfield, VA 22161

Telephone: (800)553-6847
Facsimile: (703)605-6900
E-Mail: orders@ntis.fedworld.gov
Online order: http://www.ntis.gov/ordering.htm

SAND01-8108
Unlimited Release
Printed January 2001

High-Resolution Modeling of Multiscale Transient Phenomena in Turbulent Boundary Layers

Alan R. Kerstein,[1] Rodney C. Schmidt,[2] Scott Wunsch,[1] William T. Ashurst,[1]
Vebjorn Nilsen,[3] and Thomas D. Dreeben[4]

Abstract

High fidelity numerical simulation of wall-bounded turbulence requires physically sound representation of the small scale unsteady processes governing near-wall momentum, heat, and mass transfer. Conventional wall treatments do not capture the diverse multiphysics flow regimes relevant to engineering applications.

To obtain a robust yet computationally affordable near-wall submodel for turbulent flow computations, the fine-grained spatial structure and time evolution of the near-wall flow is simulated using a model formulated on a 1D domain corresponding to the wall-normal direction. This approach captures the strong variation of flow properties in the wall-normal direction and the transient interactions between this highly inhomogeneous region and the more nearly homogeneous (at fine scales) flow farther from the wall.

The 1D simulation utilizes the One Dimensional Turbulence (ODT) methodology, whose formulation for the present application is described in detail. Demonstrations of ODT performance with regard to aspects of flow physics relevant to near-wall flow modeling are presented.

The coupling of ODT to a large eddy simulation (LES) of confined turbulent flow is described, and the performance of the coupled formulation is demonstrated. It is concluded that this formulation has the potential to provide the fidelity needed for engineering applications at an affordable computational cost.

[1] Reacting Flow Research Department, Sandia National Laboratories, Livermore, CA 94551

[2] Computational Sciences Department, Sandia National Laboratories, Albuquerque, NM 87185

[3] Torrex Equipment Corp., Livermore, CA 94550

[4] Osram Sylvania, Beverly, MA 01915

Acknowledgements

The authors would like to thank Jeff Baggett and Bill Cabot for providing the large-eddy-simulation code used in this work and for providing other assistance during their affiliation with the Center for Turbulence Research at Stanford University. This work was supported by the Laboratory Directed Research and Development (LDRD) program at Sandia National Laboratories.

Contents

1 Motivation

1.1 Current Modeling Capabilities and Needed Improvements

Computational modeling of turbulent flows has traditionally been based on ensemble or time averaging the governing equations. Reynolds-averaged Navier-Stokes (RANS) methods provide evolution equations for moments of the velocity field. Owing to the nonlinearity of the Navier-Stokes (NS) equations, these equations express the evolution of moments of given order in terms of moments of higher order, leading to an unclosed hierarchy of equations. This hierarchy is closed by modeling the unclosed terms at some level of the hierarchy.

It is widely recognized that steady-state RANS formulations omit large-scale unsteadiness that is a vital feature of many engineering and environmental flows. In many instances, it is important for flow models to capture time-resolved features because transient flow or thermochemical processes may impact system performance. Heat transfer, combustion, acoustics, multiphase couplings, and fluid-structure interactions are well-known examples of processes sensitive to flow transients.

For this reason, it has long been desirable to develop time-resolved models. Unsteady RANS formulations have been developed that capture the dominant unsteady features of some flows of interest.

A related but distinct development is the introduction of the large-eddy-simulation (LES) approach. This involves unsteady flow simulation with sufficient resolution (ideally) so that the flow scales that are not resolved presumably correspond to the regime of 'universal' flow behavior. Namely, the unresolved scales are assumed to consist of the inertial subrange of turbulence, and, at the finest scales, the viscous-dissipation subrange.

To the extent that this assumption is satisfied, it is hoped that a sufficient characterization of the universal flow properties below the resolution scale and their coupling to the resolved scales will ultimately provide a fundamentally sound basis for high fidelity turbulence modeling.

Significant process toward this goal has been achieved. However, there are several obstacles to the full achievement of this goal. It is widely recognized that foremost among these obstacles is the complexity and multiscale nature of turbulent flow interactions with boundary conditions imposed by walls (no-slip boundary conditions) or other surfaces (e.g., free-slip boundary condition for turbulent gas flow over a liquid surface).

The ideal case of a steadily forced turbulent boundary layer over a flat wall exhibits a universal structure embodied in the 'law of the wall.' This phenomenology has motivated the use of empirical wall functions in both RANS and LES models, with some degree of success. However, complex flows of practical interest do not conform to this ideal picture. Near-wall flows are subject to unsteady forcing and multiphysics processes (thermally induced property

variations, gravitational and other body forces, multiphase couplings, etc.) whose dynamical interactions with the bulk flow are not captured by currently available wall treatments. These complications arise also in the bulk flow, but in many instances their dominant influences are at large scales resolved by the computation and are thereby modeled adequately.

The particular difficulty of near-wall modeling arises because the dominant flow scale at a given distance from the wall is of the order of that distance, so all scales down to the viscous dissipation scale (below which turbulent motions are suppressed) become nonnegligible as the wall is approached. If fine scales are important near the wall and the dynamics of those scales depend on the details of the unsteady forcing and multiphysics processes, then both LES and RANS approaches face the challenge of adequately capturing these fine-scale processes and their coupling to the bulk flow. Success in this regard is important for reliable modeling of the bulk flow as well as modeling of near-wall processes *per se*.

A brute-force approach to this problem is to resolve all relevant near-wall scales in three dimensions (3D) by performing direct numerical simulation (DNS) in the near-wall region of the LES. The strategy adopted here is to capture, to the extent possible, the advantages of this approach while simplifying it so as to make it computationally affordable. The approach that is proposed achieves the needed spatial resolution in a lower dimensional formulation. To minimize the computational expense, a one-dimensional (1D) methodology is formulated. The details of this approach and its performance as a near-wall closure for LES are the subject of this report.

1.2 Modeling Strategy

The considerations outlined in Sec. 1.1 motivate the formulation of a fully resolved, unsteady, time-accurate 1D simulation of turbulent flow. Modeling assumptions needed to obtain a 1D formulation necessarily preclude an exact representation of 3D turbulence. The approximations that are introduced are guided by the intended use of the model. Recognizing that the model will not be quantitatively precise in all instances, the goal in formulating the model is to base it on physical principles that are robust, albeit empirical, within a framework that is general enough to incorporate turbulence interactions with diverse physical and chemical processes. It is hoped that this approach will yield a formulation that degrades gracefully as increasingly complex flows and/or multiphysics phenomena are addressed.

The 1D model may be viewed as a simulation of evolving profiles of flow velocity and fluid properties along a 1D line of sight through 3D turbulent flow. The 1D model domain is treated as a closed system, so that applicable conservation laws (mass, momentum, energy, and species) can be enforced. This is not locally accurate, because the physical line of sight is not a closed system. However, the 1D model is applied here to flows that are nearly homogeneous in directions normal to the line of sight, so the time-averaged properties of the

model are analogous to conventional boundary-layer approximations, as employed, e.g., in some 1D RANS formulations.

Specializing to solenoidal (incompressible) flow, the only continuous motion permitted in a closed 1D system is rigid translation of the entire domain. Therefore advection on the 1D domain is not based on motions prescribed by the velocity profile.

To motivate the ODT representation of vortical advection, Prandtl's application of the mixing-length concept to shear flow is considered. Denoting the wall-normal profile of streamwise velocity as $u(y)$, Prandtl represented turbulent advection effects as wall-normal fluid displacements of magnitude $l(y)$, where l is the local (in y) mixing length. These displacements do not change any properties of the fluid being displaced. In particular, the u value of a fluid element is invariant under displacement.

In general, displacements carry fluid to locations where the mean u value, denoted $\langle u \rangle$, differs from the u value of the fluid being displaced. The displacements thus introduce fluctuations of u at a given location. The associated fluctuations of u^2 (relative to $\langle u \rangle^2$) are interpreted as the turbulent kinetic energy of the u velocity component (here omitting constant multiplicative factors), and the displacements accordingly constitute a turbulent kinetic energy production mechanism.

In addition, the displacements transfer mean momentum, thereby representing turbulent transport of momentum. If $d\langle u \rangle/dy$ is positive, then equal-and-opposite upward and downward displacements will tend to induce a net downward displacement of u momentum. This is the momentum flux generated by motions parallel to the momentum gradient.

At this stage of the development, the mixing-length concept does not specifically imply the gradient-transport relation $J = -\rho\nu_e \nabla\langle u \rangle$, where J is the flux of mean u momentum and ν_e is a transport coefficient, termed the eddy viscosity. In fact, the mixing-length concept admits more general possibilities because it postulates direct interactions between y locations separated by a finite distance l. For example, the more general relation $J(y) = -\rho \int d\hat{y}\, \nu_e(y,\hat{y}) \nabla\langle u(\hat{y}) \rangle$, where $\nu_e(y,\hat{y})$ is a kernel (sometimes termed the 'spectral viscosity' in Fourier-space formulations), is likewise consistent with, and perhaps physically more faithful to, the mixing-length picture.

Thus, it is important to distinguish between the mixing-length concept and formal assumptions, such as gradient transport, that are often introduced on the basis of mathematical convenience rather than physical realism. The mixing-length concept in its general form is a suitable starting point for the introduction of ODT.

The mixing-length concept provides a framework for quantitative representation of coherent motions over finite distances within turbulent flow. Any such motion is characterized by a length scale l and a time scale τ that can be interpreted as either its time duration or the characteristic time between motions of the given type. In the derivation of RANS and other conventional models, and also in ODT, these motions are treated for modeling

purposes as instantaneous displacements. In RANS models, this assumption is not readily apparent owing to the ensemble averaging that is applied in deriving the final formulation. ODT is a time-resolved simulation, so details of the displacement mechanism are central to the method.

As noted, gradient transport is a simplifying assumption often adopted within the mixing-length framework. It is not universally adopted, as illustrated by the more general spectral viscosity approach (as well as other generalizations not mentioned here). Another key assumption that is widely, though not universally, adopted is that there is a single mixing length l and mixing time τ, i.e. a single relevant coherent motion, at any given location (in steady-state models) or at any given location and time (in unsteady RANS and LES models). An alternative to this assumption in a RANS context is spectral transport modeling, which is in a developmental stage.

The single-scale assumption is another convenient simplification that is not dictated by the underlying physics, hence the effort to develop a more general approach. Even for cases in which this assumption is reasonable, the known physics of turbulent flow often does not uniquely specify the parameter dependencies of l.

There are many notable examples of successful turbulence modeling based on gradient transport and/or the single-mixing-length assumption. For example, Prandtl's assumption that l and τ^{-1} scale as y and $d\langle u(y)\rangle/dy$, respectively, in the flat-plate boundary layer was the foundation of the present-day law of the wall.

The approach adopted in ODT is faithful to the mixing-length concept but involves minimal additional simplifications. The justification for this approach is that the mixing-length concept, despite its *ad hoc* nature, has proven to be a robust conceptual tool for turbulence modeling. Its main limitation is that it is typically applied in a manner that requires the introduction of flow-specific assumptions, resulting in the proliferation of models that are limited in scope. Here, a formulation is sought that captures the efficacy of the mixing-length concept while avoiding narrowly based assumptions that might constrain its applicability.

These considerations anticipate some features of ODT that are elaborated in Sec. 2. First, vortical advection is represented by instantaneous events, each characterized by a location y_0 on the 1D domain, a size l, and a time scale τ characterizing the frequency of the event type. Second, each event generates fluid displacements that obey all applicable conservation laws. Third, the model admits every event location and size permitted by the boundary conditions, and therefore does not require the designation of a unique l value at given y_0.

Within this modeling framework, it may turn out that a dominant scale l can be identified for each y_0, and that the dependence of the dominant scale on y_0 has a simple form. If this turns out to be the case, then ODT may help identify simpler formulations applicable to particular flows. It is emphasized, however, that this simplification would be an outcome of the model rather than a predetermined input to ODT.

2 Near-Wall Model Formulation

2.1 Overview

Since it was first introduced, ODT has undergone an evolutionary development process. Here, the formulation adopted in Sec. 5 as a near-wall momentum closure for LES is described. Some of the model demonstrations presented in Sec. 4 predate this formulation. The differences among formulations and their impact on computed results are discussed in the context of specific applications.

Operationally, ODT defines initial-value problems for a three-component vector velocity field $v_i(y)$ on a 1D spatial domain, denoted the y coordinate. (Consistent with boundary-layer nomenclature, v_2 corresponds to motion in the y direction.) Scalar fields $\theta(y)$, representing thermodynamic quantities, species concentrations, etc., may also be included. The numerical method consists of a conventional time-stepping solution of partial differential equations representing viscous dissipation and any other molecular processes that are included (such as diffusion of scalars θ), punctuated by a random sequence of instantaneous events representing individual turbulent eddies. This computed evolution may be viewed as a sequence of initial-value problems, each running from a given eddy event until the next one, with each eddy creating a modified starting condition for subsequent time evolution. The molecular evolution equations used here are

$$\left(\partial_t - \nu\partial_y^2\right) v_i(y,t) = 0 \tag{1}$$

$$\left(\partial_t - \kappa\partial_y^2\right) \theta(y,t) \; = 0, \tag{2}$$

where ν is the kinematic viscosity and κ is the diffusivity of the property θ. The model accommodates multiple species, multicomponent diffusion, and variable properties, including density variations, but these extensions are not considered here.

ODT is a stochastic model because the eddy events are determined by a random sampling procedure. When ODT is used to simulate a time-developing flow, statistics are gathered by running multiple realizations to form ensemble averages. For statistically stationary flows, statistics can be gathered by running a single realization and time averaging during the statistically stationary evolution that follows relaxation of initial transients.

The mathematical operations that constitute eddy implementation are specified (Sec. 2.2), and then the rules governing the random sampling of events are formulated (Secs. 2.3 and 2.4). Finally (Sec. 2.5), statistical analysis and physical interpretation of computed quantities are discussed.

2.2 Eddy Implementation

The mathematical operations that comprise an eddy event can be represented symbolically as

$$\begin{aligned} v_i(y) &\rightarrow v_i(f(y)) + c_i K(y) \\ \theta(y) &\rightarrow \theta(f(y)). \end{aligned} \tag{3}$$

Here and below, the argument t of v_i and functions of v_i is suppressed.

Equation (3) indicates that fluid properties at location $f(y)$ prior to the eddy are mapped to location y, corresponding to fluid displacement $y - f(y)$. In addition, a kernel $K(y)$ with a multiplicative coefficient c_i is added to $v_i(y)$. Before specifying the assumed forms of $f(y)$ and $K(y)$, the motivation for this eddy formulation is explained.

In keeping with the mixing-length concept, the eddy event includes a mapping operation that displaces fluid in a manner that is consistent with conservation laws and other requirements. The key requirement is that any y interval must be mapped into an an interval or collection of intervals of the same total length, thereby enforcing incompressibility in the closed 1D system. Mathematically, the mapping is required to be measure-preserving. This property assures global conservation of fluid properties, including arbitrary powers of velocity.

The additive terms $c_i K(y)$ incorporate a physical mechanism that is not reflected in the mixing-length picture of property-invariant fluid displacements. Namely, pressure gradients acting on the velocity vector during eddy motion can reorient the vector, thereby redistributing flow kinetic energy among the velocity components. This pressure-scrambling mechanism has been incorporated into second-order RANS closures through the introduction of the return-to-isotropy concept (Pope 2000). It is assumed that random eddy motions reduce flow anisotropy because they reorient fluid in a manner that does not depend on the forcings or boundary conditions that cause anisotropy. Subject to the constraint of energy conservation, return to isotropy is incorporated into ODT by choosing the amplitudes c_i in the additive terms so that the component energies

$$E_i \equiv \frac{\rho_0}{2} \int dy\, v_i^2(y), \tag{4}$$

where ρ_0 is the fluid density (here assumed constant), tend to be equalized. (In the present 1D formulation, ρ_0 is defined as mass per unit length. Conventional units can be recovered by defining the model domain to be a pencil with fixed cross-sectional area and no property variations in the cross-sectional plane.) Momentum conservation is enforced by requiring $K(y)$ to obey $\int dy\, K(y) = 0$.

Within the stated constraints, there is considerable latitude in the choice of the functions $f(y)$ and $K(y)$ and coefficients c_i. The specific choices and their motivations are presented

next. Provided that these quantities satisfy the stated constraints and other physical requirements that are noted, it is likely that the trends and features of the computed results are insensitive to the specific choices, and that sensitivity of quantitative predictions to the choices is largely subsumed in the adjustment of model parameters. Adjustable parameters are introduced in the eddy selection process (Sec. 2.3).

The function $f(y)$ is taken to be the triplet map,

$$f(y) \equiv y_0 + \begin{cases} 3(y-y_0) & \text{if } y_0 \le y \le y_0 + \frac{1}{3}l, \\ 2l - 3(y-y_0) & \text{if } y_0 + \frac{1}{3}l \le y \le y_0 + \frac{2}{3}l, \\ 3(y-y_0) - 2l & \text{if } y_0 + \frac{2}{3}l \le y \le y_0 + l, \\ y - y_0 & \text{otherwise.} \end{cases} \tag{5}$$

The triplet map was originally introduced in the linear-eddy model (LEM), the antecedent of ODT (Kerstein 1991). It induces nonzero displacements only within the y range $[y_0, y_0 + l]$. The eddy parameters y_0 (nominal eddy location) and l (nominal eddy size) are determined for a given event by selection process described in Sec. 2.3.

The triplet map shrinks the interval $[y_0, y_0 + l]$ to a third of its original length and places three copies in the original interval. The middle copy is reversed, so that the mapping does not introduce discontinuities into any field defined on y.

The physical interpretation of the triplet map has been discussed in detail (Kerstein 1991, Kerstein 1999). Salient features are (*i*) the multiplicative increase of property gradients, analogous to vortical strain effects ('vortex stretching') in turbulence, (*ii*) wrinkling of initially monotonic property profiles, introducing the 1D analog of flame wrinkling and consequent flame-flame interactions in combusting flows, and (*iii*) a 1D analog of vortical overturning and consequent mixing enhancement by turbulence. These features are interrelated, and in fact, their common mechanistic origins facilitate the concise representation of a turbulent eddy by the triplet map.

The kernel $K(y)$ in Eq. (3) is taken to be $K(y) \equiv y - f(y)$, i.e., the y profile of displacements induced by the triplet map. This is a convenient form that obeys the applicable conservation laws and introduces no discontinuities when implemented in Eq. (3).

Additional modeling is required to determine the pressure-scrambling amplitudes c_i. Based on substitution of the identity $\int dy\, K^2(y) = \frac{4}{27} l^3$ and the definition

$$v_{i,K} \equiv \frac{1}{l^2} \int dy\, v_i(f(y)) K(y) = \frac{4}{9l^2} \int_{y_0}^{y_0+l} dy\, v_i(y)[l - 2(y-y_0)] \tag{6}$$

(where the rightmost expression follows from the definitions of $f(y)$ and $K(y)$) into Eq. (4),

the change in the kinetic energy of component i due to eddy implementation is

$$\Delta E_i = \frac{1}{2}\rho_o \int dy \ \left[(v_i(f(y)) + c_i K(y))^2 - v_i(y)^2\right] = \rho_o l^2 c_i \left(v_{i,K} + \frac{2}{27} l c_i\right). \tag{7}$$

The requirement $\sum_i \Delta E_i = 0$ implies only one constraint on the three amplitudes c_i.

An additional constraint arises by requiring invariance under exchange of indices in order to satisfy reference frame invariance. With these constraints, the kinetic energy changes imposed on the velocity components must be of the form

$$\Delta E_i = \alpha \sum_j T_{ij} Q_j \tag{8}$$

where Q_j (j = 1, 2, or 3) is a quantity with units of energy that depends on $v_j(y)$ and scalars, α is a free parameter, and the transfer matrix T is defined by

$$T \equiv \frac{1}{2} \begin{pmatrix} -2 & 1 & 1 \\ 1 & -2 & 1 \\ 1 & 1 & -2 \end{pmatrix}. \tag{9}$$

This matrix is constructed to obey energy conservation ($\sum_i \Delta E_i = 0$) and to be invariant under permutation of indices. These requirements uniquely define T except for an arbitrary multiplicative constant, which is absorbed in the parameter α. Using Eq. (7), the amplitudes c_i are determined by the choice of the quantities Q_i and the value of α. Here, α is a transfer coefficient that specifies the fraction of Q_i that is redistributed to the other components.

Specification of Q_i is guided by the conceptual framework of the ODT model. Because each eddy event is meant to represent the local physics of turbulence on a single length scale (the mapping size l), Q_i should be a local measure of the turbulent kinetic energy of velocity component v_i on that length scale. The pressure-scrambling mechanism would then redistribute some of this energy among the three components. A natural choice arises when one considers the specific mathematical structure of the operations defined in Eq. (7). While addition of $c_i K(y)$ to v_i makes it possible to add an arbitrarily large quantity of energy, only a finite amount may be removed. The maximum value of $-\Delta E_i$ based on Eq. (7) is denoted the 'available kinetic energy' of v_i, because it indicates the maximum amount of energy which may be removed from v_i by this method.

The available energy concept arises in other contexts, such as the thermodynamic concept of available work (Callen 1960) and the available potential energy concept applied to density-stratified flow (Lorenz 1955). Here it introduced as a model construct, motivated as follows. Energy transfers associated with an eddy motion of given size are assumed to be governed by velocity fluctuations of comparable size. This assumption is analogous to the commonly assumed locality, in wavenumber space, of energy transfers in the turbulent cascade. The

function $K(y)$ introduced in Eq. (3) concisely embodies this scale locality principle by assuring that (i) the scale of velocity fluctuations induced by energy transfers is comparable to the eddy size, (ii) fluctuations that determine the energy available for transfer, based on Eq. (7), are of comparable size, and (iii) scale locality is likewise incorporated into the eddy selection process (Sec. 2.3).

Therefore Q_i is taken to be the available kinetic energy of v_i determined by maximization of $-\Delta E_i$, giving

$$Q_i \equiv \frac{27}{8}\rho_o l v_{i,K}^2. \tag{10}$$

Using this choice of Q_i, the exchange amplitudes are given by

$$c_i = \frac{27}{4l}\left(-v_{i,K} + \mathrm{sgn}(v_{i,K})\sqrt{v_{i,K}^2 + \alpha\sum_j T_{ij} v_{j,K}^2}\right). \tag{11}$$

The solution is guaranteed to be real for $0 \leq \alpha \leq 1$. Because Q_i is the maximum energy available for exchange, the physical model requires the transfer coefficient to fall within this range.

Unless otherwise noted, α is set equal to $2/3$, corresponding to equalization of component available energies. This reflects the intuitive notion that an eddy turnover erases memory of fluid orientation in any fixed reference frame, so there should be no bias in the post-eddy distribution of available energy among velocity components that reflects the distribution prior to the turnover. This may be an overly literal interpretation of the correspondence between ODT eddy events and eddies in turbulent flow, so other values of α should not be ruled out *a priori*.

In Eq. (11), the sign ambiguity in the solution to the quadratic equation for c_i is resolved by requiring that $c_i \to 0$ as $\alpha \to 0$. Velocity components that are initially zero everywhere are seeded with small initial random perturbations to prevent sign ambiguities in these components. The perturbations are symmetric about zero, assuring that these components have zero mean.

2.3 Eddy Selection

The final ingredient required in the model is the determination of the sequence of eddy mappings, parameterized by position y_0 and size l, that should take place. An estimated time scale $\tau(y_0, l)$ for each mapping is based on the eddy turnover time as determined from the velocity profiles $v_i(y,t)$. In real turbulence, this is roughly the time required for an eddy to mix a region of size l. In ODT, eddy events are implemented instantaneously, but should occur with frequencies comparable to the turnover frequencies of corresponding eddies.

For a quantititive definition of τ, a measure of the turbulent kinetic energy associated with each possible mapping interval is employed. The most general dimensionally consistent

form for the time scales $\tau(y_0, l)$ is

$$\frac{\rho_o l^3}{\tau^2} \sim \sum_j B_j Q_j \tag{12}$$

where B_j are arbitrary dimensionless constants, and the quantities Q_j are again some measure of energy in the velocity components. Here again, Q_j is taken to be the available kinetic energy of component j, based on the same considerations as in Sec. 2.2. Because eddy events represent motion in the y direction, the quantities B_j are chosen so that the right-hand side of Eq. (12) corresponds to the available kinetic energy in component v_2 (the y velocity component) upon completion of eddy implementation. Based on Eqs. (8)-(10), this yields

$$\left(\frac{l}{\tau}\right)^2 \sim v_{2,K}^2 + \alpha \sum_j T_{2j} v_{j,K}^2. \tag{13}$$

This choice breaks the symmetry under index exchange only in determining the sequence of mappings, while maintaining it during the implementation of each individual eddy mapping event.

There is one additional consideration in determining τ. Due to the damping effects of viscosity, very small eddies should not occur. Any eddy with a time scale much longer than the corresponding viscous time scale $\tau_\nu \sim l^2/\nu$ for that eddy size should be prohibited. This suggests including a 'viscous penalty' in the relation determining the eddy turnover time. The eddy time scale, with the viscous penalty, is then governed by

$$\left(\frac{l}{\tau}\right)^2 \sim v_{2,K}^2 + \alpha \sum_j T_{2j} v_{j,K}^2 - Z\frac{\nu^2}{l^2}. \tag{14}$$

The constant of proportionality Z in the viscous penalty is an order-unity parameter of the model. For most applications, computed results are insensitive to Z for sufficiently small Z because transport by marginally allowed eddies becomes negligible compared to viscous transport due to the concurrent molecular evolution, Eq. (1). Thus, Z can be either a physical parameter or a numerical parameter used to eliminate small, inconsequential events.

In Eq. (14), the available energy is evaluated at the completion of eddy implementation in order to incorporate several relevant energy transfer processes. For example, consider a flow with a spatially varying v_1 or v_3 profile but v_2 identically zero. Then intercomponent energy transfer is the only source of available energy, and this transfer, if it occurs, corresponds to the onset of higher-dimensional motion. This raises the possibility (not yet investigated in detail) that the present formulation may encompass the transition to turbulence as well as fully developed turbulence.

A model generalization discussed in Sec. 4 is the incorporation of buoyancy. If the ODT domain is vertically oriented, then triplet mapping of a variable-density interval induces a potential-energy change that implies to an equal-and-opposite change of v_2 kinetic energy. To

simulate the onset of turbulence in a quiescent, unstably stratified fluid, the available energy must again be evaluated after energy exchange, or there will be no identified energy source to drive the flow. Likewise, the inhibiting effect of stable stratification is captured by evaluating the available energy at eddy completion; to do otherwise might lead to energetically forbidden motions.

As in the previous versions of ODT, the time scales τ for all possible eddies are translated into an event rate distribution λ, defined as

$$\lambda(y_0, l; t) \equiv \frac{C}{l^2 \tau(y_0, l; t)} = \frac{C\nu}{l^4} \sqrt{\left(\frac{v_{2,K} l}{\nu}\right)^2 + \alpha \sum_j T_{2j} \left(\frac{v_{j,K} l}{\nu}\right)^2 - Z} \tag{15}$$

using (14) for the turnover time. If the right-hand side of Eq. (14) is negative, the eddy is deemed to be suppressed by viscous damping and λ is taken to be zero for that case. In the square-root term of Eq. (15), the quantities preceding Z involve groups that have the form of a Reynolds number. Z can be viewed in this context as a parameter controlling the critical Reynolds number for eddy turnover. This Reynolds-number threshold is conceptually (though not necessarily quantitatively) related to the threshold for transition to turbulence (Kraichnan 1962).

The foregoing construction of the ODT eddy rate involves three free parameters: C, α, and Z. The overall rate constant C determines the strength of the turbulence in the model; hence it determines the Reynolds number Re or equivalent measures of turbulence intensity. The transfer coefficient α determines the degree of kinetic energy exchange among components. For $\alpha = 0$ (no exchange), this formulation reduces to a specialization of the buoyant stratified flow model of Wunsch & Kerstein (2001) to constant density flows (see Sec. 4). The small-scale cutoff parameter Z determines the smallest eddy size for given local strain conditions.

The sequence of eddies implemented during a simulated realization is sampled from the rate distribution λ. During a time increment dt, the probability of occurrence of an eddy whose location and size are within the ranges $[y_0, y_0 + dy_0]$ and $[l, l + dl]$ respectively is $\lambda(y_0, l; t)\, dy_0\, dl\, dt$.

Each event, as well as the viscous evolution, Eq. (1), between events, changes the velocity profiles v_i and therefore modifies the rate distribution λ. This interaction between the rate distribution and simulated flow evolution is largely responsible for key features of the model such as emulation of the inertial-range turbulent cascade (Kerstein 1999, Wunsch & Kerstein 2001). From a computational viewpoint, it causes explicit construction of, and sampling from, the rate distribution to be unaffordable owing to the need to reconstruct this distribution repeatedly. Instead, an indirect but mathematically equivalent procedure is employed, as explained in Sec. 3.3.

2.4 Large-Eddy Anomaly

For time-developing flows, the statistical sampling procedure used in ODT introduces an artifact associated with the occasional selection of an event much larger than the momentum thickness (or equivalent characteristic size) of the flow. These events are rare because the dimensional scalings underlying the method are consistent with scale locality (i.e., events of given size are driven most effectively by forcings of comparable scale). However, the rare large events permitted by the statistical sampling procedure contribute disproportionately to transport, which scales as the square of the event size. Thus, they can dominate transport, and potentially introduce spurious divergences.

Several ways of mitigating this artifact have been employed previously (Kerstein 1999, Kerstein & Dreeben 2000). Here, a large-eddy suppression mechanism is introduced that is physically motivated, parameter free, and broadly applicable.

To suppress rare large events, the rate λ for a given event is evaluated two different ways, and the smaller of the two results is used in the sampling procedure outlined in Sec. 2.3. One evaluation is by the method already described in Sec. 2.3, based on Eq. (15). The other evaluation involves replacement of each velocity profile $v_i(y,t)$ by a profile that is linear in y, and evaluation of Eq. (15) based on these linear profiles. The slope of each profile is taken to be the median value of $|dv_i/dy|$ within the eddy range $[y_0, y_0 + l]$.

The key attribute of this procedure is that it assigns a zero rate to any event for which each velocity profile is flat (zero slope) in more than half of the eddy range. Thus, an event encompassing a y interval that is more than twice the width of the active zone of an entraining shear flow is strictly excluded. The median of absolute slope is used in order to avoid a balance of positive and negative values that would result in a zero median for events whose exclusion is not intended. In addition to preventing unphysically large eddies, this procedure reduces the likelihood of events whose available energy is dominated by contributions from a small subinterval of the eddy range. Thus, the procedure further enforces scale locality, which is the conceptual basis of ODT.

The median procedure could be used as a replacement, rather than an augmentation, of the procedure of Sec. 2.3. However, the model is internally most consistent if the true profiles, which must be used in eddy implementation (mapping and energy exchange), are also used in eddy selection. The median procedure as implemented can only reduce the likelihood of a given event, consistent with the objective of excluding certain events with minimal modification of other aspects of the model.

2.5 Statistical Properties of Flow Realizations

ODT is formulated as a closed system on a 1D domain. The model can be viewed as a simulation of a 1D line of sight in a 3D flow. However, such a line of sight is not a closed

system. Modeling it as a closed system is an artifact that may be the cause of some of the discrepancies between model predictions and measured turbulence properties. However, it is unlikely that this is the most severe approximation within the model.

A key benefit of taking the 1D domain to be a closed system is that conservation laws can be enforced. The measure-preserving property of the triplet map enforces conservation of mass. In fact, this property assures that the triplet map conserves all domain-integrated quantities, including velocity moments of all orders. The pressure-scrambling mechanism is formulated so as to conserve momentum and total energy while redistributing energy among velocity components. Viscous dissipation, implemented in a conventional manner, removes kinetic energy while conserving momentum.

Accordingly, momentum and energy budgets can be formulated for ODT that are broadly analogous to the usual relations based on the Navier-Stokes equations. Here, ODT budgets are formulated both to refine the analogy to Navier-Stokes turbulence and to provide operational definitions of relevant flow statistics.

For this purpose, a notional instantaneous evolution equation is written for ODT as follows:

$$\frac{\partial v_i}{\partial t} = \nu \frac{\partial^2 v_i}{\partial y^2} + M_i + K_i. \tag{16}$$

This equation formally represents the three processes that can change the value of v_i at a given location y and time t. The viscous term has its usual form. M_i and K_i represent changes induced by triplet-map and and pressure-scrambling operations, respectively. For example, if a triplet map at time t_0 replaces the v_i value at given y, denoted $\hat{v}_i$, by a new value $\tilde{v}_i$, then $M_i(y) = (\tilde{v}_i - \hat{v}_i)\delta(t - t_0)$. The formal definition of K_i is analogous, with $\hat{v}_i$ and $\tilde{v}_i$ now evaluated before and after the pressure-scrambling operation. Numerical implementation of statistical data analysis is based on ensemble-averaged equations derived from Eq. (16).

Before averaging Eq. (16), the role of K_i in the context of momentum and energy balances is considered. Though the kernel addition (Sec. 2.1) during eddy implementation is intended to incorporate pressure-scrambling effects, this operation may be interpreted formally as a combination of scrambling and transport contributions to balance equations. In particular, a given kernel-induced change $K_i(y)$ may reflect energy and momentum transfers to other velocity components (scrambling) and/or to the same velocity component at other spatial locations (transport). Accordingly, K_i is expressed as a sum, $K_i = S_i + T_i$, of scrambling and transport contributions.

The kernel K is defined so that $\int K\, dy = 0$ so that the pressure-scrambling operation conserves momentum. Accordingly, for a given eddy $\int K_i\, dy = 0$. The transport contribution T_i should be defined so that its integral is zero, because it represents i-component momentum transfer along the y coordinate and therefore is not a net momentum source or sink for this component. These integral constraints are satisfied only if $\int S_i\, dy = 0$.

The latter result does not uniquely define S_i, but the choice $S_i \equiv 0$ is clearly preferred

because it corresponds to the absence of a pressure-scrambling contribution to the ODT mean momentum equation, in accordance with the absence of pressure scrambling in the Navier-Stokes mean momentum equation. In fact, this equation lacks any pressure-fluctuation terms, so T_i should not be regarded as a pressure-transport contribution. Rather, M_i and T_i together determine the ODT analog of mean advective transport.

The ODT mean momentum equation is obtained by taking the ensemble average of Eq. (16). Substituting T_i for K_i, this gives

$$\frac{\partial}{\partial t}\langle v_i \rangle = \nu \frac{\partial^2}{\partial y^2}\langle v_i \rangle + \langle M_i \rangle + \langle T_i \rangle, \tag{17}$$

which may be compared to the constant density Navier-Stokes mean momentum equation for planar time-developing flow (Moser *et al.* 1998),

$$\frac{\partial}{\partial t}\langle v_1 \rangle = \nu \frac{\partial^2}{\partial y^2}\langle v_1 \rangle - \frac{\partial}{\partial y}\langle v_1' v_2' \rangle, \tag{18}$$

where $v_i' \equiv v_i - \langle v_i \rangle$. (Owing to planar symmetry, $\langle v_2 \rangle$ and $\langle v_3 \rangle$ are identically zero.) The comparison identifies the ODT analog of the Reynolds-stress component $\langle v_1' v_2' \rangle$ for this class of flows. Assuming an infinite domain with a turbulent zone of finite lateral extent, $\langle v_1' v_2' \rangle = 0$ at $y = \infty$, so at any location y^*, Eqs. (17) and (18) give

$$\langle v_1'(y^*) v_2'(y^*) \rangle = \int_{y^*}^{\infty} dy \, (\langle M_1 \rangle + \langle T_1 \rangle) \equiv I_1(y^*). \tag{19}$$

The notation $I_i(y^*)$ is introduced in order to distinguish the operational evaluation of $\langle v_i'(y^*) v_2'(y^*) \rangle$ in ODT from the conventional Navier-Stokes definition of this quantity. (Generalization of the derivation of Eq. (19) to $i \neq 1$ is straightforward.) Equation (19) is likewise applicable if the upper bound of the integral is any finite y value at which $\langle v_1' v_2' \rangle = 0$, e.g., at a wall.

Equation (18) is consistent with the physical interpretation that $\langle v_1'(y^*) v_2'(y^*) \rangle$ represents the rate of increase of $\int_{y^*}^{\infty} dy \, v_2(y^*)$ due to turbulent transfer of the v_1 velocity component across $y = y^*$. The terms on the right-hand size of Eq. (19) are the contributions of the ODT turbulent transfer mechanisms to this integral.

Operationally, these contributions are evaluated by gathering statistics from ODT realizations in finite time bins. Omitting for now the viscous contribution, Eq. (17) implies that the mean velocity increment over a time increment Δt is

$$\langle \Delta v_1 \rangle = \langle M_1 \Delta t \rangle + \langle T_1 \Delta t \rangle, \tag{20}$$

where $M_1 \Delta t$ and $T_1 \Delta t$ are determined, for a given realization, by summing the respective Δv_1 contributions over all eddies occurring during the designated time interval. This summation is performed separately at each location y, though the y argument has been suppressed in the analysis. An average of these contributions over an ensemble of realizations yields $\langle \Delta v_1 \rangle$.

Dividing by Δt, a discrete-time estimate of the advective terms on the right-hand side of Eq. (17), specialized to $i = 1$, is obtained. Substitution into Eq. (19) then yields the ODT analog of $\langle v_1' v_2' \rangle$.

This result is different from what would be obtained by evaluating $\langle v_1' v_2' \rangle$ based on ODT velocity profiles v_1 and v_2. ODT velocities do not literally advect fluid, so their use in this way would not be physically meaningful. However, ODT is formulated so that energetics based on these profiles are meaningful. In particular, budgets of the component contributions, $\langle v_i'^2 \rangle$, to the turbulent kinetic energy are analogous to their Navier-Stokes counterparts. Flux terms within these budgets must be evaluated, as in the derivation of Eq. (19), based on the conservation laws obeyed by ODT.

Therefore the ODT budget of $\langle v_i'^2 \rangle$ is obtained by first reconsidering Eq. (16). The usual approach is to multiply this equation by v_i, average, and then combine the result with $\langle v_i \rangle$ times Eq. (17) to obtain an evolution equation for $\langle v_i'^2 \rangle$. However, this approach is again inapplicable to the advective terms because of the limited role of the velocity profiles in ODT. Therefore the appropriate starting point is the formal equation

$$\frac{\partial v_i^2}{\partial t} = 2\nu v_i \frac{\partial^2 v_i}{\partial y^2} + M_{ii} + K_{ii}, \tag{21}$$

where M_{ii} and K_{ii} represent the effects of the triplet-map and pressure-scrambling operations, respectively, on v_i^2 at given y. For the illustrative case below Eq. (16), $M_{ii}(y) = (\tilde{v}_i^2 - \hat{v}_i^2)\delta(t - t_0)$, and the evaluation of K_{ii} is analogous.

K_{ii}, like K_i, is expressed as a sum of scrambling and transport contributions, $K_{ii} = S_{ii} + T_{ii}$. For a given eddy, transport by definition conserves v_i^2 globally, so $\int T_{ii}\, dy = 0$. Unlike K_i, K_{ii} is not globally conserved, so $\int K_{ii}\, dy$ is nonzero in general. S_{ii} is not uniquely defined, though its dy-integral for a given eddy is unique. We choose to define S_{ii} within an eddy as its eddy average, $S_{ii} = \frac{1}{l} \int K_{ii}\, dy$. Though arbitrary, this choice does not have a significant impact on computed results because it only affects the spatial distribution of scrambling within an eddy subject to the integral constraint.

It was noted that T_i should not be interpreted as a pressure-transport effect although it is based on the model subprocess that nominally represents pressure-fluctuation effects. Likewise, T_{ii} is not specifically a pressure-transport effect, although the $\langle v_i'^2 \rangle$ budget, unlike the $\langle v_i \rangle$ budget, has a pressure-transport as well as a turbulent transport term. The sum of M_{ii} and T_{ii} contributions can be interpreted as the ODT analog of the sum of Navier-Stokes pressure-transport and turbulent transport terms, but the M_{ii} and T_{ii} contributions cannot be decomposed consistently into the individual Navier-Stokes terms. Therefore the advective transport term of the $\langle v_i'^2 \rangle$ budget combines these two terms.

The ODT evolution equation for $\langle v_i^2 \rangle$ is

$$\frac{\partial}{\partial t}\langle v_i^2 \rangle = \nu \frac{\partial^2}{\partial y^2}\langle v_i^2 \rangle - 2\nu \left\langle \left(\frac{\partial v_i}{\partial y} \right)^2 \right\rangle + \langle M_{ii} \rangle + \langle T_{ii} \rangle + \langle S_{ii} \rangle, \tag{22}$$

where the viscous contribution has been rearranged in the usual manner. To obtain the evolution equation for $\langle v_i'^2\rangle$, $\frac{\partial}{\partial t}\langle v_i\rangle^2 = 2\langle v_i\rangle\frac{\partial}{\partial t}\langle v_i\rangle$ is subtracted from Eq. (22). The subtracted term is evaluated by multiplying Eq. (17) by $2\langle v_i\rangle$. This multiplication is valid because it does not involve subsequent averaging that would require the evaluation of advective fluxes.

Performing the subtraction and rearranging the viscous terms in the usual manner gives

$$\frac{\partial}{\partial t}\langle v_i'^2\rangle = \nu\frac{\partial^2}{\partial y^2}\langle v_i'^2\rangle - 2\nu\left\langle\left(\frac{\partial v_i'}{\partial y}\right)^2\right\rangle + \langle M_{ii} + T_{ii} + S_{ii}\rangle - 2\langle M_i + T_i\rangle\langle v_i\rangle. \qquad (23)$$

Adopting the I_i notation introduced in Eq. (19) and introducing the notation $I_{ii}(y) \equiv \int_y^\infty dy\,(\langle M_{ii}\rangle + \langle T_{ii}\rangle)$, addition and subtraction of $-2I_i\frac{\partial}{\partial y}\langle v_i\rangle$ on the right-hand side of Eq. (23) gives

$$\frac{\partial}{\partial t}\langle v_i'^2\rangle = \nu\frac{\partial^2}{\partial y^2}\langle v_i'^2\rangle - 2\nu\left\langle\left(\frac{\partial v_i'}{\partial y}\right)^2\right\rangle - 2I_i\frac{\partial}{\partial y}\langle v_i\rangle - \frac{\partial}{\partial y}(I_{ii} - 2\langle v_i\rangle I_i) + \langle S_{ii}\rangle \qquad (24)$$

after some rearrangement. This is not the most useful representation for data reduction. The terms in Eq. (24) have been organized so that their counterparts in conventional Navier-Stokes budgets (as formulated by Moser *et al.* 1998) can be readily identified.

The first term on the right-hand side of Eq. (24) is the viscous diffusion term, identical in form to the corresponding term of the conventional $\langle v_i'^2\rangle$ budget. The second term is the ODT analog of the conventional dissipation term $-2\nu\left\langle\left(\frac{\partial v_i'}{\partial x_i}\right)\left(\frac{\partial v_i'}{\partial x_j}\right)\right\rangle$, which is summed over j but not over i. In ODT, property variations are represented only on the y coordinate, so the ODT dissipation term corresponds to the $j = 2$ term of this sum. This does not imply that ODT necessarily underestimates the viscous dissipation. The conservation laws obeyed by ODT assure that it will exhibit a balance between total (y-integrated) production and total dissipation plus storage (time derivative), and the model can in principle reproduce all these quantities accurately. Because the model is confined to one spatial dimension, velocity derivatives will be larger in magnitude to achieve a given dissipation level than they are in 3D flow. This illustrates that ODT may provide a reasonable representation of flow energetics although its representation of flow kinematics differs from 3D turbulence.

As noted earlier, I_i is the ODT analog of the Reynolds-stress component $\langle v_i' v_2'\rangle$. Accordingly, the third term on the right-hand side of Eq. (24) corresponds precisely to the conventional production term.

The next term is a transport term because its form precludes a net gain or loss of total $\langle v_i'^2\rangle$. It subsumes the ODT advective processes (triplet map and kernel implementation), and in this regard is analogous to the sum of conventional turbulent transport and pressure transport, here denoted 'advective transport.' There does not appear to be a physically valid decomposition of the ODT term into the two conventional transport terms. Therefore the sum of conventional terms should be compared to the ODT advective transport in computed budgets.

The quantity S_{ii} has been defined so that its properties are analogous to the conventional pressure-strain term. Though there is some arbitrariness in the definition, it was noted that an integral constraint limits its quantitative impact. $\langle S_{ii} \rangle$ measures pressure scrambling by the mechanism introduced in Sec. 2.2. The transport induced by this mechanism is subsumed in the transport term of Eq. (24). S_{ii} has been defined so that its sum over components i is zero at all y. Thus, there is no scrambling contribution to the ODT budget of q^2 (the sum of component variances), just as there is no pressure-strain term in the conventional q^2 budget.

3 Numerical Implementation

3.1 Molecular Evolution

The numerical implementation of an ODT simulation involves four subprocesses: eddy selection, eddy implementation, molecular evolution, and data gathering. The first three subprocesses are considered in their order of introduction in Sec. 2. Data gathering is not discussed further because data gathering procedures that are specific to ODT implementation are discussed in Sec. 2.5.

Molecular evolution according to Eqs. (1) and (2) is computed in a conventional manner, although the choice of the numerical scheme is influenced by the occurrence of eddy events. The eddy events affect the time-step and spatial resolution requirements. To see why, the typical time between eddy events is compared to the diffusive time scale that controls molecular evolution. In a turbulent cascade, the smallest eddies occur most frequently, so the eddy event frequency is determined primarily by the smallest eddies. Assume that the smallest eddy size $l_{\min}$ in an ODT simulation is much smaller than the computational domain size Y. (In turbulence, $l_{\min}/Y$ typically scales as $Re^{-3/4}$.) The smallest eddy in turbulence is the eddy whose contribution to transport is comparable to the kinematic viscosity ν. The corresponding eddy transport coefficient is of order $l_{\min}^2/\tau_{\min}$, where $\tau_{\min}$ is the eddy turnover time. Analysis of fluid displacements induced by triplet maps suggests the relation $\frac{2}{27} l_{\min}^2/\tau_{\min} = \nu$ (Kerstein 1991). Though this relation neglects the transport contribution of kernel implementation (Sec. 2.5), it is adequate for estimation purposes.

In the ODT context, $\tau_{\min}$ is the typical time between eddy events that include a given location. This is not the same as the typical time between eddy events in the simulation. If each size-$l_{\min}$ interval is subject to one event per time interval $\tau_{\min}$ (an idealization for estimation purposes), then then the total number of events during that time interval is $Y/l_{\min}$. Therefore the eddy event time scale for the simulation is $l_{\min}\tau_{\min}/Y$.

This time scale is compared to the CFL time scale for marginal stability of the numerical solution of the viscous evolution equation, which is $\frac{1}{2}(\Delta y)^2/\nu$, where Δy is the cell size on the

discretized 1D domain. There is generally no need for Δy to be extremely small compared to $l_{\min}$ because $l_{\min}$ by definition is the scale below which velocity fluctuations are strongly damped by viscosity. ($\Delta y \ll l_{\min}$ may be required in special cases such as flows with scalars whose diffusivity κ is much less than ν. Some cases of this sort are considered in Sec. 4. The spatial and temporal resolution requirements for these cases are modified accordingly.)

Nevertheless, Δy should be somewhat smaller than $l_{\min}$ so that the spatially discrete implementation of the triplet map and the scrambling kernel are sufficiently accurate approximations of their continuum definitions. As noted shortly, a minimum of six cells are required to implement the a discrete eddy, and more are required for a reasonable representation of the continuum formulation. For estimate purposes, the relation $\Delta y = l_{\min}/10$ is assumed for a marginally resolved computation.

Combining results, the eddy event time scale is estimated to be a factor $150\Delta y/Y$ smaller than the viscous CFL time scale. This factor is of order unity or less for any physically meaningful application of ODT. Therefore molecular evolution uninterrupted by triplet maps does not occur for time scales much longer than the viscous CFL time scale. However, acceptable accuracy is obtained in some instances if the molecular evolution time step is taken to be larger than the eddy event time scale. In this case, the eddy events scheduled to be implemented during the molecular time step are implemented instead at the end of the time step. This approach improves efficiency through the use of implicit methods for the solution of Eqs. (1) and (2). The CFL time scale for Eq. (2) is smaller than the eddy event time scale for $\kappa \ll \nu$ (due to more stringent resolution requirements) and for $\kappa \gg \nu$, so implicit methods are particularly advantageous for these cases, and were used for some of the computations discussed in Sec. 4.

This lengthening of the the molecular time step, and associated delay of the implementation of concurrent eddies, may cause an artificial cyclic variation of property gradients. The bunched implementation of eddy events can lead to excessively smooth property profiles immediately before they are implemented and excessively rough profiles immediately afterward. Time-step sensitivity studies are needed on a case-by-case basis to determine the largest time step such that flow statistics of interest are not unduly affected by this cyclic variation.

3.2 Eddy Implementation

Eddy implementation on a discretized domain requires a definition of the discrete triplet map. For conservative implementation, the discrete triplet map is defined as a permutation of the cells of the discrete domain. The eddy interval is taken to be an integer multiple of three cells. The discrete map, applied to $3k$ cells sequentially labeled 1, 2, ... , $3k$, yields the sequence 1, 4, 7, ... , $3k-8$, $3k-5$, $3k-2$, $3k-1$, $3k-4$, $3k-7$, ... , 8, 5, 2, 3, 6,

9, ... , $3k-6$, $3k-3$, $3k$. The smallest consistently defined permutation involves six cells ($k=2$), corresponding to the permuted sequence 1, 4, 5, 2, 3, 6. Note that only $3k-2$ of the cells in a nominal size-$3k$ map are permuted. Continuous and discrete representations of the triplet map are illustrated in Fig. 1.

It is straightforward to show that the mean-square displacement, $\frac{1}{l}\int_{y_0}^{y_0+l} dy\,[y-f(y)]^2$, of points in the eddy interval is $\frac{4}{27}l^2$. Based on random walk theory, this implies a diffusivity $\frac{2}{27}Nl^2$ of a fluid marker that is subject to successive size-l mappings with mean frequency N. Taking the eddy time scale τ to be an estimate of $1/N$, the relation used earlier for time-step estimation is obtained.

It is likewise straightforward to show that the mean-square displacement of cells by a size-$3k$ discrete triplet map is $\frac{4}{27}\left(1-\frac{1}{k}\right)(3k)^2$, which is a factor $1-\frac{1}{k}$ smaller than the corresponding continuum result. The effect of this deviation on advective transport, and a compensatory correction, are presented in the discussion of eddy selection, which is considered next.

3.3 Eddy Selection

As explained in Sec. 2.3, the sequence of eddy events implemented during a simulated realization is sampled from the rate distribution λ. Each event, as well as the viscous evolution, Eq. (1), between events, changes the velocity profiles v_i and therefore modifies the rate distribution. This interaction between the rate distribution and simulated flow evolution is largely responsible for key features of the model such as emulation of the inertial-range turbulent cascade (Kerstein 1999, Wunsch & Kerstein 2001). From a computational viewpoint, it causes explicit construction of, and sampling from, the rate distribution to be unaffordable owing to the need to reconstruct this distribution repeatedly.

Instead, an indirect but mathematically equivalent procedure is employed. A rate distribution that remains unchanged during the simulation is specified arbitrarily, though the procedure is most efficient if it approximates the true distribution. Events are sampled from this fixed distribution. For a given sampled event, parameterized by y_0 and l, the true value of λ at that instant is computed based on the smaller of two values: the value given by Eq. (15) and the value given by the procedure of Sec. 2.4. This true value is compared to the value specified by the fixed distribution. The comparison determines an acceptance probability for the event. This two-step procedure - random sampling followed by a random trial determining acceptance or rejection - results in an event sequence that is governed by the true rate distribution. The advantage of this approach is that each invocation procedure requires determination of the true value of λ for only one eddy, rather than for all possible (y_0,l) pairs.

This procedure is implemented as follows. A fixed rate distribution $\Lambda(y_0,l)$ is preassigned,

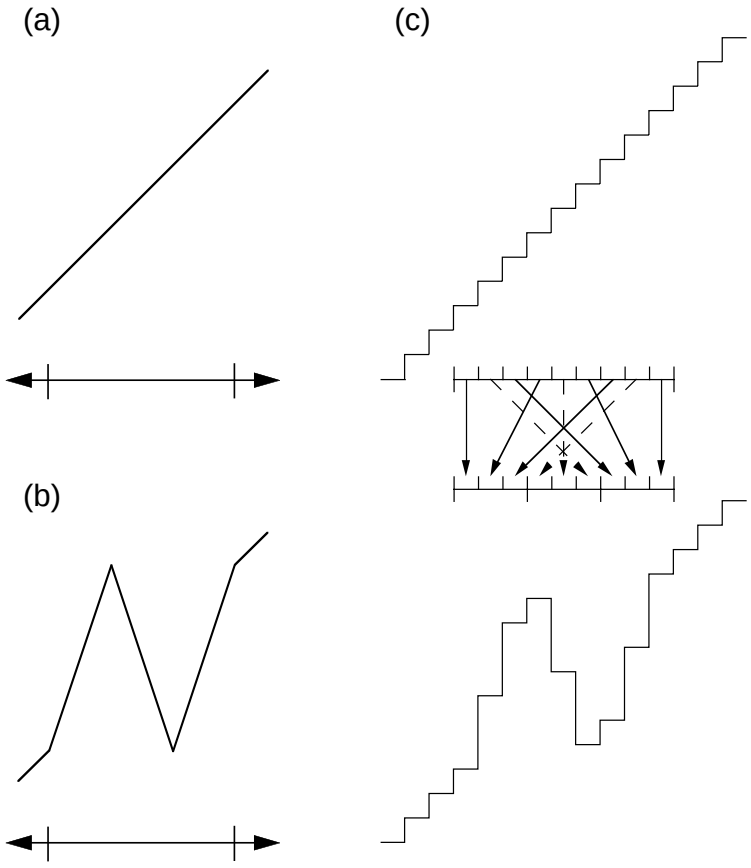

Figure 1. Effect of the triplet map on an initially linear fluid-property profile. (a) Initial profile. (b) Velocity profile after applying the triplet map to the interval denoted by ticks. (c) Discrete representation of the initial profile, and illustration of the effect of a triplet map on an interval consisting of nine cells. For clarity, arrows indicating formation of the central of the three images of the original interval are dashed.

such that Λ is nonzero for any (y_0, l) pair allowed in the simulation. One eddy sampling occurs per time step Δt, where Δt is chosen to obtain an adequate approximation of eddy sampling in continuous time.

One condition that Δt must satisfy is that the expected number N of eddies during the time interval $[t, t+\Delta t]$, which equals $\int dy_0\, dl \int_t^{t+\Delta t} dt\, \lambda(y_0, l; t)$, must be much less than unity. This is required because at most one eddy is implemented per Δt interval. This sampling can adequately approximate the true eddy sequence only if the true sequence rarely involves two or more eddies during a Δt interval. This requires $N \ll 1$ because the probability of two or more events during this interval is of order N^2 (assuming independent events for estimation purposes). For example, if $N^2 = 0.01$ provides sufficient accuracy, then this requires a sampling rate at least ten times higher than the true eddy rate. Physically based estimates (Sec. 3.1) indicate that the true eddy rate determines the shortest time scale in the model, so Δt is by far the smallest time step in the simulation. If the sampling rate is at least 10 times higher than the true eddy rate (a nominal factor, because the numbers are illustrative), then the fraction of sampled eddies that are implemented must be less than 0.1 in order for the eddy implementation rate in the numerical simulation to equal the true rate defined by the model.

These estimates are based on the rate of occurrence of all eddies. In the foregoing expression for N, this corresponds to integration over all values of y_0 and l. Likewise, one may compare the true event rate and the numerical implementation rate for events corresponding to any differential increment $dy_0\, dl$ of these parameters. The true rate is $\lambda(y_0, l; t)\, dy_0\, dl$ and the numerical implementation rate is the sampling rate $\Lambda(y_0, l)\, dy_0\, dl$ times the probability P that the sampled event is implemented. Thus, to match the true rate, implementation of a sampled event is determined by a Bernoulli trial with acceptance probability

$$P = \lambda(y_0, l; t)/\Lambda(y_0, l). \tag{25}$$

Operationally, this procedure is implemented as follows. At each time step Δt, eddy parameters y_0 and l are sampled from the preassigned joint probability density function (PDF) of y_0 and l, $\Lambda(y_0, l)\, \Delta t$. Based on the current state of the system, $\lambda(y_0, l; t)$ is computed and P is evaluated based on Eq. (25). The specified eddy is then implemented with probability P. If it is not implemented, then no further trials are performed during the current time step. It is convenient to preassign the sampling PDF $\Lambda(y_0, l)\, \Delta t$ rather than $\Lambda(y_0, l)$ because the sampling is then independent of Δt, which can vary during the simulation. Then P is evaluated by multiplying the numerator and denominator in Eq. (25) by Δt. The denominator is then preassigned and the numerator depends explicitly on Δt.

Expressed in this form, Eq. (25) indicates that P is proportional to Δt. Therefore a requirement for accurate emulation of the true rate for eddies in any $dy_0\, dl$ range is that Δt must be small enough so that the P values for eddies within that range rarely exceed unity.

This requirement indicates the advantage of choosing a sampling PDF $\Lambda(y_0, l)\,\Delta t$ that is close to the true PDF, which is approximately $\lambda(y_0, l; t)\,\Delta t/N$. If these PDFs differ greatly, then a Δt value that is small enough to assure that $P < 1$ for all eddies may result in $P << 1$ for eddies in particular ranges of y_0 and l. This implies oversampling of some eddies. If the oversampled eddies are eddies that are relatively rare, then the overall sampling rate may not be raised significantly. However, inefficiency can result if the oversampled eddies are those with the highest true rates. To avoid the latter outcome, it is advantageous to choose a sampling PDF that weights the rare eddies (typically the large eddies) somewhat more heavily than simple scaling estimates would prescribe. This will assure that it is the rarer eddies that are oversampled, even when fluctuations cause temporary deviations from the expected scalings.

For transient flows, it can be advantageous to adjust Δt and the sampling PDF dynamically. Several procedures have been applied successfully. One way to adjust Δt is to compute a moving average of P values and periodically reset Δt to keep this moving average close to a target value. Fluctuations can cause P to vary by an order of magnitude or more, even with an accurate (in an average sense) sampling PDF, so a target value of order 0.1 is prudent. Owing to the flow dependence of statistical properties of the simulation, no universally valid criterion can be established. The most reliable procedure is to perform runs with successively smaller target probabilities until convergence of flow statistics is obtained. Likewise, determination of the required spatial resolution by successive grid refinements until statistics converge is recommended.

Dynamical adjustment of the sampling PDF has proven effective, and even essential for affordable computations, in some instances. This is an elaborate, flow dependent procedure.

As outlined thus far, the eddy selection procedure accounts for the time discretization of the sampling process but not the spatial discretization of y_0 and l. The discretization of l is of particular concern because numerical implementation requires l to be an exact multiple of three times the cell size (Sec. 3.2). The discretization of l is thus a factor of three coarser than the discretization of y_0.

There is not a unique procedure to compensate for this discretization because eddies have multiple effects (transport, length scale reduction, energy transfer, etc.), each of which might require a different correction. A transport correction has been developed and implemented that has provided significant reduction of the spatial resolution requirements for numerical convergence of several simulated flows. The correction addresses only the triplet-map contribution to transport, omitting any transport correction due to discrete implementation of the kernel. (As shown in Sec. 2.5, kernel implementation induces transport as well as scrambling.)

In Sec. 3.2, it is noted that a discretized triplet map applied to an interval consisting of $3k$ cells induces a mean-square cell displacement that is a factor $1 - \frac{1}{k}$ smaller than a

continuum triplet map of that size. If the interval size $3k$ is different from the sampled l value due to roundoff of $\frac{l}{3}$ to the nearest integer value k, then the mean-square displacement of the discretized map is a factor $(3k/l)^2$ times the continuum displacement. Combining these factors, the ratio of the mean-square displacements of the discrete and corresponding continuum maps is $(k-1)(3k/l)^2$.

The diffusivity corresponding to mapping-induced transport of fluid cells in the simulation is proportional to the mean-square cell displacement times the frequency of mappings that contain a given fluid element. This frequency is proportional to the eddy event rate times a correction factor reflecting the dependence of the amount of affected fluid on the eddy size. Thus, for a given event rate, the frequency of discrete eddies that contain a given fluid element differs by a factor $3k/l$ from the corresponding continuum frequency. Combining this and the displacement correction, it is concluded that the discrete-eddy diffusivity for a given event rate differs from the corresponding continuum-eddy diffusivity by a factor $(k-1)(3k/l)^3$.

To compensate for this spatial discretization effect, the right-hand side of Eq. (25) is divided by this factor. This modifies the rate of implemented events so that the simulation better approximates the advective transport prescribed by the model.

Various approaches to convergence enhancement have been used in the computations discussed in this report. The specific correction factor derived above has not yet been used, but it is recommended for future use be cause it accounts for more effects than approaches used to date.

Spatial discretization requires care in the determination of the eddy location as well as the eddy event rate. It has been noted that eddy size l is discretized to an integer multiple of three cells, a coarser discretization than for the eddy location y_0. Therefore only one of the two ends of the eddy interval can be specified to within one cell width, because the other is determined by the eddy size. This asymmetry implies that eddy intervals in wall-bounded flow should be selected by first choosing the location of the endpoint closer to the wall and then determining the other endpoint based on the eddy size. This maximizes the precision of the numerical algorithm in the near-wall region, where property gradients are steepest. Numerical tests indicate that this approach is advantageous, although other methods are adequate if the spatial resolution is sufficient.

4 Near-Wall Model Demonstrations

4.1 Free Shear Flow

In this section, applications of ODT to various canonical flows are presented in order to demonstrate the performance of the model, including several variants not discussed in Sec. 2. Applications of earlier formulations of ODT to homogeneous turbulence have been discussed in detail previously (Kerstein 1999, Wunsch & Kerstein 2001). Although the formulation presented in Sec. 2 has some new features with significant implications for homogeneous shear flow, this flow is not examined here because the method of Sec. 2.4 for suppressing the large-eddy anomaly is ineffective for this flow. A more effective method has been formulated but has not yet been implemented because it greatly complicates the model but broadens its applicability only slightly.

The model formulation of Sec. 2 is first applied to two time-developing free shear flows, a planar mixing layer and a wake. Results are compared to DNS of these flows by Rogers & Moser (1994) and Moser *et al.* (1998), respectively. Many features of turbulent free shear flows are insensitive to viscous transport, so they provide direct tests of the model representation of advective processes.

For each flow, the ODT results are based on 5000 simulated realizations. To facilitate initial transient relaxation, it is convenient to choose the initial velocity profiles to be continuous functions of y. Accordingly, the initial v_1 profile for the mixing layer is a linear ramp between two semi-infinite flat regions whose velocity difference is denoted ΔU. The initial v_1 profile for the wake is a symmetric tent. The initial v_2 and v_3 profiles for both flows are nominally zero, but are seeded with small random perturbations as explained in Sec. 2.2. For both flows, the computational domain is taken to be large enough so that it is effectively infinite, i.e., the turbulent region does not extend close enough to the boundaries during the simulations to be affected by their presence.

Owing to the coordinate invariance of the pressure-scrambling mechanism (Sec. 2.2), the statistical evolution of velocity components subject to the same initial and boundary conditions (in this instance, the v_2 and v_3 components) is indistinguishable in the present formulation of ODT. A more general formulation that breaks this symmetry while maintaining required invariance properties has been formulated and tested. This formulation involves three eddy types, each of which allows energy exchange between two of the three velocity components. Because eddy selection is based on the v_2-component available kinetic energy (Sec. 2.3), this generalization breaks the (v_2, v_3) symmetry. In particular, it captures the 2D (v_1, v_2) character of the dominant shear instabilities. However, this formulation is not adopted here because its performance is not commensurate with the additional complexity and parameter tuning that it entails. The formulation presented in Sec. 2 captures the prin-

cipal manifestation of anisotropy, resulting from the imposition of the initial shear solely on the v_1 component, but not the secondary manifestations that break (v_2, v_3) symmetry.

The high-Re regime of self-similar flow evolution is examined. For the wake, ODT results are presented for Reynolds number, defined as $Re = \frac{1}{\nu}\int_{-\infty}^{\infty}\langle v_1\rangle\, dy$, equal to 2000, the same value as in the DNS comparison case. In the time-developing wake, Re remains constant during the simulations. For the mixing layer, the initial value of Re based on ΔU and the momentum thickness $\delta_m = \int_{-\infty}^{\infty}\left[\frac{1}{4} - (\langle v_1\rangle/\Delta U)^2\right] dy$ is 427, compared to an initial DNS value of 800. (The definition of δ_m is based on nominal v_1 values of $\pm\Delta U/2$ in the flat regions.)

The flow statistics considered here are large-scale dominated, and accordingly, are insensitive to viscous transport for the Re values considered. (This insensitivity has been verified by performing parameter excursions.) Accordingly, the results are insensitive not only to the kinematic viscosity ν, but also to the model parameter Z that controls the strength of the viscous penalty in the eddy rate distribution, Eq. (15). The results presented here correspond to $Z = 0.02$.

The model parameter C is an overall rescaling of the eddy rate distribution. In flow regimes that are insensitive to the strength of viscous processes, this distribution controls the evolution of flow structure in ODT simulations. Therefore modification of C is equivalent to rescaling of the time coordinate, and hence rescaling of the growth rate, in these regimes. For the self-similar regimes of both flows considered here, it has been verified that variation of C changes only the growth rate, with no effect on other properties other than proportionate rescaling of quantities dependent on the growth rate.

These self-similar regimes exhibit the same growth laws as the corresponding DNS results. The numerical coefficients in the DNS growth laws, $\frac{1}{\Delta U}\frac{d\delta_m}{dt} = 0.014$ for the mixing layer and $\frac{1}{U_0}\frac{db}{dt} = 0.12$ for the wake (where b is the full width at half-maximum of the mean velocity profile, growing as $t^{1/2}$, and U_0 is the centerline mean velocity, decaying as $t^{-1/2}$), are matched for $C = 3.78$ and 5.55 for the mixing layer and wake, respectively. These C values were used for all α values considered because the growth rates were found to be insensitive to α.

For each of the flow statistics considered, the onset of self-similarity was demonstrated by verifying the collapse of normalized quantities computed within time bands. Once the self-similar time regime was identified, all the normalized data within the self-similar regime was pooled.

Lateral profiles of mean velocity, Reynolds shear stress, velocity fluctuations, and velocity fluctuation budgets obtained from the self-similar regime of the ODT simulations are compared to DNS results in Figs. 2-6. All quantities are normalized as in the DNS studies. Lengths are scaled by δ_m and b, and velocities are scaled by ΔU and U_0, for the mixing layer and wake, respectively.

As explained in Sec. 2.1, advection on the 1D domain is implemented in ODT as a se-

quence of instantaneous events rather than as continuous motion governed by the velocity profiles. Therefore the flux interpretation of quantities such as the Reynolds stress component $\langle v_1' v_2' \rangle$ is not applicable if these quantities are computed in ODT directly from the velocity components. In Navier-Stokes flow, $\langle v_1' v_2' \rangle$ can be interpreted as the advection of v_1 fluctuations by v_2 fluctuations, but in ODT, the v_2 velocity does not directly prescribe the advection of v_1 (or of any other fluid property). Therefore the Reynolds stresses and other advective fluxes (arising, e.g., in velocity fluctuation budgets) are evaluated in ODT by monitoring eddy-induced fluxes during simulated realizations. This assures that conservation laws and balance equations are satisfied exactly. The formal development of this approach is presented in Sec. 2.5.

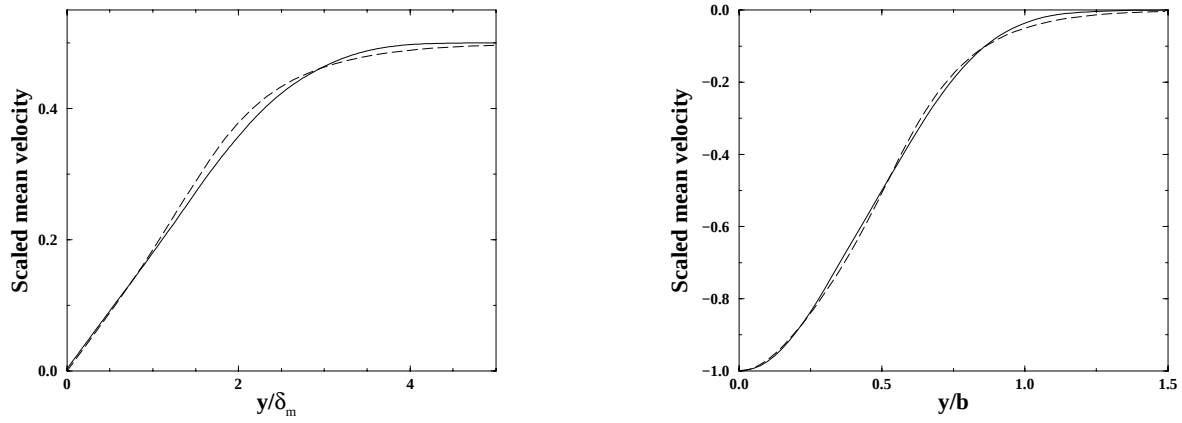

Figure 2. Lateral profile of mean streamwise velocity, scaled by ΔU for the mixing layer (left frame) and by U_0 for the wake (right frame): – – –, ODT; ——, DNS.

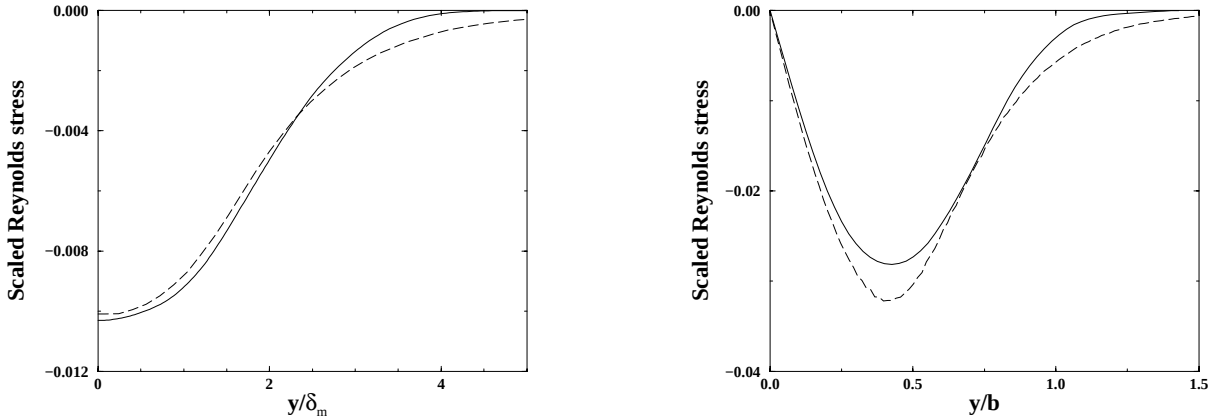

Figure 3. Lateral profile of Reynolds shear stress $\langle v_1' v_2' \rangle$, scaled by $(\Delta U)^2$ for the mixing layer (left frame) and by U_0^2 for the wake (right frame): – – –, ODT; ——, DNS.

Figures 2 and 3 indicate reasonable agreement with the DNS mean axial velocity and Reynolds shear stress profiles of both flows. The shapes of these profiles are largely dictated by the mean spreading rate. ODT spreading rates have been matched to the DNS spreading rates for these flows by parameter adjustment, so these comparisons are not stringent tests of model performance.

Lateral profiles of ODT velocity-component variances $\langle v_1'^2 \rangle$, $\langle v_2'^2 \rangle$, and $\langle v_3'^2 \rangle$, and their sum q^2, are compared to DNS results in Fig. 4. The ODT results for the the v_2 and v_3 velocity components are identical because the model formulation of Sec. 2 does not distinguish between the v_2 and v_3 velocity components in the flows considered here. The DNS results indicate that the differences between the statistics of these components are smaller than the differences between either of them and the v_1-component statistics. This is consistent with the physical origins of the anisotropy, discussed earlier.

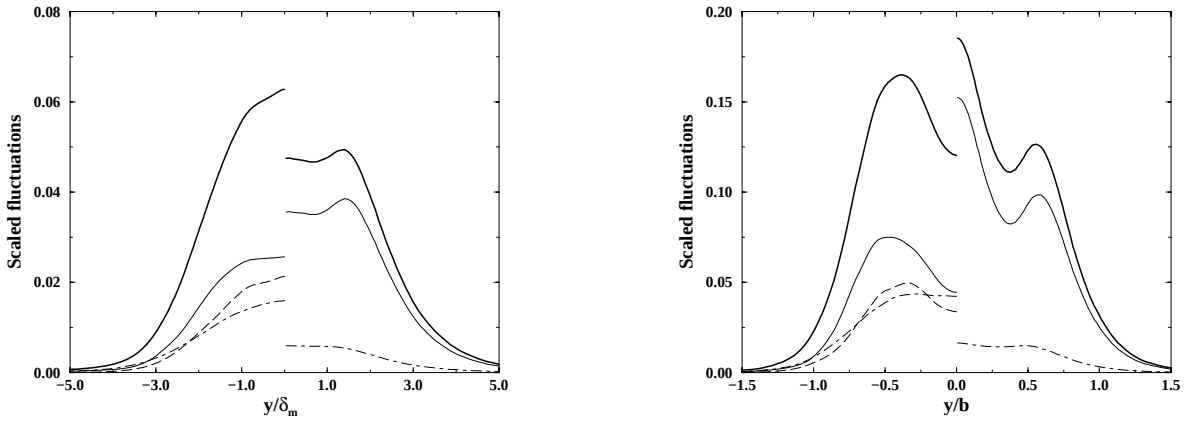

Figure 4. Lateral profiles: ——, q^2; ——, $\langle v_1'^2 \rangle$; —·—, $\langle v_2'^2 \rangle$; – – –, $\langle v_3'^2 \rangle$, scaled by $(\Delta U)^2$ for the mixing layer (left frame) and by U_0^2 for the wake (right frame). ODT and DNS results are plotted right and left of centerline, respectively. (The ODT $\langle v_3'^2 \rangle$ profiles are identical to the ODT $\langle v_2'^2 \rangle$ profiles.)

It is seen that $\langle v_1'^2 \rangle$ is consistently overpredicted and the other component variances are underpredicted. The comparison of ODT and DNS budgets of $\langle v_1'^2 \rangle$ in Fig. 5 indicates the likely origin of these trends. The transfer of turbulent kinetic energy from the v_1 component to the other components by the pressure-scrambling mechanism is lower in ODT than in DNS. This transfer is controlled by the parameter α introduced in Sec. 2.2. The value 2/3 was selected based on a physical interpretation of the ODT scrambling mechanism. If instead, the largest allowed value $\alpha = 1$ is chosen in order to maximize the transfer, the ODT component variances are found to be significantly closer to their DNS counterparts, although the aforementioned trend is not entirely eliminated. Other properties such as the q^2 profile and the budget of q^2 (Fig. 6) are not much affected by the change. Moreover, $\alpha = 1$

does not give better results for channel flow (Sec. 4.2), so for present purposes, $\alpha = 2/3$ is adopted as the baseline value.

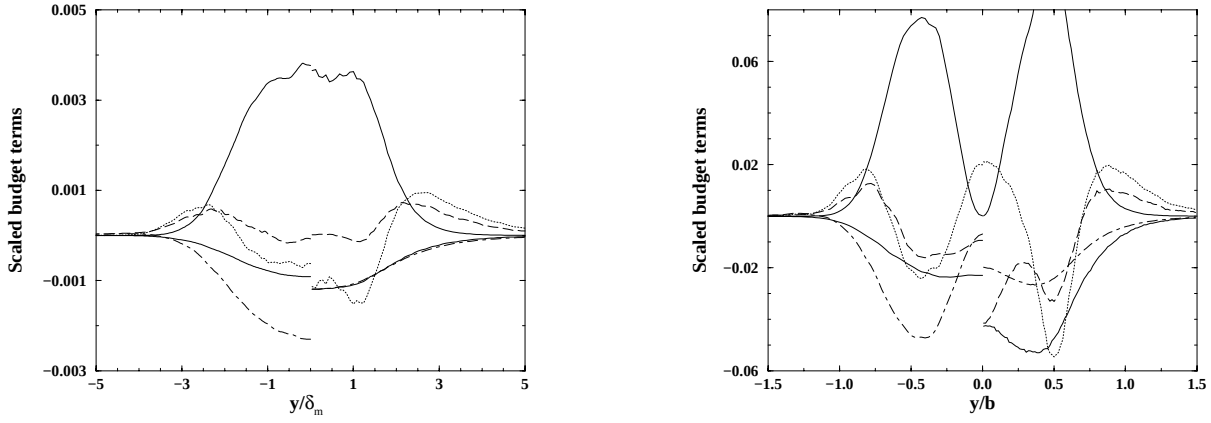

Figure 5. Budget of $\langle v_1'^2 \rangle$, scaled by $\Delta U^3/\delta_m$ for the mixing layer (left frame) and by U_0^3/b for the wake (right frame): ——, production (upper), dissipation (lower); – – –, time derivative; · · ·, advective transport; — · —, scrambling. ODT and DNS results are plotted right and left of centerline, respectively.

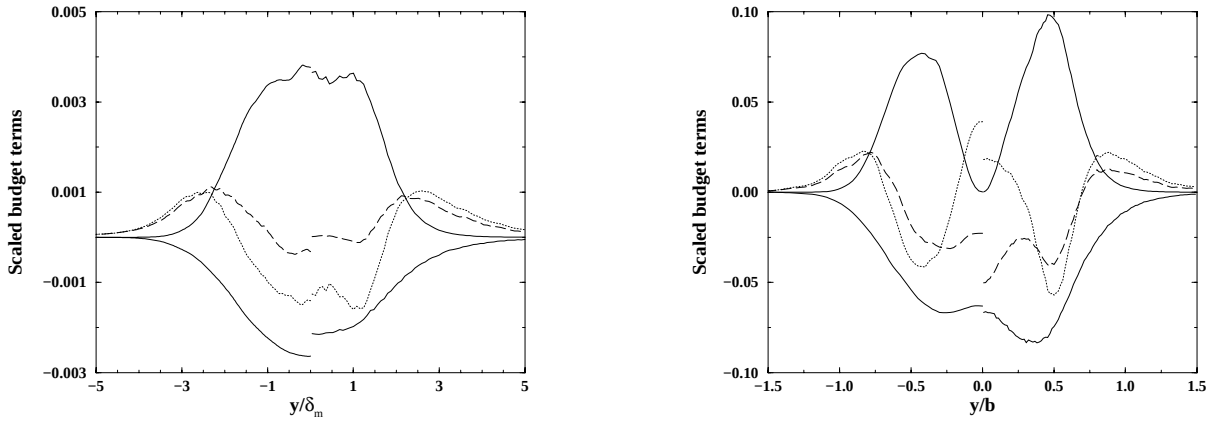

Figure 6. Budget of q^2. Format as in figure 5.

It is apparent that ODT provides a reasonable overall representation of free shear flow structure and energetics (e.g., q^2 profile and budget), although details of the kinematics (e.g., evolution and coupling of the velocity components) are not consistently reproduced. Comparable performance is seen in the channel-flow results considered next.

4.2 Channel Flow

Channel flow is the validation case for the coupled ODT/LES formulation, so it is considered in detail in Sec. 6.1. For comparison purposes, ODT simulations of this flow are presented.

Time-developing turbulent flow in a planar channel of width h is simulated by applying the boundary conditions $v_i = 0$ to all velocity components on a size-h domain, and introducing a fixed source term $-\frac{1}{\rho}\frac{\partial P}{dx}$ on the right hand side of Eq. (1) for $i = 1$. This term introduces an imposed mean pressure gradient in the streamwise (x) direction, but does not include pressure fluctuations. (Pressure fluctuations are not modeled explicitly, but their effects are represented in the implementation of eddy events.)

ODT results for statistically steady flow are compared to corresponding DNS results of Moser *et al.* (1999). DNS results are reported for $Re_\tau = 180$, 395, and 590. Here, $Re_\tau = u_\tau h/(2\nu)$, where $u_\tau = \sqrt{\nu dv_1/dy|_{y=0}}$ is the friction velocity.

ODT channel simulations have been performed for various values of the parameters C and Z and for two values of α, the base case $\alpha = 2/3$ and the alternate case $\alpha = 1$. As noted in Sec. 4.1, the α variation had little effect on the overall performance of the model. Results for $\alpha = 2/3$ are shown here. The parameters C and Z were adjusted to obtain the best overall match to the DNS friction law and mean velocity profile. The friction law is sensitive mainly to C, which controls the turbulence intensity. By controlling the frequency of small eddies, Z mainly affects the transition of the mean velocity profile from near-wall viscous structure to a profile shape farther from the wall that reflects turbulence effects. The results shown here correspond to $C = 12.73$ and $Z = 98$, chosen to match the DNS mean velocity profile and the DNS value of the friction coefficient $C_f = 2(u_\tau/\bar{U})^2$ at $Re_\tau = 590$. (Here, $\bar{U}$ is the mean bulk velocity.) It is noted in Sec. 6.1 that a slightly lower C value is preferable in ODT/LES simulations.

Figure 7 shows good agreement with the DNS C_f value at $Re_\tau = 395$ and slight overprediction of C_f at $Re_\tau = 180$. ODT is formulated based on scalings applicable to high-intensity turbulence, so it may provide a less accurate representation of the weak turbulence at this Re_τ value. For the other flow properties considered here, neither DNS nor ODT exhibit much sensitivity to Re_τ, so results are shown only for $Re_\tau = 590$.

Lateral profiles of flow properties are plotted in the wall coordinate $y^+ = yu_\tau/\nu$. In Fig. 8, the scaled mean velocity $\langle v_1\rangle/u_\tau$ is denoted u^+. Good agreement with the DNS profile is obtained.

The diagonal components, and the nonvanishing off-diagonal component, of the scaled Reynolds-stress tensor are shown in Fig. 9. The diagonal components are underpredicted by ODT. In Sec. 6.1, it is shown that ODT/LES results for the diagonal components are in better agreement with DNS results, perhaps due to more realistic forcing of the near-wall region by the bulk flow.

Despite the discrepancies seen in Fig. 9, the ODT predictions of the terms of the v_1

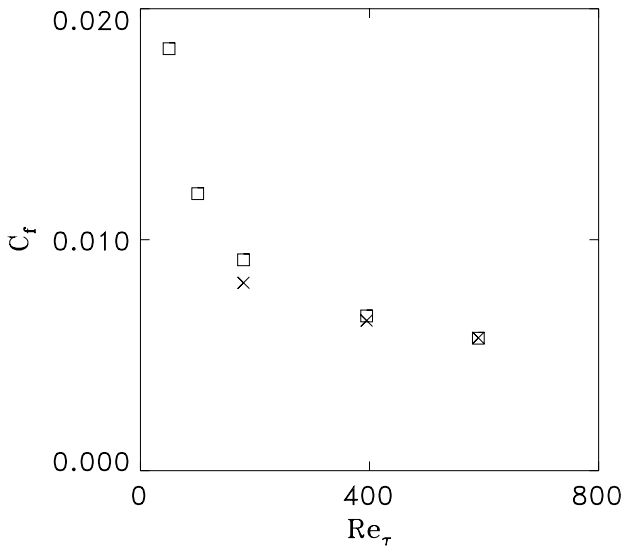

Figure 7. Computed friction coefficient for channel flow. □, ODT; ×, DNS.

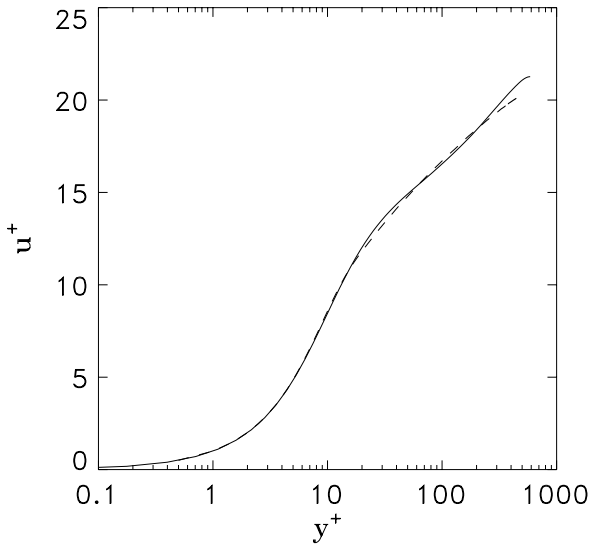

Figure 8. Semilog plot of the mean velocity profile for channel flow at $Re_\tau = 590$, in wall coordinates. – – –, ODT; ——, DNS.

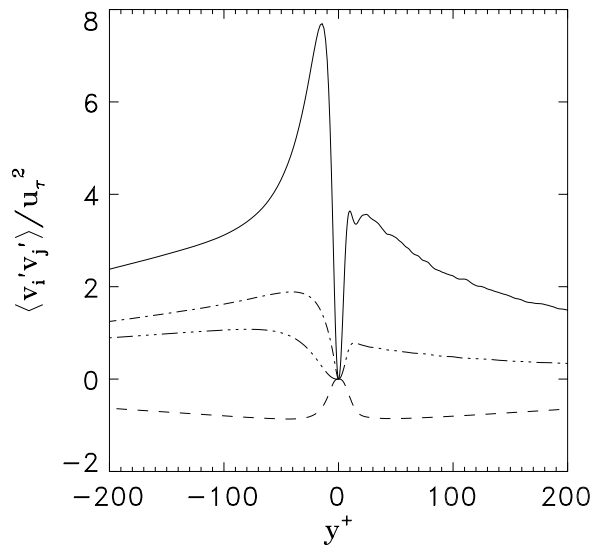

Figure 9. Lateral profiles of Reynolds stress components in channel flow, scaled by u_τ^2: ——, $\langle v_1'^2 \rangle$; — · · · —, $\langle v_2'^2 \rangle$; — · —, $\langle v_3'^2 \rangle$; – – –, $\langle v_1' v_2' \rangle$. (The ODT $\langle v_3'^2 \rangle$ profile is identical to the ODT $\langle v_2'^2 \rangle$ profile.) ODT and DNS results are plotted right and left of centerline, respectively.

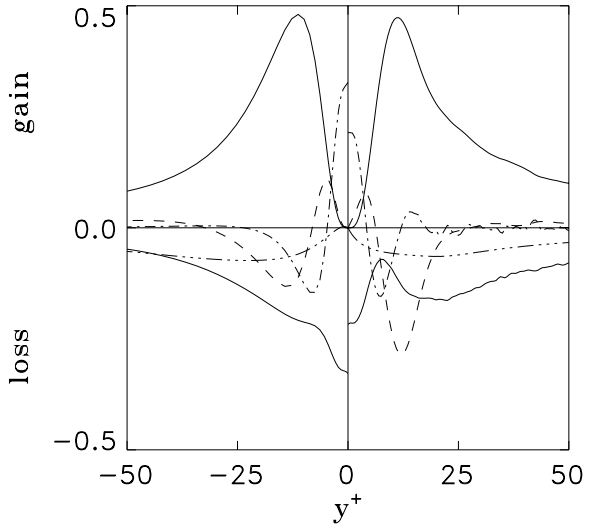

Figure 10. Budget of $\langle v_1'^2 \rangle$ in channel flow, in wall coordinates: ——, production (upper), dissipation (lower); – – –, advective transport; — · —, viscous transport; — · · · —, scrambling. ODT and DNS results are plotted right and left of centerline, respectively.

variance budget (Fig. 10) are in good overall agreement with the corresponding DNS terms. This indicates that ODT is a fundamentally sound model of near-wall flow energetics.

4.3 Rayleigh-Bénard Convection

Here and in Sec. 4.4, the model formulation of Sec. 2 is generalized to incorporate buoyant stratified flow. These applications predate the vector velocity formulation of ODT, so they involve a single velocity component v. The vector velocity formulation reduces to a one-component formulation by setting the scrambling parameter α equal to zero. This reduction is physically reasonable if only one velocity component is subject to external forcing and if flow anisotropy does not play an essential role in the phenomena of interest. Operationally, the reduced formulation is obtained by substituting v for v_2 and taking $\alpha = 0$ in the formulation of Sec. 2.

Buoyancy effects are introduced in the Boussinesq approximation. Namely, a constant reference density ρ_0 is assumed in all terms except those involving the gravitational acceleration g. The density appearing in those terms evolves like any other scalar in the simulation, subject to the appropriate initial and boundary conditions.

Two new terms appear in the most general Boussinesq formulation of ODT. They are identified by decomposing the gravity vector into components parallel and orthogonal to the ODT computational domain. To simplify the discussion, the two special cases of parallel and orthogonal gravity are considered separately.

In the first case, the ODT domain is vertically oriented. Triplet maps rearrange the vertical profile of density, thereby changing the gravitational potential energy. To conserve total energy, an equal-and-opposite change of the flow kinetic energy is implemented during each eddy event. This is accomplished by kernel implementation with amplitude c chosen to obtain the desired energy change. A sign ambiguity in the determination of c is resolved in the same manner as in Sec. 2.2.

This procedure can add any amount of energy to the flow, but it cannot extract more than the available kinetic energy defined in Sec. 2.2. Therefore an increase in the gravitational potential energy by more than this amount is energetically prohibited.

Accordingly, a gravitational term is added to the right-hand side of Eq. (14) that has the following properties: it is proportional to the mapping-induced gravitational potential energy change, and it causes the right hand side to be negative (for $\alpha = Z = 0$) if and only if the event is energetically prohibited. These requirements uniquely determine the additional term, which is $-\frac{8}{27}\frac{\rho_K}{\rho_0}gl$, where ρ_K is defined by substituting ρ for v_i in Eq. (6).

If, however, the ODT domain is horizontally oriented, then rearrangement of the density profile does not change the gravitational potential energy. Now, buoyancy effects are introduced (again within the Boussinesq approximation) by interpreting v as the vertical velocity

component (or, in the vector formulation, designating either v_1 or v_3 as the vertical component) and adding a forcing term $g(\rho_0 - \rho)$ to the right hand side of the evolution equation, Eq. (1), for that component.

In this section, a vertically oriented domain is used to simulate Rayleigh-Bénard convection. In Sec. 4.4, a horizontally oriented domain is applied to a different buoyancy-driven flow.

In Rayleigh-Bénard convection there is no mean flow, so v serves solely as a reservoir of turbulent kinetic energy. For flows involving horizontal mean motion as well as buoyant stratification, v is taken to be the streamwise velocity component, here assuming a vertically oriented ODT domain. Results of simulations for this class of flows, as well as for Rayleigh-Bénard convection, were reported previously (Kerstein 1999), but the formulation used in that study lacked the conservative representation of energy-conversion processes that is used here.

Rayleigh-Bénard convection is simulated in ODT by applying constant-density boundary conditions at the top and bottom of an ODT domain whose size is denoted h, where the upper boundary is held at density $\Delta\rho$ larger than the lower boundary. The velocity boundary condition at both boundaries is $v = 0$. Molecular evolution is governed by Eq. (2) with ρ substituted for θ. The initial condition is arbitrary because the simulation is run to a state of statistically steady evolution before data is gathered.

The large-eddy suppression mechanism introduced in Sec. 2.4 is omitted from the Rayleigh-Bénard simulations. Although this mechanism can in principle be extended to dynamically active scalars such as density in buoyancy-driven flow, it may not accurately reflect the physics of buoyancy-driven flows. Large-scale motion driven by wall-layer density gradients is an important feature of this class of flows, so the scale-locality property of the large-eddy suppression mechanism may be inapplicable. Computed results supporting this viewpoint are presented shortly. The large-eddy suppression mechanism is likewise omitted from the buoyant-flow formulation used for the computations discussed in Sec. 4.4.

Large-eddy suppression is omitted from the subgrid implementation of ODT because ODT in this case represents a restricted subdomain of the flow. This subdomain is not typically large enough to include eddies that could cause a significant transport anomaly.

The governing parameters of the Rayleigh-Bénard simulation are the same as for the physical configuration. The strength of the buoyant forcing relative to dissipative mechanisms, which controls the turbulence intensity, is measured by the Rayleigh number, $Ra = g\Delta\rho h^3/(\rho_0\nu\kappa)$. The combination of molecular transport coefficients in the denominator is somewhat arbitrary in the present context, though it has a theoretical basis in other contexts. Reflecting this arbitrariness, the second governing parameter is the Prandtl number, $Pr = \nu/\kappa$. Ra times any power p of Pr yields a new dimensionless group with denominator $\nu^{1-p}\kappa^{1+p}$.

Pr is a fundamental parameter because it is the ratio of the two relevant fluid properties. Thus, Pr is varied by the choice of fluid and Ra is varied, for a given fluid, by changing the flow configuration (boundary conditions, domain size, and gravitational acceleration). Therefore measured quantities are typically plotted versus Ra, with one curve for each Pr value considered.

The normalized mean heat flux, $Nu = Q/Q_0$, is shown in Fig. 11. Here, Q_0 is the steady state heat flux in the absence of fluid motion, in which case Eq. (2) and the boundary conditions imply $Q_0 = \kappa\Delta\rho/h$. Density is used here as a surrogate for enthalpy, which is valid for computing normalized quantities in the Boussinesq approximation. Accordingly, $Q = \kappa\langle(d\rho/dy)|_w\rangle$, where the subscript denotes the wall value of the density derivative.

Measured curves for three Pr values are shown. Nu is multiplied by $Ra^{-1/3}$ to remove the trend representing the classical scaling $Nu \sim Ra^{1/3}$, which is dimensionally prescribed if it is assumed that wall-layer structure is independent of domain size h. Deviations from a horizontal line in the figure therefore reflect the influence of the far wall on the boundary layer. The measurements indicate the presence of this influence. The measured deviations from classical scaling exhibit Pr dependencies that have not yet been explained satisfactorily from first principles.

The ODT results are based on parameter values $C = 26.1$ and $Z = 1.21$ that were chosen to match the measurements. Though the close correspondence between computed results and measurements is partly attributable to this parameter adjustment, the comparison clearly indicates that the model captures flow properties that cause deviation from classical scaling. Interaction across the flow domain is presumably due to large scale motions such as plumes emanating from the boundaries. It is remarkable that ODT, in which advective motions are instantaneous, can capture effects that appear to reflect a significant degree of space-time coherence. This suggests that the imprint of mapping events on the evolving v and ρ fields and the consequent influence on future events provides a physically realistic degree of coherence. One might expect this coherence to be somewhat less than in physical flows due to the stochastic nature of the model. An indication that this may the case is the apparent reduction of the slopes of the computed curves with increasing Ra, suggesting suppression of the interaction mechanism at high turbulence intensity.

Further indication that the model provides a fundamentally sound representation of Rayleigh-Bénard convection is provided in Fig. 12. The plot shows computed midpoint density fluctuations for the cases plotted in Fig. 11 and corresponding measurements for the only Pr at which this measurement has been made. The agreement clearly indicates that the model has predictive capability because it is obtained with no additional parameter adjustment.

The ODT representation of Rayleigh-Bénard convection is different from the other flows considered in this section in that the eddies in this flow are driven predominantly by gravita-

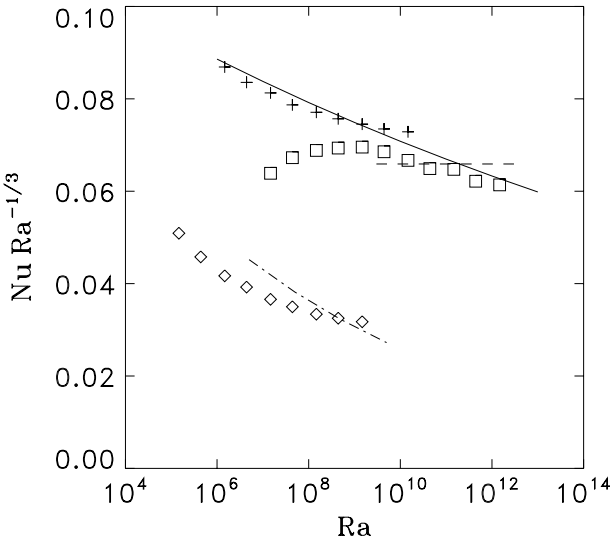

Figure 11. Rayleigh-number (Ra) dependence of the normalized mean heat flux Nu in Rayleigh-Bénard convection, compensated so that the classical scaling $Nu \sim Ra^{1/3}$ corresponds to a horizontal line on the plot. ODT computations: $\diamond$, $Pr = 0.025$; $+$, $Pr = 0.7$; $\square$, $Pr = 2750$. Measurements: —·—, $Pr = 0.025$ (Cioni *et al.* 1997); ——, $Pr = 0.7$ (Niemela *et al.* 2000); – – –, $Pr = 2750$ (Goldstein *et al.* 1990).

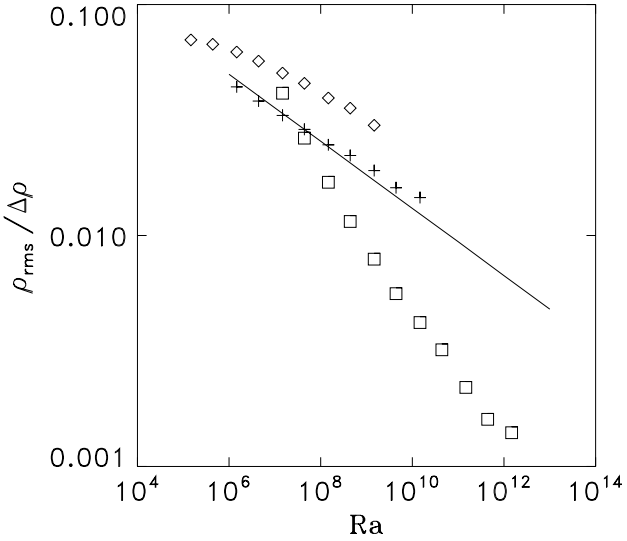

Figure 12. Normalized midpoint density fluctuations in Rayleigh-Bénard convection. ODT computations: $\diamond$, $Pr = 0.025$; $+$, $Pr = 0.7$; $\square$, $Pr = 2750$. Measurements: ——, $Pr = 0.7$ (Niemela *et al.* 2000).

tional forcing rather than shear. (In the ODT representation of the buoyancy-driven vertical channel, gravitational forcing generates shear which then drives the eddies; see Sec. 4.4.) Possibly reflecting this distinction, the empirically determined value of C for Rayleigh-Bénard convection is about five times larger than the typical value for the other flows. (Values for the other flows range from 3 to 7.) The present formulation of ODT will not provide quantitative accuracy for the full range of multiphysics environments due to the flow dependence of the parameter fit. Extensive testing will be needed to determine whether the performance of ODT as an LES subgrid model is subject to analogous limitations.

4.4 Buoyancy-Driven Vertical Channel

In Rayleigh-Bénard convection, the heat flux is parallel to the gravitational forcing. Buoyancy-driven flows in which the heat flux and the gravitational forcing are not aligned are particularly difficult to model using conventional methods (Petukhov & Polyakov 1988). Here, a flow of this type is considered.

The configuration that is selected for study is flow between parallel vertical plates with fixed density boundary conditions imposed at the plates, maintaining a density difference $\Delta\rho$ across the plates, whose separation is denoted h. This is the Rayleigh-Bénard configuration with $\pi/2$ rotation of the gravity vector. Ra and Pr as defined in Sec. 4.3 are again the governing parameters.

As explained in Sec. 4.3, this flow is modeled using an ODT formulation with a single velocity component that is interpreted as the vertical component. The evolution (apart from eddy events) of this component is governed by Eq. (1) with a forcing term $g(\rho_0 - \rho)$ added to the right hand side. Adopting the conventional notation for this flow, this velocity component is denoted w.

The ODT coordinate y is now horizontal, so eddy events do not change the gravitational potential energy. Indeed, there is no longer a gravitational potential energy concept within the formulation. The forcing term introduces a kinematic emulation of buoyancy effects without accounting for the implied energy exchanges. In this context, there is no basis for use of the kernel function of Sec. 2 to change the kinetic energy of the w profile. Therefore an eddy event now involves only a triplet map.

Eq. (15) for the event rate distribution is applicable, where now $\alpha = 0$ and $v_{2,K}$ is replaced by w_K. w_K can be evaluated by substituting w for v_i in the rightmost expression of Eq. (6). This is the recommended procedure, but the computed results shown here were obtained with an earlier formulation (Dreeben & Kerstein 2000) in which

$$w_K = \frac{4}{l}\int_{y_0}^{y_0+l} dy\, w(y)\,\mathrm{sgn}(y - y_0 - l/2). \tag{26}$$

In addition, the procedure of Sec. 2.4 for suppressing the large-eddy anomaly was not incor-

porated.

The large-eddy anomaly is not likely to have much effect on the results presented here, though it may affect model predictions of a subtle relaminarization effect seen in a related configuration involving pressure forcing as well as buoyant forcing. The effect of using Eq. (26) instead of Eq. (6) can be estimated by assuming a linear velocity profile of given slope within $[y_0, y_0 + l]$. This gives $|w_K/v_K| = 13.5$. Computed results for several flows have been compared by using this factor to estimate the C value for one method that is equivalent to the C value for the other. The two sets of results were close, indicating that this parameter conversion largely accounts for the difference between the formulations.

For the computed results shown here, parameter values converted on this basis into estimated values for the model formulation of Sec. 2 are $C = 3.1$ and $Z = 0.27$. The parameters were assigned by comparing channel-flow simulations to measurements (involving one free parameter because one parameter was assigned by *a priori* analysis). Comparisons to the buoyancy-driven flow involve no further parameter adjustment.

As in the simulations of Rayleigh-Bénard convection, runs were started from a convenient initial condition and statistics were gathered following relaxation to statistically steady evolution. The dependence of Nu (defined as in Sec. 4.3) and of the mean velocity profile on Ra and Pr is examined. DNS results, and some measurements, are available for $Pr = 0.71$ (air).

ODT mean velocity profiles are compared to measurements in Fig. 13. (Following convention, the wall-normal coordinate for this flow is denoted x rather than y.) Substantial quantitative differences are apparent, although profile shapes and the Ra dependence are well represented. The measured temperature profile is matched well in the bulk flow (Fig. 14), but the thermal boundary layer thickness is overpredicted. The measurements, performed in a closed high-aspect-ratio channel rather than an unconfined system, may be subject to recirculation and other effects that would not occur in the ideal unconfined flow.

The buoyant forcing, odd symmetry, and no-slip boundary condition result in a nonmonotonic mean velocity profile. The conventional law of the wall is not applicable to this flow. In an effort to develop a suitable alternative, Versteegh and Nieuwstadt (1999) performed DNS of this flow for a range of Ra values. They found classical Ra dependence of Nu (Fig. 15; see Sec. 4.3 for background) but nonclassical Ra dependence (not conforming to dimensional analysis based on either wall or bulk properties) of the maximum velocity (Fig. 16) and the location of the maximum (Fig. 17).

Although the plots indicate that ODT does not match the numerical results, it found that ODT reproduces the Ra dependencies of all these properties, and complements the DNS by demonstrating these dependencies over a wider Ra range. ODT has been used to further broaden the investigation by varying Pr. The Ra dependencies of w-profile properties are found to be independent of Pr (Figs. 18 and 19). Moreover, the maximum velocity appears

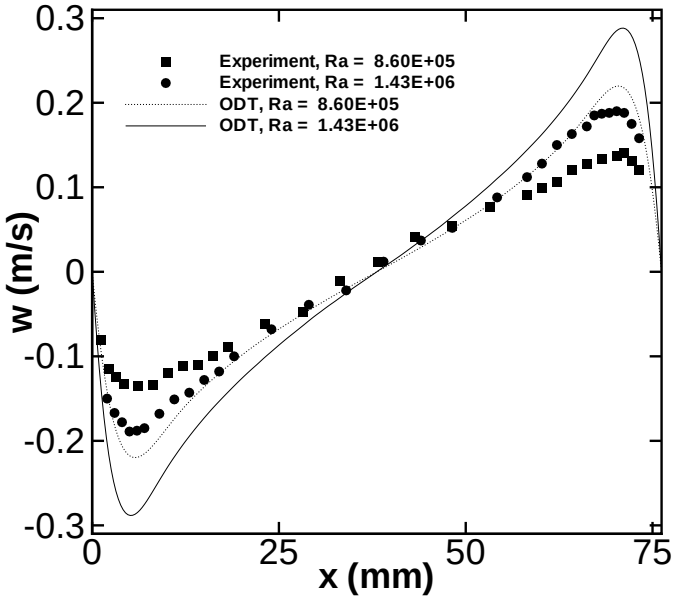

Figure 13. Computed and measured (Betts & Bokhari 1996) mean velocity profiles in buoyancy-driven vertical-channel flow.

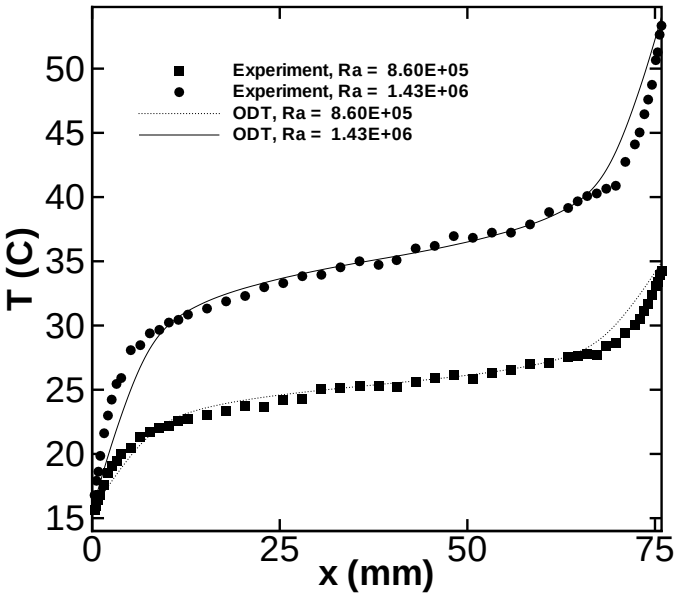

Figure 14. Computed and measured (Betts & Bokhari 1996) mean temperature profiles in buoyancy-driven vertical-channel flow.

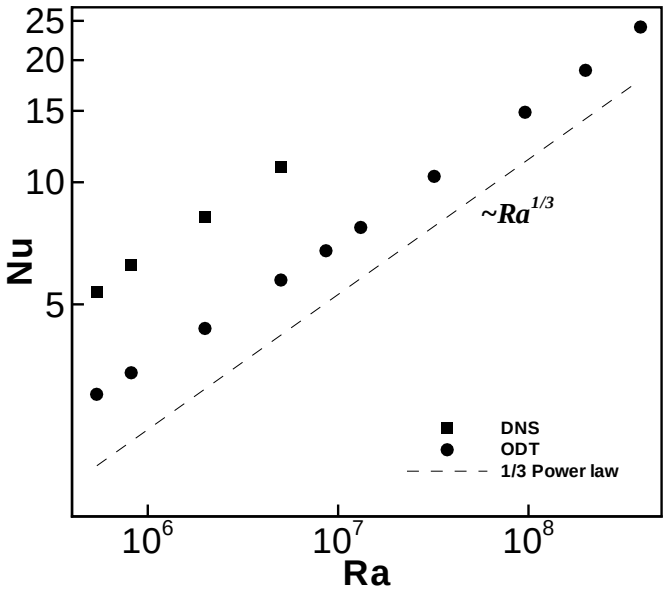

Figure 15. Computed dependence of Nu on Ra in buoyancy-driven vertical-channel flow for $Pr = 0.71$. $---$, classical scaling.

to scale as $(RaPr)^{1/2}$, which is the outer (bulk) scaling predicted if $\Delta\rho$ is substituted for the mean heat flux in the dimensional analysis (Dreeben & Kerstein 2000). Nieuwstadt & Versteegh (1997) note a theoretical inconsistency of this scaling, so the significance of this observation is unclear. No theoretical interpretation of the $Ra^{-1/6}$ dependence of the location of the maximum has been proposed.

Curiously, the Nu scaling at $Pr = 0.71$ is the property most consistent with theory, but ODT suggests that it is the least tractable property when a range of Pr values is considered. Figure 20 indicates that the scaling exponent is an increasing function of Pr, suggesting that the apparent classical scaling reflects crossing of the classical value at a particular Pr. This surprising result indicates that parameter studies using ODT may be useful for physics discovery and for identification of interesting parameter regimes for follow-up DNS studies.

These results also provide some indication of the potential strengths and weaknesses of ODT as a near-wall subgrid model for LES. The capability of ODT to reproduce parameter dependencies of turbulent flows has not yet been explained. Though the demonstrated performance of ODT indicates its potential value as a subgrid model, the lack of theoretical explanation requires that extrapolation of the model far beyond validated regimes should be regarded as plausible but speculative. In many respects, ODT has shown itself to be the tool of choice for subgrid modeling, but it should not be considered the definitive solution to the LES subgrid closure problem.

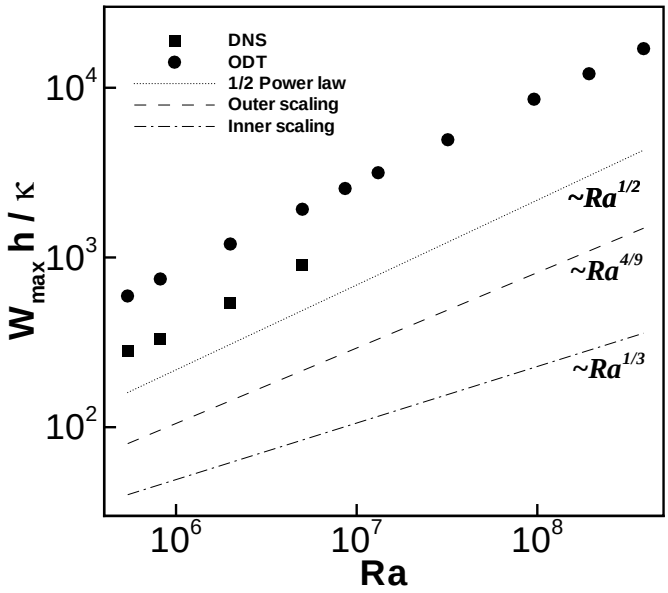

Figure 16. Computed dependence of the maximum value of the scaled mean velocity profile on Ra in buoyancy-driven vertical-channel flow for $Pr = 0.71$.

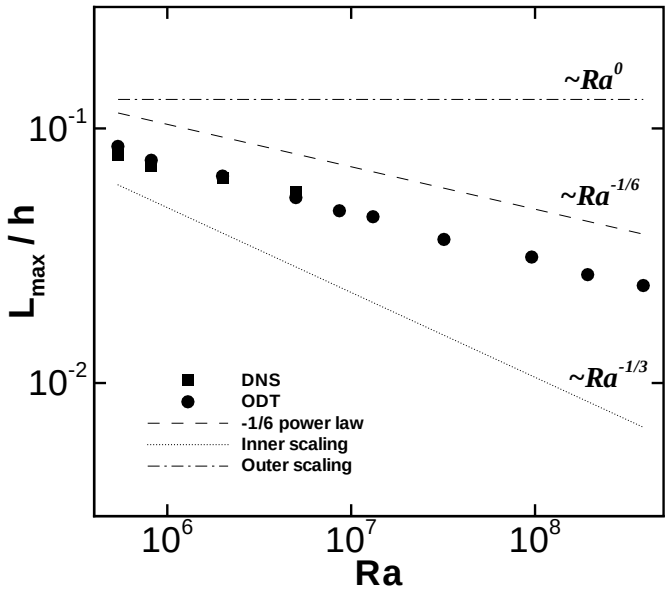

Figure 17. Computed dependence of the scaled location of the maximum velocity on Ra in buoyancy-driven vertical-channel flow for $Pr = 0.71$.

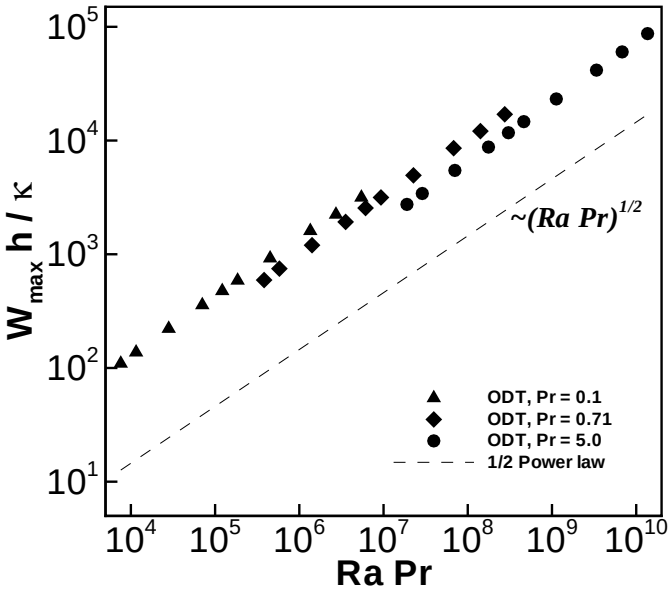

Figure 18. Computed dependence of the maximum value of the scaled mean velocity profile on $RaPr$ in buoyancy-driven vertical-channel flow.

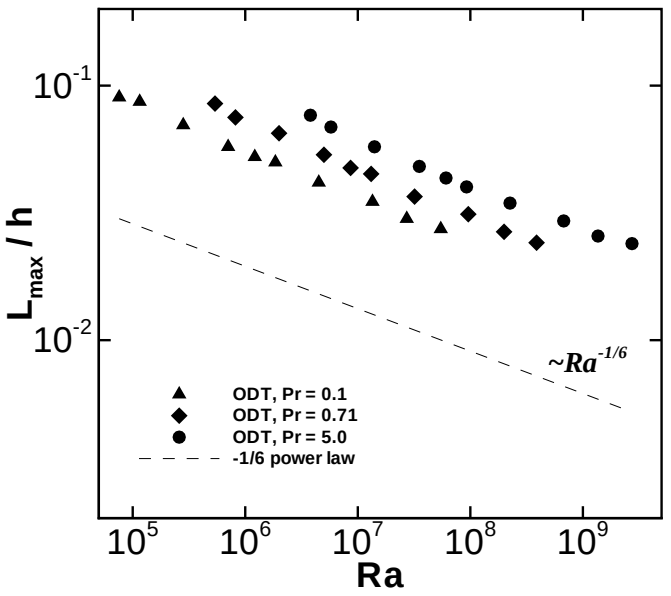

Figure 19. Computed dependence of the scaled location of the maximum velocity on Ra in buoyancy-driven vertical-channel flow for three Pr values.

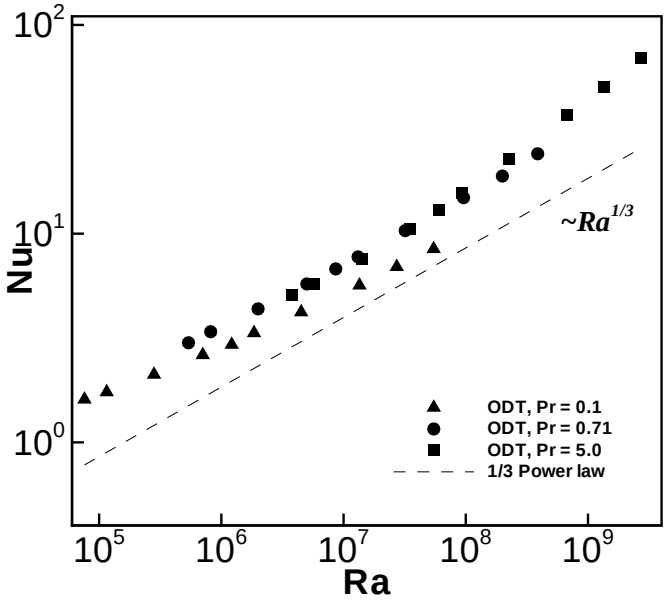

Figure 20. Computed dependence of Nu on Ra in buoyancy-driven vertical-channel flow for three Pr values.

5 Incorporation of the Near-Wall Model into a Large Eddy Simulation

5.1 Problem Definition

To understand the role of ODT as a subgrid closure coupled to an LES code, it is first necessary to examine the physical assumptions and approximations underlying the LES method. Specifically, an LES model of the incompressible Navier-Stokes equations is considered.

At a minimum, LES is intended to reproduce the structure and time evolution of the largest scales of turbulent flow. These scales are forced by applied shear (free shear or shear at walls) and/or by applied pressure gradients. Here, only constant property (including density) flow is considered. The vortical flow that develops in response to these forcings cascades to fine scales where the vortical kinetic energy is dissipated by viscosity.

If the viscous dissipation scales are not resolved, a model must be introduced in order to dissipate the vortical kinetic energy. Conceptually, this is accomplished by introducing an eddy viscosity designed to dissipate, at or near the grid resolution scale, the amount of energy that would otherwise (in a fully resolved flow) flux to smaller scales and ultimately dissipate. The primary challenge of LES development is to formulate a dissipation mechanism that achieves this goal.

Though accurate energy dissipation is a key objective of LES modeling, it is recognized

that physical interaction between the fine scales and the large scales involves more than one-way energy transfer. The 'back-scatter' of energy from fine to large scales is represented in some LES formulations. For multiphysics problems involving fine-scale vorticity generation, e.g., due to combustion-driven thermal expansion, this reverse energy flow can be a dominant feature of the overall flow.

The ODT subgrid implementation introduced here is intended to be the first step toward a full multiphysics subgrid treatment. The results presented in Sec. 4 provide an indication of the potential usefulness of ODT in this regard. Rather than tackling this problem in its full generality, a more limited yet almost universal issue confronting LES is addressed. This issue is near-wall momentum closure.

As discussed in Sec. 1, the dominant flow scale in turbulent flow near a wall is the distance from the wall. Thus, increasingly fine scales must be resolved to maintain accuracy of the LES model as the wall is approached, ultimately requiring some resolution of the viscous scale. Some LES formulations provide the needed resolution, but the computational cost limits the applicability of this approach. The common alternative is to use empirical wall functions or related empirical approaches.

Recognizing the inevitability of some empiricism in an affordable general-purpose wall treatment, it is proposed that ODT may provide a cost-effective framework for introducing the needed empiricism. ODT has two key attributes in this regard. First, it introduces a time-lagged response of near-wall flow and wall stress to bulk forcing, and of bulk flow to wall effects. In particular, near-wall response to flow reversals and other transients should evolve more realistically than the response of an empirical wall function. Second, the model should readily generalize to at least some of the multiphysics regimes of practical importance.

Near-wall momentum closure is a practical near-term target for ODT because the near-wall region is a small fraction of the total fluid volume. Detailed simulation within this region is affordable relative to the total computational cost of the LES, as shown in Sec. 6.2. Moreover, the region of interest is fixed in time (unlike combustion problems in which the flame region requiring submodeling is advected by the flow), and property variations are strongest in a fixed direction (wall normal), implying fixed locations and orientations of the ODT domains.

Another motivation for attempting near-wall momentum closure is the strong interest in this problem in the academic research community. A successful approach to this problem will engage the attention and involvement of this community and thereby accelerate progress toward high fidelity turbulent multiphysics simulation.

5.2 Formulation of the LES Equations

5.2.1 Filtering and the Filtered Equations

A fundamental component of all LES models is the definition of spatially filtered variables (generally denoted by the overbar) such that the following relationship holds:

$$\phi = \bar{\phi} + \phi'. \tag{27}$$

Here ϕ is a generic physical quantity, with $\bar{\phi}$ its filtered value and ϕ' the instantaneous difference between ϕ and $\bar{\phi}$. (Note that each of these values are functions of x, y, z, and t.) The filtering operation is defined as

$$\bar{\phi}(\mathbf{x}, t) = \int_D \phi(\mathbf{x}, t) G(\mathbf{x} - \mathbf{z}, \Delta)\, d\mathbf{z}, \tag{28}$$

where G is a normalized filter kernel, D is the domain of the flow, and Δ is the filter width in each spatial direction. The shape and spatial extent of the filter applied is a modeling choice. For example, if the filter is defined as a box filter, then the value of $\bar{\phi}$ is simply the instantaneous average value of ϕ within the domain enclosed by the box.

The classic way to develop the LES equations of motion is to begin by making the assumption that the filtering operation commutes with differentiation. Under this assumption, one can directly apply the filtering operation to the continuity and Navier-Stokes equations. For an incompressible fluid with constant properties this yields the following LES equations of motion:

$$\rho \frac{\partial \bar{u}_i}{\partial t} + \rho \frac{\partial}{\partial x_j}(\overline{u_i u_j}) = -\frac{\partial \bar{p}}{\partial x_i} + \frac{\partial}{\partial x_j}\left[\mu\left(\frac{\partial \bar{u}_i}{\partial x_j}\right)\right] + \rho \bar{f}_i \tag{29}$$

$$\frac{\partial \bar{u}_i}{\partial x_i} = 0. \tag{30}$$

At this point a closure model must be chosen for the nonlinear advective term that arises (see the second term in Eq. (29)). Examples of these will be reviewed later.

Finally, since exact solutions of these equations are not possible, one cannot avoid the further step of choosing and implementing a numerical discretization scheme (e.g., finite difference, control volume, finite element, etc.) in order to define a set of discrete LES equations that can be solved on a finite grid.

An alternative way to develop the discrete LES equations is described by Schumann (1973, 1975). In this approach, called the 'volume-balance method,' the averaged quantities correspond to a discrete number of volumes that are fixed in space (i.e., the mesh). In essence, it is simply a control-volume numerical scheme developed for LES. The governing equations are integrated by parts to obtain discrete budget equations for the individual mesh cells. The modeling problem then reduces to how to represent accurately the unresolved surface fluxes in terms of the spatially averaged quantities that are available. An advantage of this

method is that irregular or anisotropic meshes do not introduce fundamental errors. (For the classic approach with non-uniform meshes, filter commutativity becomes a problem.) Adopting Schumann's notation, the discrete momentum equation that would correspond to Eq. (29) above can be written as

$$\rho\frac{\partial\bar{u}_i}{\partial t}+\rho\delta_j(\overline{\overline{u_i u_j}}^S)=-\delta_i\bar{p}+\delta_j\left[\mu\left(\overline{\frac{\partial u_i}{\partial x_j}}^S\right)\right]+\rho\bar{f}_i, \tag{31}$$

where δ denotes a numerical-difference operator, and the advective and diffusive flux terms are averages over surfaces, not volume averages.

5.2.2 Gradient-Diffusion Closure

It is common in the literature to define a subgrid-scale stress tensor as follows:

$$\tau_{ij}=\overline{u_i u_j}-\bar{u}_i\bar{u}_j. \tag{32}$$

Dropping the body-force term for simplicity, Eq. (29) is then rewritten as

$$\rho\frac{\partial\bar{u}_i}{\partial t}+\rho\frac{\partial}{\partial x_j}(\bar{u}_i\bar{u}_j)=-\frac{\partial\bar{p}}{\partial x_i}+\frac{\partial}{\partial x_j}\left[\mu\left(\frac{\partial\bar{u}_i}{\partial x_j}\right)\right]-\frac{\partial}{\partial x_j}\tau_{ij}. \tag{33}$$

Gradient-diffusion models (other models will not be reviewed here) adopt the following hypothesis, which consists of assuming that the anisotropic part of the subgrid-scale stress tensor τ is proportional to the resolved (large scale) strain-rate tensor $\mathbf{S}$:

$$\tau_{ij}-\frac{1}{3}\delta_{ij}\tau_{kk}=-2\mu_S\bar{\mathbf{S}}_{ij} \tag{34}$$

$$\bar{\mathbf{S}}_{ij}=\frac{1}{2}\left(\frac{\partial\bar{u}_i}{\partial x_j}+\frac{\partial\bar{u}_j}{\partial x_i}\right), \tag{35}$$

where μ_S is a subgrid eddy viscosity, which must be computed from an appropriate model, and δ_{ij} is the Kronecker delta. By defining a modified pressure $\bar{P}$ that includes the subgrid kinetic energy (i.e., the trace of τ) and performing the appropriate algebraic substitutions and manipulations (see for example Ciofalo 1994), Eq. (33) can be expressed as

$$\rho\frac{\partial\bar{u}_i}{\partial t}+\rho\frac{\partial}{\partial x_j}(\bar{u}_i\bar{u}_j)=-\frac{\partial\bar{P}}{\partial x_i}+\frac{\partial}{\partial x_j}\left[(\mu+\mu_S)\left(\frac{\partial\bar{u}_i}{\partial x_j}\right)\right]. \tag{36}$$

5.2.3 Smagorinsky Model for the Subgrid Eddy Viscosity

The first model for the subgrid eddy viscosity was introduced by Smagorinsky (1963) and it remains, together with its variants, a widely applied model. It can be written compactly as

$$\mu_S=\rho(C_S\Delta)^2(2\bar{\mathbf{S}}_{ij}\bar{\mathbf{S}}_{ij})^{1/2} \tag{37}$$

where C_S is called the Smagorinsky constant, and the characteristic filter width Δ is generally computed as the cube root of the local cell volume:

$$\Delta = (\Delta x_1 \Delta x_2 \Delta x_3)^{1/3}. \tag{38}$$

Substitution of Eq. (37) into Eq. (34) yields

$$\tau_{ij} - \frac{1}{3}\delta_{ij}\tau_{kk} = -2\rho(C_S\Delta)^2|\bar{\mathbf{S}}|\,\bar{\mathbf{S}}_{ij} \tag{39}$$

where $|\bar{\mathbf{S}}| = (2\bar{\mathbf{S}}_{ij}\bar{\mathbf{S}}_{ij})^{1/2}$.

5.2.4 Dynamic Smagorinsky Model for the Subgrid Eddy Viscosity

A method for dynamically adjusting the Smagorinsky constant to the local features of the flow was first suggested by Germano *et al.* (1991). The basic idea is to assume that the constant in the eddy-viscosity relationship is the same for a second filter of larger width Δ'. Given this second filter, typically referred to as the test filter, we can define a second subgrid-scale stress tensor $\mathbf{T}_{ij}$ as follows,

$$\mathbf{T}_{ij} = \widetilde{\overline{u_i u_j}} - \tilde{\bar{u}}_i \tilde{\bar{u}}_j. \tag{40}$$

Tilde denotes the test filter, here applied to quantities that have already been subject to a filter of width Δ. We now note that the difference between this tensor $\mathbf{T}$ and the filtered value of τ (using the test filter) can be written in terms of quantities that can be computed, i.e.,

$$\mathbf{L}_{ij} = \mathbf{T}_{ij} - \tilde{\tau}_{ij} = \widetilde{\bar{u}_i \bar{u}_j} - \tilde{\bar{u}}_i \tilde{\bar{u}}_j. \tag{41}$$

If we apply the assumption that the Smagorinsky constant is the same at both filter widths, then we can write

$$\widetilde{\bar{u}_i \bar{u}_j} - \tilde{\bar{u}}_i \tilde{\bar{u}}_j = 2\rho(C_S\Delta')^2|\bar{\mathbf{S}}'|\,\bar{\mathbf{S}}'_{ij} - 2\rho(C_S\widetilde{\Delta})^2|\bar{\mathbf{S}}|\,\bar{\mathbf{S}}_{ij}, \tag{42}$$

where the wide tilde over the rightmost term indicates test filtering of the entire term. This is an overdetermined but closed system of equations for the Smagorinsky constant C_S. The most common method of dealing with the overdeterminancy is to use the least-squares solution described by Lilly (1992). However, the fact that C_S appears inside the filtering operation (second term on the right-hand side of Eq. (42)) introduces some additional mathematical and practical problems for which various solutions have been proposed. These are discussed by Ghosal *et al.* (1995), and a dynamic localization procedure is proposed which uses a constrained variational formulation.

For flows with two homogeneous directions, such as fully developed turbulent flow between parallel plates, the following formula is obtained:

$$(C_S(y,t))^2 = \left[\frac{\langle \mathbf{m}_{ij}\mathbf{L}_{ij}\rangle_{xz}}{\langle \mathbf{m}_{kl}\mathbf{m}_{kl}\rangle_{xz}}\right]_+, \tag{43}$$

where $\mathbf{m}_{ij} = 2\rho(\Delta')^2|\bar{\mathbf{S}}'|\,\bar{\mathbf{S}}'_{ij} - 2\rho\widetilde{(\Delta)^2|\bar{\mathbf{S}}|\,\bar{\mathbf{S}}}_{ij}$, $\langle\rangle_{xz}$ denotes integration over a layer of finite thickness in the xz plane, and the brackets with a + subscript denote the operation of taking the positive part, i.e., $[x]_+ = \frac{1}{2}(x + |x|)$ for any real number x.

5.3 Formulation of an ODT-Based Near-Wall Subgrid Model

5.3.1 Modeling Approach

The conceptual idea and overall goal behind coupling ODT to LES in the near wall region is quite simple. We seek a method which allows us to use the highly resolved (in 1D space) ODT model near all no-slip walls, and some form of traditional 3D LES turbulence modeling everywhere else.

As one considers the differences between LES and ODT, it is clear that several fundamental issues must be addressed in order for this conceptual idea to be realized. These include questions about how to:

1. relate 1D ODT variables to spatially filtered LES variables, and provide appropriate ODT/LES interface boundary conditions,
2. account for 3D advection effects when ODT is 1D,
3. address 3D continuity constraints on control volumes associated with 1D ODT domains,
4. allow for eddy events to span between ODT and LES resolved space, and
5. couple small ODT time-integration steps with much larger LES time-integration steps.

One approach (there may be others) for which each of these questions has been worked out is described below.

5.3.2 Geometric Considerations

The ODT/LES wall model developed here affects the LES equations in two distinct near-wall regions, as illustrated in Fig. 21. For reference purposes, we will call the layer of LES cells that are immediately adjacent to the no-slip wall the ODT inner region. It is in this region that the ODT model will be primarily active. An additional set of LES cell layers, the number of which will be a model parameter, defines the ODT outer region. The flow in this domain is primarily controlled by standard LES equations, but is also affected by an ODT/LES coupling that diminishes in strength with distance from the wall (details to be described below).

From an LES perspective, we begin by conceptualizing all LES cells that lie adjacent to solid walls (i.e., the inner ODT region) in the framework of the volume-balance LES model

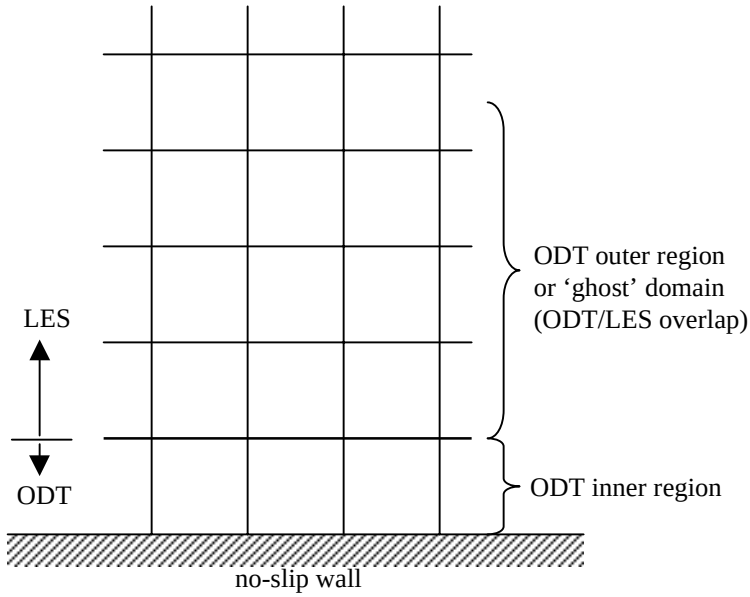

Figure 21. Illustration of the ODT inner and outer region domains in the LES mesh.

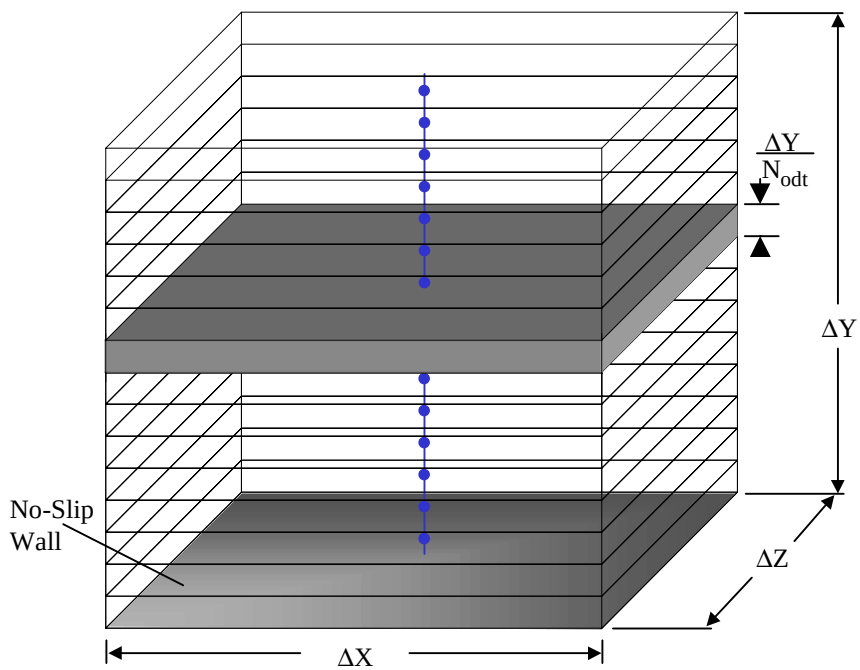

Figure 22. ODT sub-volumes imbedded in an 'inner-region' LES control volume.

developed by Schumann (1975) (see Eq. (31)). Associated with each of these inner-region control volumes, we define an ODT line that begins at the no-slip wall and extends upward to the top of the control volume. All three ODT velocity components as well as any scalar quantities of interest, except pressure, are spatially resolved in the wall-normal direction on the ODT lines. Pressure is only resolved on the LES-scale mesh (i.e., one value per LES control volume), reflecting that 3D continuity constraints are only imposed by pressure on the LES grid.

We now define a relationship between ODT variables in the inner region and their corresponding instantaneous spatially averaged LES values as follows:

$$\bar{\phi} = \frac{1}{N_{\mathrm{ODT}}} \sum_{m=1}^{N_{\mathrm{ODT}}} \phi_m, \tag{44}$$

where ϕ denotes a generic variable, and N_{ODT} is the number of ODT points on the ODT line. Equation (44) implies that the ODT-resolved variable ϕ_m represents an instantaneous volume average over a control volume of height $\Delta Y/N_{\mathrm{ODT}}$ at location $y = y_m$. This is illustrated pictorially in Fig. 22, where an array of ODT sub-volumes imbedded in a near-wall LES control volume is depicted. In effect, each point on the ODT line is conceptualized as an LES sub-control volume in exactly the same sense as developed by Schumann, only in this case, the resolution in the wall-normal direction is very fine.

5.3.3 Revised ODT Evolution Equations

ODT as a standalone model is a closed system that consists of a single ODT line. However, as a near-wall LES subgrid model, the formulation must be extended to allow for advective transport between neighboring ODT sub-volumes in adjacent LES control volumes. Enforcement of continuity within these control volumes then implies a wall-normal LES-scale advective-transport contribution. (Wall-normal LES-scale advective transport induced by eddy events is discussed in Sec. 5.3.4.) This is accomplished by modifying the ODT evolution equations (see Eqs. (1) and (2)) to include advective transport terms as follows:

$$\left(\partial_t - \nu\partial_{x_2}^2\right) v_i(y,t) + \partial_{x_j}\left(V_j(y,t) v_i(y,t)\right) + \frac{1}{\rho}\left.\frac{\partial \bar{P}}{\partial x_i}\right|_{i\neq 2} = 0 \tag{45}$$

$$\left(\partial_t - \nu\partial_{x_2}^2\right) \theta(y,t) + \partial_{x_j}\left(V_j(y,t)\theta(y,t)\right) = 0. \tag{46}$$

Here, the mean pressure gradient has been included except in the wall-normal direction ($i = 2$), and a local advective velocity field $V_j(y,t)$, has been introduced. Taking $V_1(y,t)$ and $V_3(y,t)$ to be $v_1(y,t)$ and $v_3(y,t)$ respectively gives a formally valid representation of lateral transport. However, definitions of V_1 and V_3 that involve temporal filtering of v_1 and v_3 are preferred because the spatial derivatives in the $i = 1$ and $i = 3$ directions in Eqs. (45) and

(46) are implemented numerically as spatial differences over LES-scale spatial increments ΔX and ΔZ, respectively, as illustrated by the ODT/LES control-volume geometry sketched in Fig. 22. In view of the coarseness of the X and Z resolution relative to the Y resolution, the convective time scale for property transfer between laterally adjacent ODT sub-volumes is the LES time scale Δt rather than the fine-grained time scale on which other ODT processes, governed by Eqs. (45) and (46), evolve. Accordingly, temporal filtering suppresses unphysical high-frequency fluctuations due to the more rapid evolution processes implemented in the vertical direction (which can be resolved temporally owing to the finer spatial resolution in that direction). These considerations are analogous to time-stepping issues that arise in any numerical scheme involving high-aspect-ratio control volumes. From an operational standpoint, the temporal filtering is useful when implementing the ODT/LES model in the context of a pressure-projection type numerical time-integration method. The numerical integration method used in the present implementation is described in Sec. 5.5.

A simple temporal filter that would serve this purpose is

$$V_1(y,t) = \frac{1}{\Delta t}\int_{t-\Delta t}^{t} v_1(y,t')\,dt' \tag{47}$$

$$V_3(y,t) = \frac{1}{\Delta t}\int_{t-\Delta t}^{t} v_3(y,t')\,dt', \tag{48}$$

where Δt is the LES time step. A computationally more convenient definition that serves the same purpose is introduced in Sec. 5.5.2.

There is an important distinction between the instantaneous wall-normal velocity component v_2 and the instantaneous tangential velocity components v_1 and v_3. In the approach developed here, v_1 and v_3 are treated as 'real' velocities, i.e., they are advecting velocities, and we compute V_1 and V_3 from them as described in Sec. 5.5.2. However, v_2 is not considered an advecting velocity because eddy events are the model for turbulent transport in the wall-normal direction. Instead we conceptualize v_2 as simply related to the wall-normal velocity component kinetic energy (actually the square root of that energy). Thus, no pressure gradient is included in the evolution equation for v_2. To compute the mean advective transport velocity in the wall-normal direction, V_2, we simply apply continuity and integrate from the wall, as follows:

$$V_2(y,t) = -\int_0^y \left(\frac{\partial V_1}{\partial x_1} + \frac{\partial V_3}{\partial x_3}\right) dy. \tag{49}$$

Note that this automatically satisfies continuity within the LES-scale control volume.

The ODT evolution equations are only solved in the inner region. Thus, boundary conditions must be applied both at the wall ($y = 0$) and at the top of the inner region ($y = \Delta Y$). At $y = \Delta Y$ this is accomplished by assuming a linear variation of all velocity components at every instant in time between the last ODT node ($y = \Delta Y$) and the corresponding LES

values in the outer region at $y = \frac{3}{2}\Delta Y$. Given this assumption, all required boundary fluxes (both advective and diffusive) can be computed based on the boundary conditions at $y = 0$:

$$v_1 = v_2 = v_3 = 0$$
$$V_2 = 0 \tag{50}$$

and at $y = \Delta Y$:

$$\frac{\partial v_i}{\partial x_2} = \left(\bar{u}_i|_{y=(3/2)\Delta Y} - v_i|_{y=\Delta Y} \right) / [(3/2)\Delta Y]. \tag{51}$$

Note that in Eq. (51), $\bar{u}_i|_{y=(3/2)\Delta Y}$ denotes the current value of the corresponding LES velocity at a distance from the wall equal to $\frac{3}{2}\Delta Y$.

5.3.4 ODT/LES Eddy Events

Although the ODT evolution equations are only solved in the inner region, eddy events can extend from any location within the inner region out into the LES domain. In standalone ODT, the length scale of the largest possible eddy event, $L_{\max}$, corresponds to the integral scale of the flow problem. For example, in channel flow the largest possible eddy is limited by the distance between the two walls. However, as an LES subgrid model ODT must only model the unresolved small scale eddies. Independent of filter type, the smallest possible eddy that can be resolved on the grid by an LES is 2Δ (sometimes called the Nyquist limit), and this will not be a very accurate representation. In practice, both the numerical method and the particular filter type chosen will determine the length-scale range over which the resolution of smaller eddies degrades. When ODT is modeling the LES subgrid processes, the value for $L_{\max}$ must correspond to these same limits. In other words, the largest length scales modeled by ODT must correspond to the smallest length scales captured by the LES.

Figure 23 illustrates how all eddy events must extend down into the inner region, but that given a large eddy, it is possible for one to extend out as far as $\Delta Y + L_{\max}$. Thus, the value of $L_{\max}$ determines the length of the outer (or overlap) region.

To obtain ODT-resolved information in the outer region, linear interpolation of the LES-scale variables is used to provide 'ghost-node' ODT values at any location that is required. Eddy events that extend across LES control volumes result in transfer of fluid properties (momentum, mass fractions, etc.) across those LES control-volume boundaries. Therefore the fluxes corresponding to these transfers are summed at each interface. These accumulated fluxes are incorporated into the LES time-stepping scheme, both to enforce consistency between ODT and LES evolution and to evaluate unclosed terms in the LES evolution equations. Note that the LES-scale properties at the LES node points are considered unchanged during the fine-grained ODT time evolution.

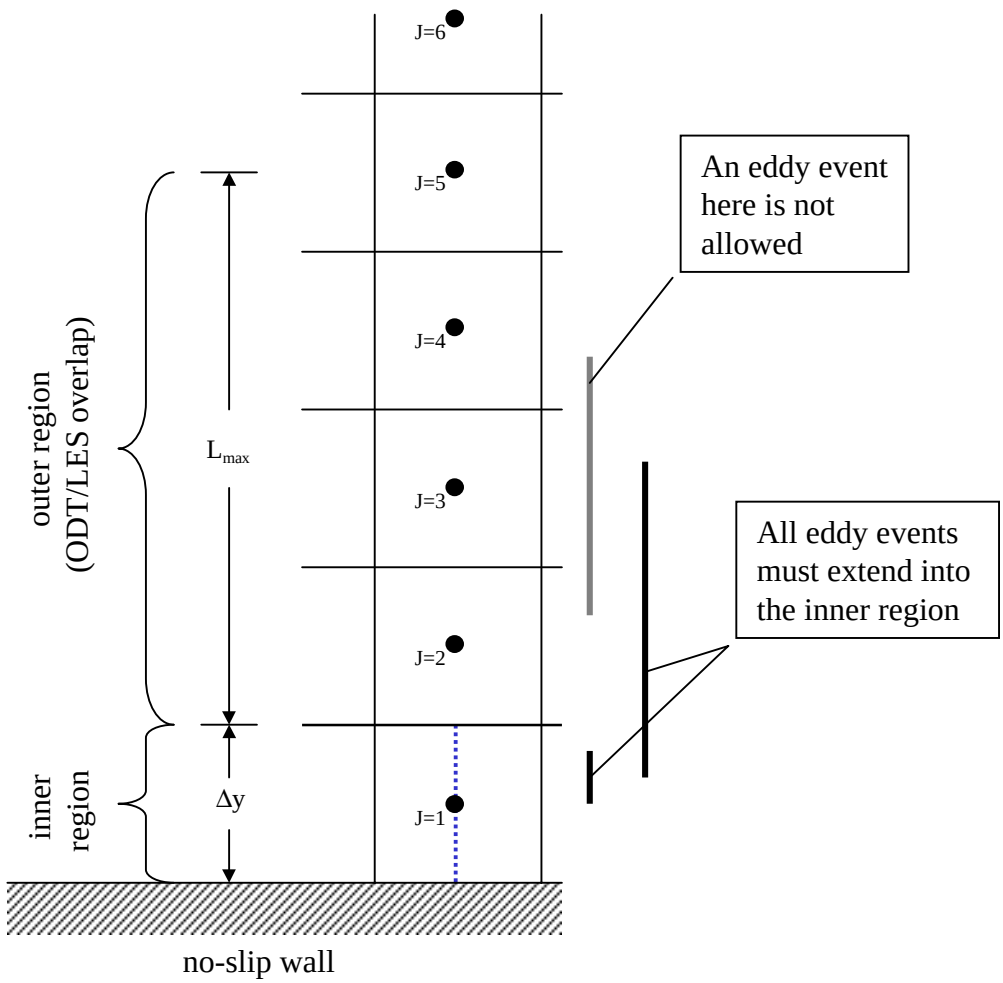

Figure 23. Illustration of allowable eddy events within the inner and outer ODT regions.

5.3.5 Synopsis of the Coupled ODT/LES Model

As modeled here, the equations simulating the turbulent flow are distinct in each of the three flow regions, i.e., the ODT inner region, the ODT/LES overlap region, and the LES core-flow region.

In the ODT inner region, Eqs. (45) and (46) are solved subject to the boundary conditions given by Eqs. (50) and (51), and the definition of the advecting velocities in Sec. 5.5.2 (with $V_2(y,t)$ defined by Eq. (49)).

In the ODT/LES overlap region, Eq. (31) is solved subject to a flux-matching condition at the ODT/LES interface (i.e., $y = \Delta Y$). This flux includes both a time-continuous contribution from Eq. (49) and the instantaneous transport across wall-normal LES control-volume interfaces due to eddy events extending outward from the ODT inner region (see Fig. 23).

When an instantaneous eddy event occurs, time-accurate implementation of conservation laws would require all affected LES quantities to be adjusted based on the net transport across each LES control-volume face. However, in practice, the LES equations of motion are solved numerically using time steps that are much larger than those required by the ODT subgrid model. In the current numerical implementation, explicit ODT/LES coupling across is accomplished by accumulating the net transfer across each LES control-volume interface (from all processes) during the ODT evolution within an LES time step. The net transfer is summed during this time period and then divided by the LES time step - thus providing an explicit flux value for input to the LES equations, in lieu of instantaneous adjustment of LES values when eddy events occur. These inputs supplement LES fluxes in the ODT/LES overlap region that are modeled based on the LES model chosen for the bulk flow. Details are provided in Sec. 5.5.

In the LES core-flow region, the LES equations associated with the base LES model chosen for the simulation are solved without modification. The LES code used in this work incorporates gradient-diffusion closure (Sec. 5.2.2) with the dynamic Smagorinsky model for the subgrid eddy viscosity (Sec. 5.2.4).

5.4 Description of the LES Simulation Code

The base LES code used for testing the near-wall ODT subgrid model is a structured-grid second-order finite-difference code specifically designed for doing channel flow (Morinishi 1995), and was obtained from Stanford University through our collaboration with the Center for Turbulence Research. In this code, periodic boundary conditions are imposed in the streamwise (x) and spanwise (z) directions and the flow is driven by a constant pressure gradient in the streamwise direction. The grid is staggered (Harlow & Welch 1965, Patankar 1980, also used by Schumann 1975) and can be stretched in the wall-normal direction using a hyperbolic-tangent mapping if desired.

A semi-implicit time-integration algorithm is used where the diffusion terms in the wall-normal direction (y) are treated implicitly with the Crank-Nicholson scheme, and a third-order Runge-Kutta scheme (Spalart *et al.* 1991) is used for all other terms. The fractional-step method of Dukowicz & Dvinsky (1992) is used in conjunction with a Van Kan (1986) type of pressure term. The corresponding Poisson equation for pressure is solved using a tri-diagonal matrix algorithm in the wall-normal direction and fast Fourier transforms (FFT) in the periodic directions.

The three-step time-advancement scheme used in the base LES code can be written in the following way:

$$\frac{\bar{u}_i^k - \bar{u}_i^{k-1}}{\Delta t} = \alpha_k \mathbf{L}_y(\bar{u}_i^{k-1}) + \beta_k \mathbf{L}_y(\bar{u}_i^k) + (\alpha_k + \beta_k)\mathbf{L}_{xz}(\bar{u}_i^{k-1}) - \gamma_k \mathbf{N}(\bar{u}_i^{k-1}) - \zeta_k \mathbf{N}(\bar{u}_i^{k-2}) - (\alpha_k + \beta_k)\frac{1}{\rho}\frac{\delta \bar{P}^k}{\delta x_i} - (\alpha_k + \beta_k)\frac{PG_i}{\rho} \tag{52}$$

$$\frac{\delta \bar{u}_i^k}{\delta x_i} = 0, \tag{53}$$

where $k = 1, 2, 3$ denotes the sub-step number, $k-2$ is ignored for $k = 1$; $\bar{u}_i^0$ and $\bar{u}_i^3$ are the LES velocities at the beginning and end of the time step; PG_i denotes the constant portion of the pressure gradient driving the channel flow (zero for $i = 2$ and 3); $\delta/\delta x_i$ denotes a finite-difference operator; and $\mathbf{N}(\bar{u}_i)$ represents the following second-order finite-difference approximation to the advection terms:

$$\mathbf{N}(\bar{u}_i) = \frac{\delta}{\delta x_j}(\bar{u}_i \bar{u}_j). \tag{54}$$

Two distinct second-order finite-difference operators for the viscous terms, $\mathbf{L}_{xz}(\bar{u}_i)$ and $\mathbf{L}_y(\bar{u}_i)$, are defined so that the implicit treatment of the wall-normal diffusion terms can be clearly distinguished:

$$\mathbf{L}_{xz}(\bar{u}_i) = \frac{\delta}{\delta x_j}\left[(\mu + \mu_S)\left(\frac{\delta \bar{u}_i}{\delta x_j}\right)\right] \tag{55}$$

$$\mathbf{L}_y(\bar{u}_i) = \frac{\delta}{\delta x_2}\left[(\mu + \mu_S)\left(\frac{\delta \bar{u}_i}{\delta x_2}\right)\right], \tag{56}$$

where the right hand side of Eq. (55) is summed over $j = 1$ and 3. The time-advancement coefficients α_k, β_k, γ_k, and ζ_k, $k = 1, 2, 3$, are constants selected such that third-order accuracy is obtained for the advection term and second-order accuracy for the viscous term. The values of these coefficients are

$$\gamma_1 = 8/15 \quad \gamma_2 = 5/12 \qquad \gamma_3 = 3/4$$

$$\zeta_1 = 0 \qquad \zeta_2 = -17/60 \quad \zeta_3 = -5/12$$

$$\alpha_1 = 4/15 \quad \alpha_2 = 1/15 \qquad \alpha_3 = 1/6$$

$$\beta_1 = 4/15 \quad \beta_2 = 1/15 \qquad \beta_3 = 1/6.$$

The effective sub-time-step for this method is $(\alpha_k + \beta_k)\Delta t$.

Applying the fractional-step method of Dukowicz & Dvinsky (1992) to Eqs. (52) and (53), we obtain

$$\frac{\hat{\bar{u}}_i^k - \bar{u}_i^{k-1}}{\Delta t} = \alpha_k \mathbf{L}_y(\bar{u}_i^{k-1}) + \beta_k \mathbf{L}_y(\hat{\bar{u}}_i^k) + (\alpha_k + \beta_k)\mathbf{L}_{xz}(\bar{u}_i^{k-1}) \\ - \gamma_k \mathbf{N}(\bar{u}_i^{k-1}) - \zeta_k \mathbf{N}(\bar{u}_i^{k-2}) - (\alpha_k + \beta_k)\frac{1}{\rho}\frac{\delta \bar{P}^{k-1}}{\delta x_i} - (\alpha_k + \beta_k)\frac{PG_i}{\rho} \qquad (57)$$

$$\frac{\bar{u}_i^k - \hat{\bar{u}}_i^k}{\Delta t} = -\frac{\delta \phi^k}{\delta x_i}, \qquad (58)$$

where ϕ^k and $\bar{P}$ are related by

$$\frac{\delta \phi^k}{\delta x_i} = (\alpha_k + \beta_k)\frac{1}{\rho}\frac{\delta}{\delta x_i}(\bar{P}^k - \bar{P}^{k-1}) - \beta_k \mathbf{L}_y(\bar{u}_i^k - \hat{\bar{u}}_i^k), \qquad (59)$$

and the hat symbol placed over a variable denotes an intermediate value which has not yet been corrected. For clarity we note that Eq. (52) can be recovered by solving for $\hat{\bar{u}}_i^k$ in Eq. (58), and then substituting this identity and that of Eq. (59) back into Eq. (57). In practice, the rightmost term in Eq. (59) is neglected, resulting in the 'splitting' error associated with this method.

Solving for $\bar{u}_i^k$ in Eq. (58) and applying the divergence-free constraint, Eq. (53), we obtain the discrete Poisson equation,

$$\frac{1}{\Delta t}\frac{\delta \hat{\bar{u}}_i^k}{\delta x_i} = \frac{\delta^2 \phi^k}{\delta x_i \delta x_i}. \qquad (60)$$

The subgrid-scale model used to compute the subgrid eddy viscosity μ_S is the dynamic Smagorinsky model of Germano (Germano *et al.* 1991) with the least-square technique of Lilly (1992) as described in Sec. 5.2.4. Averaging in homogeneous directions is used and filtering is performed in the spanwise and streamwise directions (see Eq. (43)). The ratio of the test filter to the grid filter is taken to be 2.0.

5.5 Numerical Implementation of the Near-Wall Model Within the Large-Eddy-Simulation Code

5.5.1 Overview

In Schumann's method for deriving LES equations, a direct relationship exists between the numerical discretization (mesh) and the LES filter. Thus, when associating ODT lines, care must be taken to assure that the spatial location of the ODT velocity components is consistent with the LES numerical discretization. In the staggered-grid method, the control volumes for mass and momentum are offset from one another such that the velocity components are calculated for the points that lie on the faces of the mass-conservation control volumes. Figure 24 illustrates this concept for a two-dimensional flow problem. The important point here is that the ODT velocity components must be spatially located in a consistent fashion. This is illustrated in Fig. 25, where the LES-scale velocities are represented with large arrow heads, and the locations of the associated ODT velocity components are given by the points that lie on the lines shown.

The modifications to the LES code needed to implement the ODT near-wall model can be described best by reference to the LES time-integration scheme outlined in Sec. 5.4. In this method, each of the three substeps in the Runga-Kutta algorithm consists of a two-part fractional-step cycle. The first part involves solving Eq. (57) for $\hat{\bar{u}}_i^k$, the interim velocity field. The second part is the continuity-enforcing pressure-projection step that involves solving a discrete Poisson equation for a pressure-adjusted velocity field $\bar{u}_i^k$. To use the ODT wall model, we modify this cycle to include two additional parts specific to the near-wall ODT model. In the new part 1, the ODT equations are evolved and the momentum exchange at LES interfaces due to the ODT processes are summed. Also, at the end of this part, values for $\hat{\bar{u}}_i^k$ corresponding to the ODT inner region (i.e., the layer of control volumes adjacent to the walls) are computed from these results. Details are given in Sec. 5.5.2. In part 2, a modified form of Eq. (57) is solved for $\hat{\bar{u}}_i^k$ throughout the rest of the domain. The modifications correspond to ODT contributions to the surface fluxes in the ODT/LES overlap region. (Details are provided in Sec. 5.5.3.) Part 3 is the continuity-enforcing pressure-projection step that involves solving a discrete Poisson equation for a pressure-adjusted velocity field $\bar{u}_i^k$. This part is unchanged. The fourth and final part consists of adjusting the ODT-resolved profiles of $V_i(y)$ and $v_i(y)$ to be consistent with the new pressure-adjusted LES velocity field in the inner region.

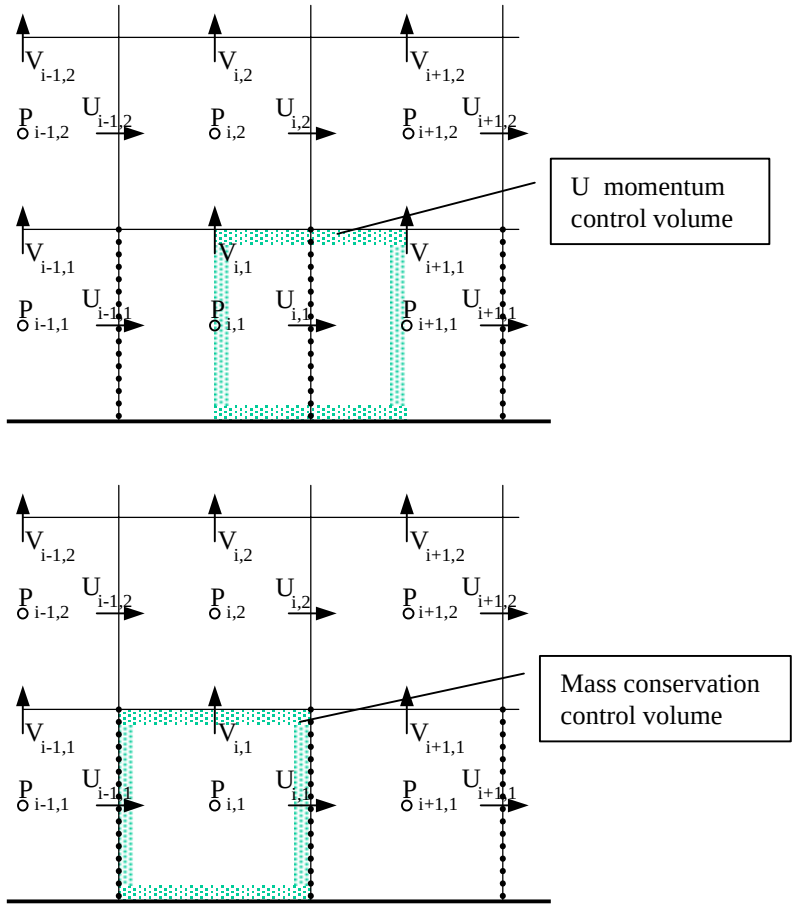

Figure 24. Illustration of offset control volumes for mass and momentum in a staggered grid.

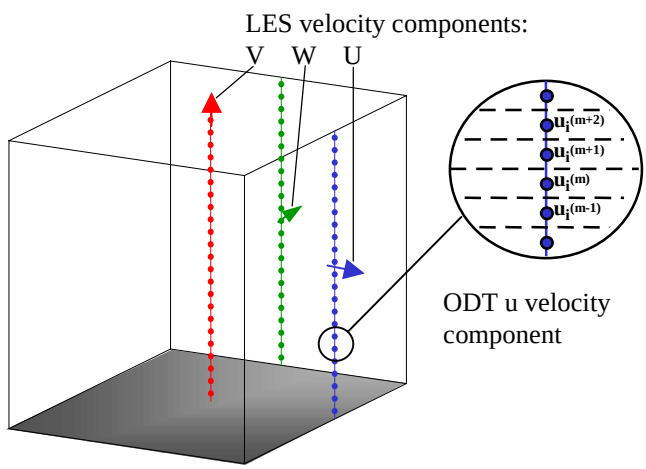

Figure 25. Spatial location of ODT and LES velocity components on a staggered grid.

5.5.2 Details of Part 1

We begin by defining an ODT time step $\Delta t'$, and the associated ODT time-step index k'. The value of $\Delta t'$ is much smaller than the LES time step Δt so that a significant number of ODT time steps must be taken to advance in time from LES substep index k to $k+1$.

Each ODT time step consists of (a) the evolution of the molecular equations from time t to $t+\Delta t'$, and (b) the stochastic sampling procedure by which eddy events are determined.

The molecular equations are numerically integrated using the following explicit numerical approximation to Eq. (45):

$$\frac{v_i^{k'} - v_i^{k'-1}}{\Delta t'} = \frac{\delta}{\delta x_2}\left(\frac{\mu}{\rho}\frac{\delta v_i^{k'-1}}{\delta x_2}\right) - \frac{\delta}{\delta x_j}\left(V_j^{k'-1} v_i^{k'-1}\right) - \frac{PG_i}{\rho}, \tag{61}$$

where PG_i denotes the constant pressure gradient imposed on the flow, which in channel flow is zero for $i = 2$ and 3. This term does not reflect the fluctuating pressure field that arises due to the turbulent fluctuations in the flow. This part of the pressure field is modeled through the pressure projection (see parts 3 and 4 below). Second-order central differencing is used to compute all gradients, and boundary conditions are imposed as per Eqs. (50) and (51).

To compute the new ODT advecting velocity field $V_i^{k'}$, an alternative to Eqs. (47) and (48) has been implemented that avoids the need to maintain a memory-intensive history of the instantaneous ODT velocity field. Namely, a temporal 'mixing-cup' approach is adopted. Given the values of V_i at time index $k'-1$, the values at k' are computed as

$$V_i^{k'} = \left(1 - \frac{\Delta t'}{\Delta t}\right) V_i^{k'-1} + \left(\frac{\Delta t'}{\Delta t}\right) v_i^{k'} \tag{62}$$

for $i = 1$ and 3 and Eq. (49) is applied for $i = 2$. We note that an alternative to using Eq. (62) (not implemented here) would be to hold $V_i^{k'}$ constant over the LES sub-step k to $k+1$, and update these values at the same time the LES velocity field is updated.

After the molecular processes have evolved from time t to $t+\Delta t'$, the possibility of an eddy event is evaluated through the standard ODT stochastic-sampling procedure (Sec. 3.3). However, allowable eddies are limited to those that extend into the inner region (as illustrated in Fig. 23), and the length of the largest possible eddy, $L_{\max}$, is a model parameter of order $4\Delta Y$ (i.e., the smallest length scale resolved by LES). If a trial-eddy location and length are chosen such that the eddy extends into the overlap region, ODT-resolved values are obtained in that region by linear interpolation of the LES field variables.

Although eddy events implemented in the usual manner would modify property profiles in the ODT/LES overlap region, the modifications are not implemented in that region. Rather, statistics are gathered, as described next, that subsequently enable LES-scale implementation of the implied property transfers across LES control-volume interfaces.

As the ODT velocity fields are advanced in time from LES substep index k to $k+1$, momentum is transferred across the ODT/LES interface through three mechanisms: molecular diffusion, wall-normal advection, and eddy events. In addition, eddy events that extend to points greater than $y = 2\Delta Y$ induce an exchange of momentum between LES cells in the overlap region. In order for the ODT model to properly couple to the LES, a running sum of the net transport across all LES control-volume interfaces due to ODT processes must be maintained. For convenience in explaining the model, we define these sums as follows:

$S_i^1 = i^{\text{th}}$ component momentum transport (per unit time, mass, and area) across an interface between a near-wall LES control volume and a second-layer LES control volume.

$S_{D_i}^1 =$ that portion of S_i^1 due entirely to molecular diffusion.

$S_{A_i}^1 =$ that portion of S_i^1 due entirely to mean advection.

$S_{E_i}^1 =$ that portion of S_i^1 due entirely to ODT eddy events.

$S_{E_i}^n = i^{\text{th}}$ component momentum transport (per unit time, mass, and area) across an interface between an n^{th}-layer LES control volume ($n > 1$) and its adjacent $(n+1)$-layer LES control volume that is due to ODT eddy events.

These sums can be computed as

$$\begin{aligned} S_i^{1,k} &= \frac{\Delta t'}{\Delta t} \sum_{k'} \left(\frac{\mu}{\rho} \frac{\delta v_i^{k'-1}}{\delta x_2} \right) \Bigg|_{y=\Delta Y} - \frac{\Delta t'}{\Delta t} \sum_{k'} \left(V_2^{k'-1} v_i^{k'-1} \right) \Big|_{y=\Delta Y} + \frac{1}{\Delta t} \sum_m E_{m,i}^1 \\ &= S_{D_i}^{1,k} + S_{A_i}^{1,k} + S_{E_i}^{1,k} \end{aligned} \tag{63}$$

$$S_{E_i}^{n,k} = \frac{1}{\Delta t} \sum_m E_{m,i}^n, \tag{64}$$

where $E_{m,i}^n$ denotes a transfer of i-component momentum across an interface between LES layers n and $n+1$ due to an eddy event m. It is easily computed as the difference in momentum (after minus before) on one side of the interface following an eddy event. In Eqs. (63) and (64), the additional superscript k has been added to denote that these quantities are computed during the interval from LES substep k to $k+1$ (see Sec. 5.4).

At the end of part 1, the ODT velocity field has evolved due to advection, diffusion, and eddy events, but without a two-way coupling with the LES velocity field (which has been held constant). Part 1 is the ODT analog to solving Eq. (57) for the interim LES velocity $\hat{\tilde{u}}_i^k$. For later use in part 3 below, we apply Eq. (44) to the ODT advecting velocities to calculate the ODT-based values for interim LES velocities in the ODT inner region:

$$\hat{\tilde{u}}_i^k \Big|_{\text{inner region}} = \hat{\bar{V}}_i = \frac{1}{N_{\text{ODT}}} \sum_{m=1}^{N_{\text{ODT}}} V_{i,m} \tag{65}$$

for $i = 1$ and 3. Equation (65) is not valid for the wall-normal velocity, $i = 2$, because of the definition of the ODT control volumes and locations as illustrated in Figs. 22 and 25.

At the top of the inner region, the spatial location of the ODT advecting velocity $V_2|_{y=\Delta Y}$ corresponds exactly to that of the LES velocity. However, the LES velocity is spatially filtered over a height ΔY, and the ODT velocity over a height $\Delta Y/N_{\rm ODT}$. For use in part 3 below, the ODT velocity is actually a more accurate approximation for the desired quantity, thus we simply set

$$\hat{\bar{u}}_2^k\Big|_{\text{inner region}} = V_2|_{y=\Delta Y} \tag{66}$$

for later use in part 3 (described in Sec. 5.5.4).

5.5.3 Details of Part 2

In part 2, modified forms of Eq. (57) are solved for all values of $\hat{\bar{u}}_i^k$ outside of the ODT inner region. These modifications correspond to ODT contributions to the surface fluxes in the ODT/LES overlap region.

In the first LES layer of the overlap region, the transport across the ODT/LES interface at the top of the inner region is completely specified by the values computed in part 1 (see Sec. 5.5.2). Also, the advective flux across the top of this layer is enhanced by any contributions due to eddy events bridging this face. To account for these effects, Eq. (57) must be modified (in this layer only) as follows:

$$\begin{aligned}
\frac{\hat{\bar{u}}_i^k - \bar{u}_i^{k-1}}{\Delta t} =& \frac{1}{\Delta x_2}\left[\alpha_k(\mu+\mu_S)\left(\frac{\delta \bar{u}_i^{k-1}}{\delta x_2}\right) + \beta_k(\mu+\mu_S)\left(\frac{\delta \hat{\bar{u}}_i^{k}}{\delta x_2}\right) - (\alpha_k+\beta_k)S_{D_i}^{1,k-1}\right] \\
&+ (\alpha_k+\beta_k)\mathbf{L}_{xz}(\bar{u}_i^{k-1}) - \gamma_k \mathbf{N}_{xz}(\bar{u}_i^{k-1}) - \zeta_k \mathbf{N}_{xz}(\bar{u}_i^{k-2}) \\
&- \frac{\gamma_k}{\Delta x_2}\left[\bar{u}_i^{k-1}\bar{u}_2^{k-1} + S_{E_i}^{n,k-1} - S_{A_i}^{1,k-1} - S_{E_i}^{1,k-1}\right] \\
&- \frac{\zeta_k}{\Delta x_2}\left[\bar{u}_i^{k-2}\bar{u}_2^{k-2} + S_{E_i}^{n,k-2} - S_{A_i}^{1,k-2} - S_{E_i}^{1,k-2}\right] \\
&- (\alpha_k+\beta_k)\frac{1}{\rho}\frac{\delta \bar{P}^{k-1}}{\delta x_i} - (\alpha_k+\beta_k)\frac{PG_i}{\rho}.
\end{aligned} \tag{67}$$

Here, the modified convection operator $\mathbf{N}_{xz}$ is defined as

$$\mathbf{N}_{xz}(\bar{u}_i) = \frac{\delta}{\delta x_j}(\bar{u}_i \bar{u}_j), \tag{68}$$

where the right-hand side is summed over $j = 1$ and 3. Note that the difference between Eq. (57) and Eq. (67) is that all finite-difference terms associated with transport across the ODT/LES interface have been replaced by the explicit sums computed in part 1.

For all other LES nodes located within the overlap region (denoted by the superscript n, with $n > 1$), Eq. (57) is revised to look as follows:

$$\frac{\hat{\bar{u}}_i^k - \bar{u}_i^{k-1}}{\Delta t} = \alpha_k \mathbf{L}_y(\bar{u}_i^{k-1}) + \beta_k \mathbf{L}_y(\hat{\bar{u}}_i^k) + (\alpha_k + \beta_k)\mathbf{L}_{xz}(\bar{u}_i^{k-1}) - \gamma_k \mathbf{N}(\bar{u}_i^{k-1}) - \zeta_k \mathbf{N}(\bar{u}_i^{k-2}) - \frac{\gamma_k}{\Delta x_2}\left(S_{E_i}^{n+1,k-1} - S_{E_i}^{n,k-1}\right) - \frac{\zeta_k}{\Delta x_2}\left(S_{E_i}^{n+1,k-2} - S_{E_i}^{n,k-2}\right) - (\alpha_k + \beta_k)\frac{1}{\rho}\frac{\delta \bar{P}^{k-1}}{\delta x_i} - (\alpha_k + \beta_k)\frac{PG_i}{\rho}. \quad (69)$$

Note that the only difference between Eq. (57) and Eq. (69) is the addition of wall-normal transport terms coming from the ODT eddy events crossing LES boundaries as computed in part 1.

For LES nodes located outside of the ODT/LES overlap region, Eq. (57) is solved without modification.

5.5.4 Details of Part 3

After completing parts 1 and 2, all values of the interim velocity field have been computed. Part 3 begins by solving the discrete Poisson equation, Eq. (60), for ϕ. Knowing ϕ^k, Eq. (59) is integrated (with the rightmost term omitted, as explained in Sec. 5.4) to compute the change in pressure from $k-1$ to k. The new pressure is then given by

$$\bar{P}^k = \bar{P}^{k-1} + \frac{\phi^k}{\alpha_k + \beta_k}. \quad (70)$$

Next, Eq. (58) can be applied to solve for the new velocity field:

$$\bar{u}_i^k = \hat{\bar{u}}_i^k - \Delta t \frac{\delta \phi^k}{\delta x_i}. \quad (71)$$

5.5.5 Details of Part 4

The fourth and final part of the cycle consists of adjusting the ODT-resolved profiles of $V_i^k(y)$ and $v_i^k(y)$ to be consistent with the new pressure-adjusted velocity field in the inner region. Figure 26 is useful in explaining how this is done.

Consider an ODT advective velocity field $V_i^k(y)$ in the inner region after the completion of part 1. Since it has not been adjusted by the pressure-projection procedure, we denote this profile hereafter as $\hat{V}_i^k(y)$. It has an average value $\hat{\bar{V}}_i^k$ (see Eq. (65)), but may have an irregular variation with y. A linear profile can be drawn from $y = 0$ to $y = \Delta Y$ that passes through the value of $\hat{\bar{V}}_i^k$ at exactly $y = \Delta Y/2$. At any location y from the wall, one can compute a difference or 'variation' between the local value of $\hat{V}_i^k(y)$ and this linear function.

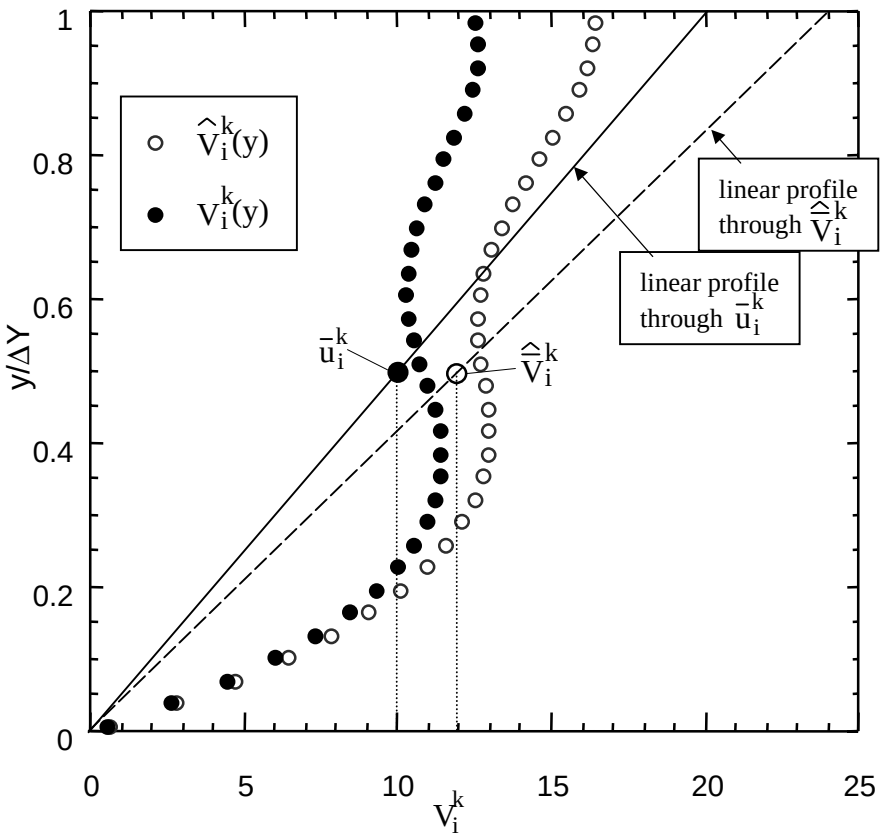

Figure 26. Illustration of how the ODT velocity field is adjusted following a pressure-projection update.

After part 3 is completed, a new adjusted value for $\bar{u}_i^k$ in the inner region is known. We impose the requirement that the difference (as a function of y) between the new $V_i^k(y)$ and a line drawn through $\bar{u}_i^k$ is unchanged from the difference function before the pressure projection. Put another way, we obtain $V_i^k(y)$ by adding a linear profile to $\hat{V}_i^k(y)$ that enforces $\bar{V}_i^k = \bar{u}_i^k$. This gives

$$V_i^k(y) - 2\frac{\bar{u}_i^k y}{\Delta Y} = \hat{V}_i^k(y) - 2\frac{\hat{\bar{V}}_i^k y}{\Delta Y} \tag{72}$$

for $i = 1$ and 3. After $V_1(y)$ and $V_3(y)$ are found, $V_2(y)$ is computed using Eq. (49).

In exactly analogous fashion, the ODT instantaneous velocity profiles are adjusted based on the relationship

$$v_i^k(y) - 2\frac{\bar{u}_i^k y}{\Delta Y} = \hat{v}_i^k(y) - 2\frac{\hat{\bar{V}}_i^k y}{\Delta Y} \tag{73}$$

for $i = 1$ and 3. At the end of part 4, all values have been advanced from LES sub-time step $k-1$ to k.

5.5.6 Remarks

The LES velocity adjustment based on the updated pressure field (Sec. 5.5.4) is the means by which the global effects of boundary conditions, inlet and outlet conditions, and other imposed forcings are communicated to the LES-resolved flow field. The corresponding adjustment of ODT velocity profiles (Sec. 5.5.5) reconciles the ODT profiles to the adjusted LES-resolved flow. The latter adjustment is formulated so that the ODT profiles are brought into conformance with the LES-resolved flow without modifying the microstructure of the ODT profiles. ODT internal processes are formulated to provide a physically sound representation of the communication of LES-scale forcings down to the microscales. Accordingly, the ODT/LES subprocesses and couplings are formulated to be complementary, each providing the other with the information needed to simulate flow evolution within the range of scales that it represents.

The ODT velocity adjustment thus accounts for the effects of large-scale forcings not incorporated into ODT microscale evolution. This does not preclude the incorporation of such forcings into ODT evolution to the extent that this can be done in a physically consistent manner. Indeed, to do so is advantageous because the adjustment procedure is approximate at best, so numerical accuracy is improved if ODT and LES evolution are well enough synchronized so that the magnitude of the adjustment is small. This is the motivation for including the mean pressure gradient in the ODT momentum equation, Eq. (45). In principle, it would likewise be advantageous to incorporate an estimate of the LES-scale pressure-gradient fluctuation, then viewing the adjustment in Sec. 5.5.5 as the correction step of a predictor-corrector procedure. To date, we have found that stability problems

typically encountered in such formulations negate the potential advantages of this approach. This does not preclude the possibility that a procedure of this type might prove advantageous in the future.

Finally, it is noted that neither the ODT momentum equation, Eq. (45), nor the adjustment in Sec. 5.5.5 communicates the large-scale forcing to the wall-normal ($i = 2$) ODT velocity component. As noted in Sec. 5.3.3, it is neither necessary nor desirable to couple v_2 to these forcings. Continuity is sufficient to determine the advective velocity V_2 that provides an LES-scale representation of the effect of ODT evolution on wall-normal flow. As in ODT standalone implementation, v_2 is a kinetic-energy reservoir that is incorporated to improve the fidelity of the ODT representation of energy transfers among the three velocity components. Owing to the distinctive role of v_2 in the formulation of the ODT event-rate distribution (Sec. 2.3), v_2 may have additional physical significance in future applications to transition and other phenomena that are sensitive to details of this formulation.

6 Performance of the Coupled ODT/LES Formulation

6.1 Computed Results and Comparison to DNS

Turbulent channel flow is chosen as the first validation test of the coupled ODT/LES model. This problem has been studied extensively in the past and both experimental and numerical DNS data is available for comparison purposes.

Figure 27 illustrates the flow domain chosen for the simulations performed here. The computational domain is 2π, $2\pi/3$, and 2 in the streamwise (x), spanwise (z), and wall-normal (y) directions, respectively. For all but the highest-Reynolds-number flows considered, the domain is discretized by a uniform $32 \times 32 \times 32$ grid in the streamwise, spanwise, and wall-normal directions. As is common in the literature, the Reynolds number used herein is based on the bulk velocity and the channel half-width (except where noted otherwise).

To perform a set of coupled ODT/LES calculations, the ODT model constants C, Z, α, and $L_{\max}$ must be specified. As in Sec. 4.2, $\alpha = 2/3$ is used for all results shown in this section. Z is again assigned the value 98. These values, together with the choice $C = 12.73$, are shown in Sec. 4.2 to yield a good fit of DNS data by standalone ODT.

For ODT/LES, it is found that a slightly lower C value, $C = 9.9$, is the best value for matching the DNS mean velocity profile at $Re_\tau = 590$. This value also yields accurate results for the friction coefficient. The performance of the model for this C value is demonstrated in the remainder of this section. Figure 28 shows the standalone ODT mean velocity profile for this C value compared to the best standalone case, $C = 12.73$. It is seen that the sensitivity is slight, but nevertheless sufficient to imply a distinction between the coupling

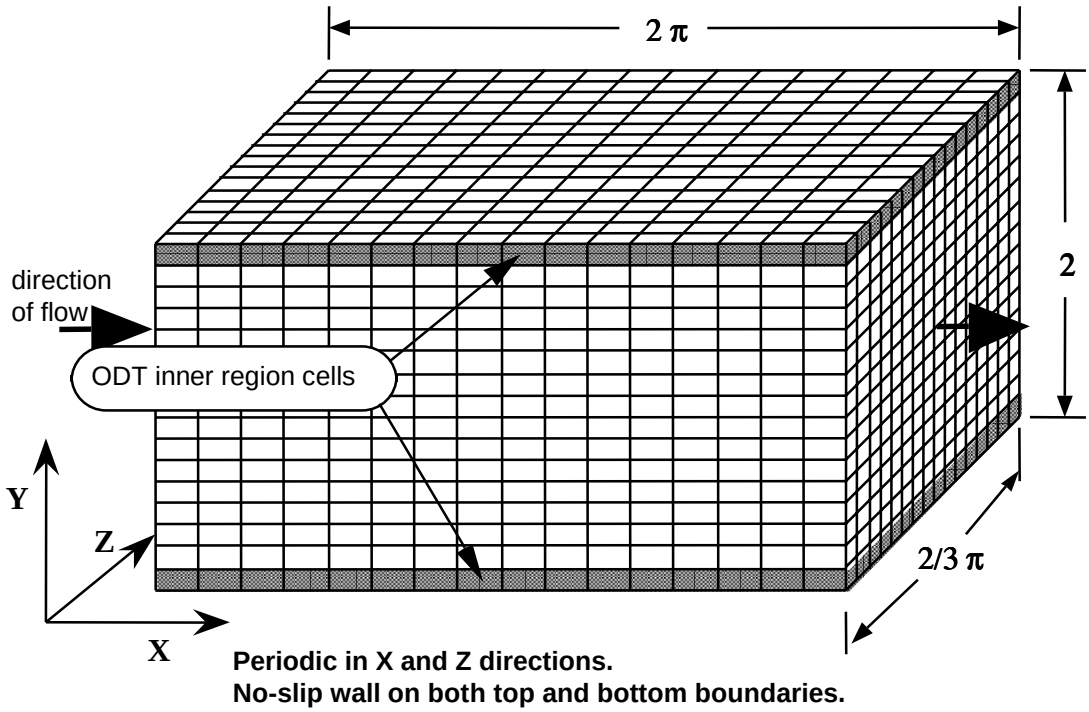

Figure 27. Illustration of the ODT/LES channel-flow validation problem domain.

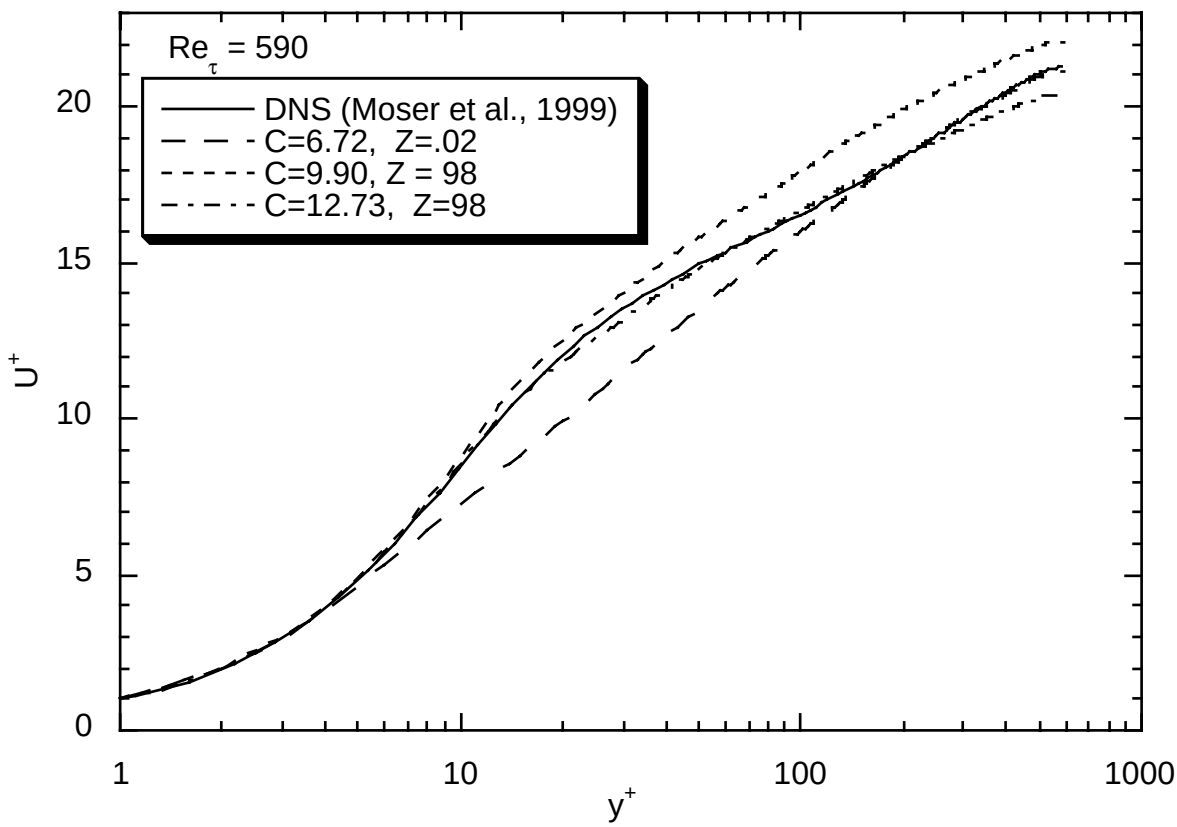

Figure 28. Sensitivity of the predicted near-wall mean velocity profiles of standalone ODT to different values of C and Z.

of near-wall and bulk regions in standalone ODT and ODT/LES, respectively. Also shown in Fig. 28 is a computed mean profile for $Z = 0.02$, a value chosen to be small enough so that Z is effectively eliminated as a model parameter (i.e., further reduction of Z does not change the computed results). C for this case is chosen to match the DNS friction coefficient. As anticipated, the reduced viscous suppression of eddies reduces the y^+ range of the viscosity-dominated flow regime. Though this case is less accurate than the others, it is noteworthy that a useful degree of predictive capability is obtained when standalone ODT is implemented as an effectively one-parameter model. In fact, fluctuation statistics for this case are only slightly less accurate than the results shown in Figs. 9 and 10.

Coupling ODT to LES requires the specification of the maximum eddy length, $L_{\max}$. This value determines the length of the overlap region (as illustrated in Fig. 21). It corresponds physically to the largest length scale captured by ODT, and should also correspond approximately to the smallest length scales resolved by the LES. Thus, one can also think of an overlap region of length scales in which both ODT and LES models are active.

To determine the appropriate value of $L_{\max}$, a simple parametric sensitivity study was performed. Figure 29 illustrates the results of this exercise for flow at $Re_\tau = 600$. Four different simulations were performed, keeping all other values and conditions constant except for the value of $L_{\max}$. A large change is seen as $L_{\max}$ is increased from $2\Delta Y$ to $3\Delta Y$, but very little difference is seen as its value is increased from $3.5\Delta Y$ to $4\Delta Y$. These results confirm our intuition that this value should correspond approximately to $4\Delta Y$ based on the resolution limitations of the numerical mesh. For all other calculations shown in this section, we use the value $L_{\max} = 3.5\Delta Y$.

The last issue of importance here is to determine the numerical resolution required by the ODT mesh. Figure 30 shows the sensitivity of the near-wall mean velocity profiles to ODT grid resolution at $Re_\tau = 1200$. At this Reynolds number, a value of N_{ODT} equal to 64 corresponds to an ODT near-wall mesh thickness of approximately 1.2 wall units (y^+). These results suggest that an ODT resolution of about $\Delta y^+ = 1$ is sufficient to achieve grid-independent results. Thus, for all subsequent calculations, the ODT mesh was chosen to satisfy this criterion.

Table 1 summarizes calculations performed and discussed here as a test of the current ODT/LES coupled model. In each of these runs, the values of C, Z, α, and $L_{\max}$ were constant and unchanged from the values specified as above. For cases E and F, the LES grid in the wall-normal direction was stretched using a constant geometric multiplier in order to obtain the desired near-wall grid thickness.

All calculations were performed on single-processor SGI workstations with run times varying from several hours for the lower-Reynolds-number flows to several days for the highest-Reynolds-number flows. However, extensive optimization of the code and model algorithms has not yet been attempted.

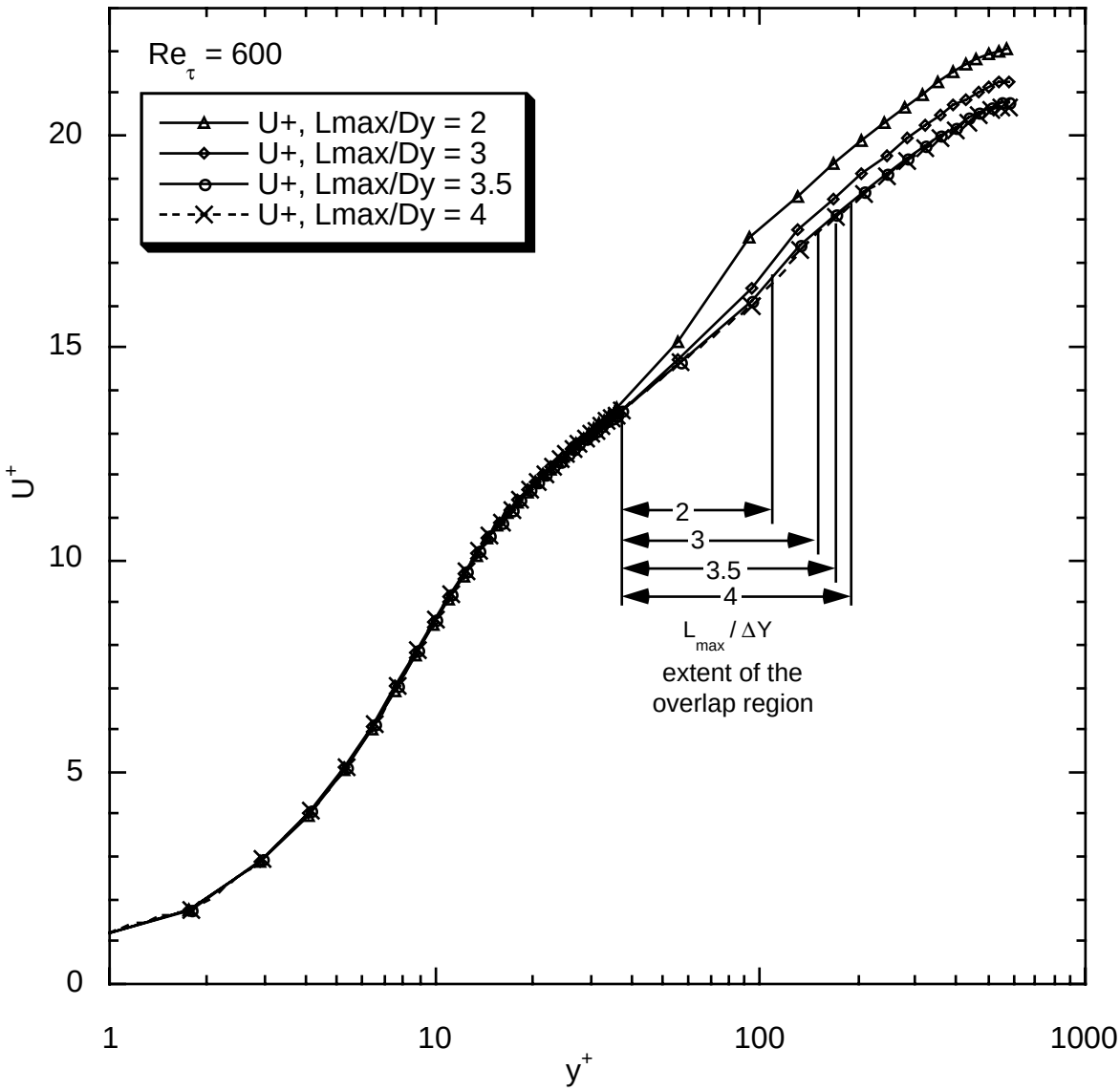

Figure 29. Sensitivity of the near-wall mean velocity profiles to different values of L_{max}.

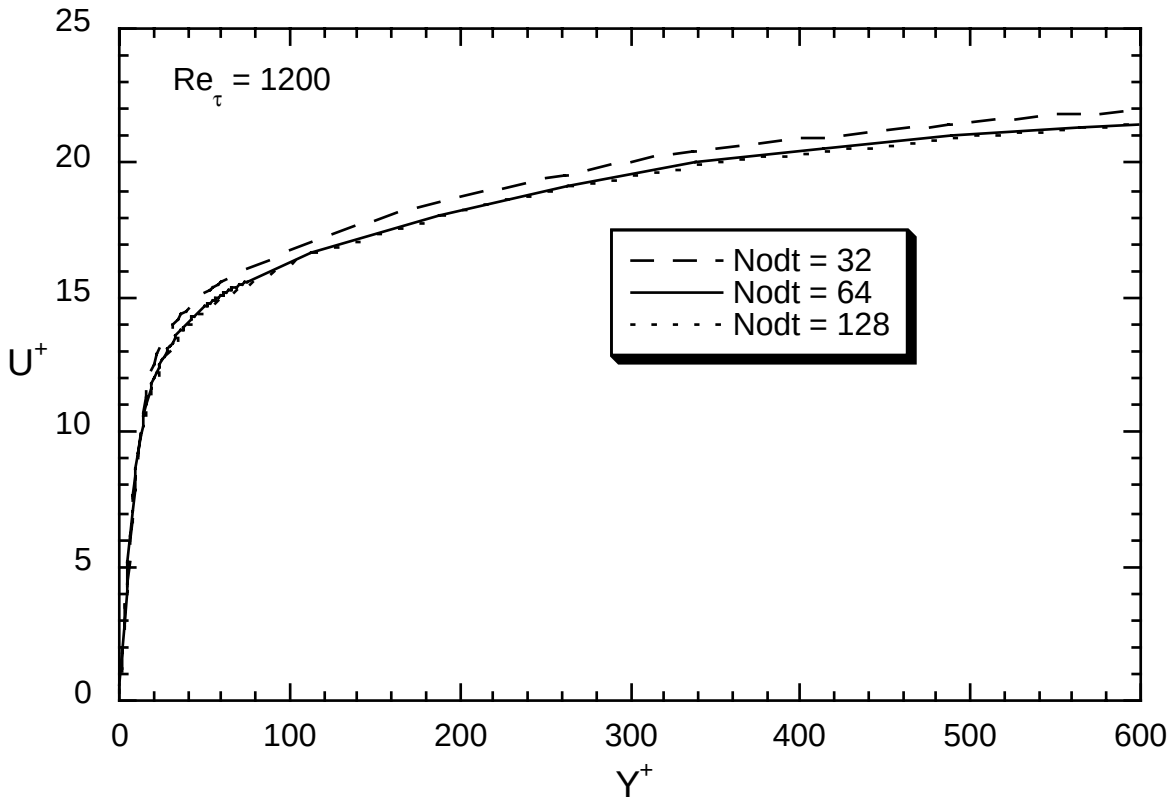

Figure 30. Sensitivity of the near-wall mean velocity profiles to ODT grid resolution.

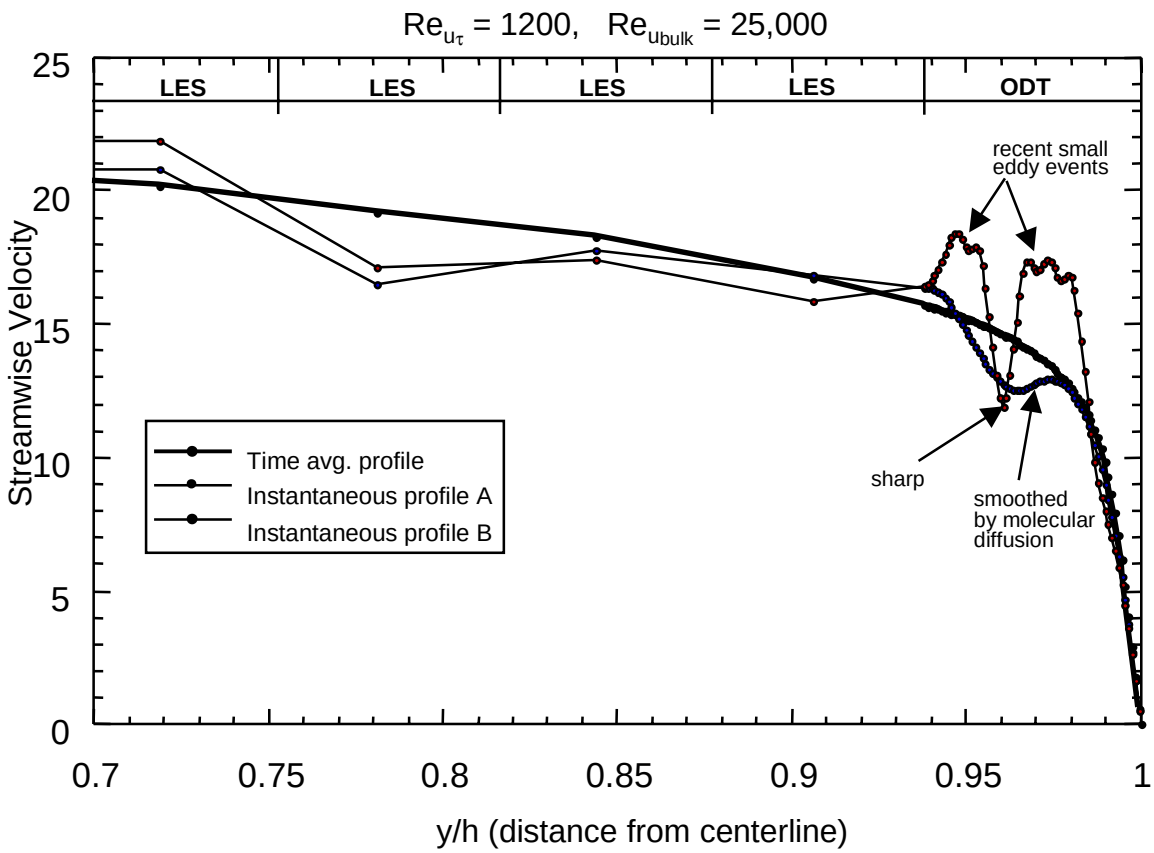

Figure 31. Near-wall mean and sample instantaneous velocity profiles, normalized by u_τ.

Case	Re_τ	Re	N_{ODT}	$\Delta y^+_{\mathrm{ODT}}$	N_x	N_y	N_z
A	395	7010	24	1.03	32	32	32
B	600	11236	32	1.17	32	32	32
C	1200	24668	64	1.17	32	32	32
D	2400	54312	128	1.17	32	32	32
E	4800	117166	128	1.15	32	48*	32
F	10000	262133	100	1.02	48	64*	48

*Grid was stretched to produce a finer resolution near the wall.

Table 1. Computed cases.

Figure 31 helps illuminate the dynamics of the coupled ODT/LES model by showing near-wall mean and instantaneous velocity profiles for an example calculation at $Re_\tau = 1200$. In contrast to the smoothly varying time-averaged profile that is shown, instantaneous profiles are highly irregular. Of particular note are the wrinkling effects of eddy events on the velocity profiles in the ODT inner region. At the particular instant shown, the effects of both large and small eddy events can be clearly seen. Furthermore, the smoothing effect of molecular processes over time can be seen and contrasted to the sharp gradients imposed by recent eddy events.

Figure 32 provides a summary illustration of model results for the mean velocity profiles over the Reynolds-number range indicated in Table 1. For cases A and B, the DNS data of Moser *et al.* (1999) are available and are used for direct comparison. For all cases, the inner law ($u^+ = y^+$) and a commonly accepted log law ($u^+ = 2.44 \ln(y^+) + 5.2$) are also plotted for comparison. Data symbols are used to denote ODT/LES node-point values in order to highlight the increased resolution of the model in the ODT domain.

At all Reynolds numbers, the simulations produce a physically realistic viscous sublayer smoothly transitioning through the buffer zone into a log layer. At the edge of the overlap region (between the second and third LES nodal values), a slight rise in the mean profile can be noticed in the lower-Reynolds-number cases. This is likely due to imperfect transitioning from ODT-based modeling of the turbulent transport to the LES modeling in the overlap region - an aspect that is likely to improve with model refinement. At the highest Reynolds numbers (cases E and F), the mean profile in the LES region above the ODT domain is

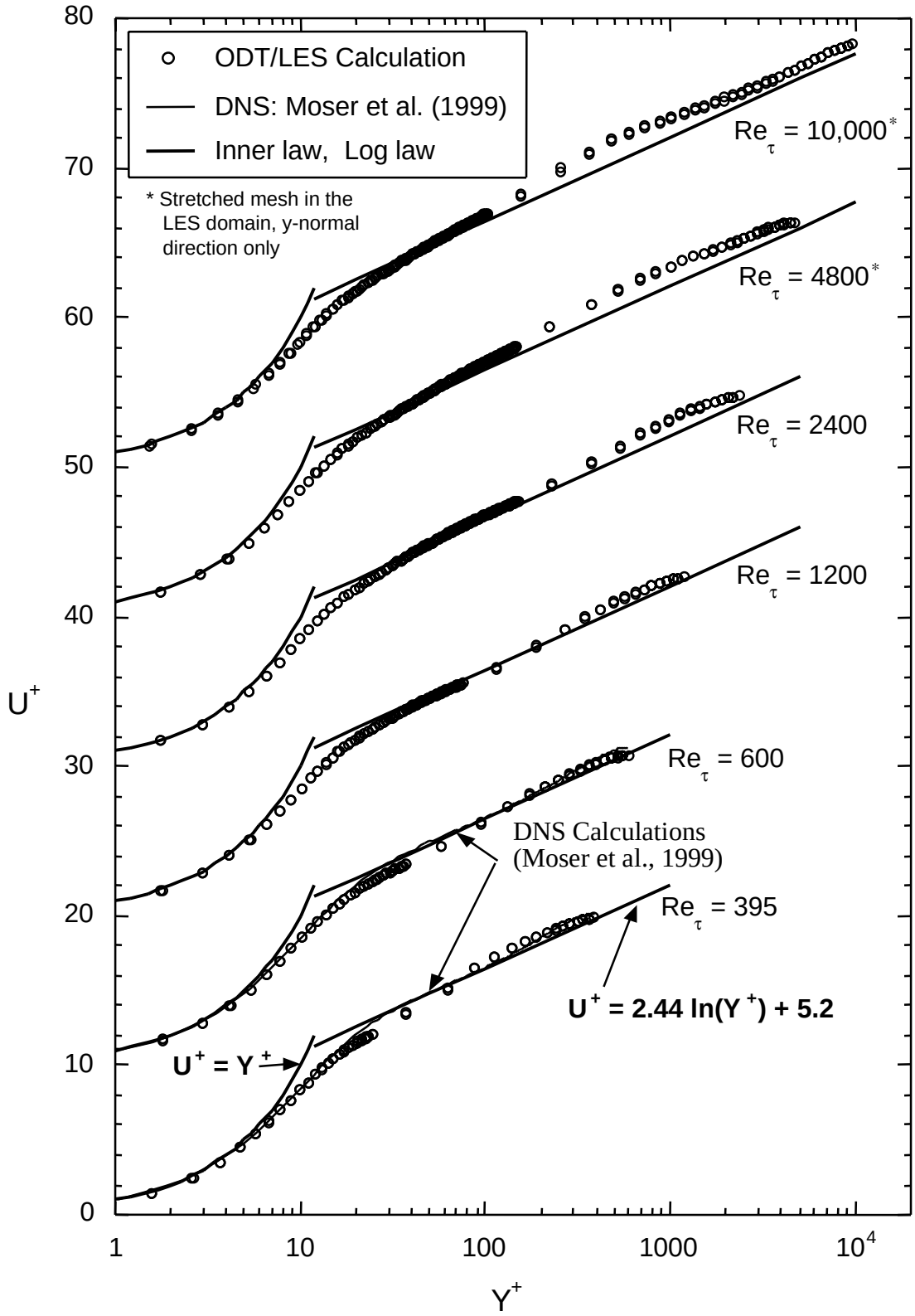

Figure 32. Semilog plot of ODT/LES mean velocity profiles for a range of Reynolds numbers. Successive profiles are vertically displaced for clarity. Pairs of overlapping symbols reflect the folding of computed profiles for the two channel walls onto a single profile.

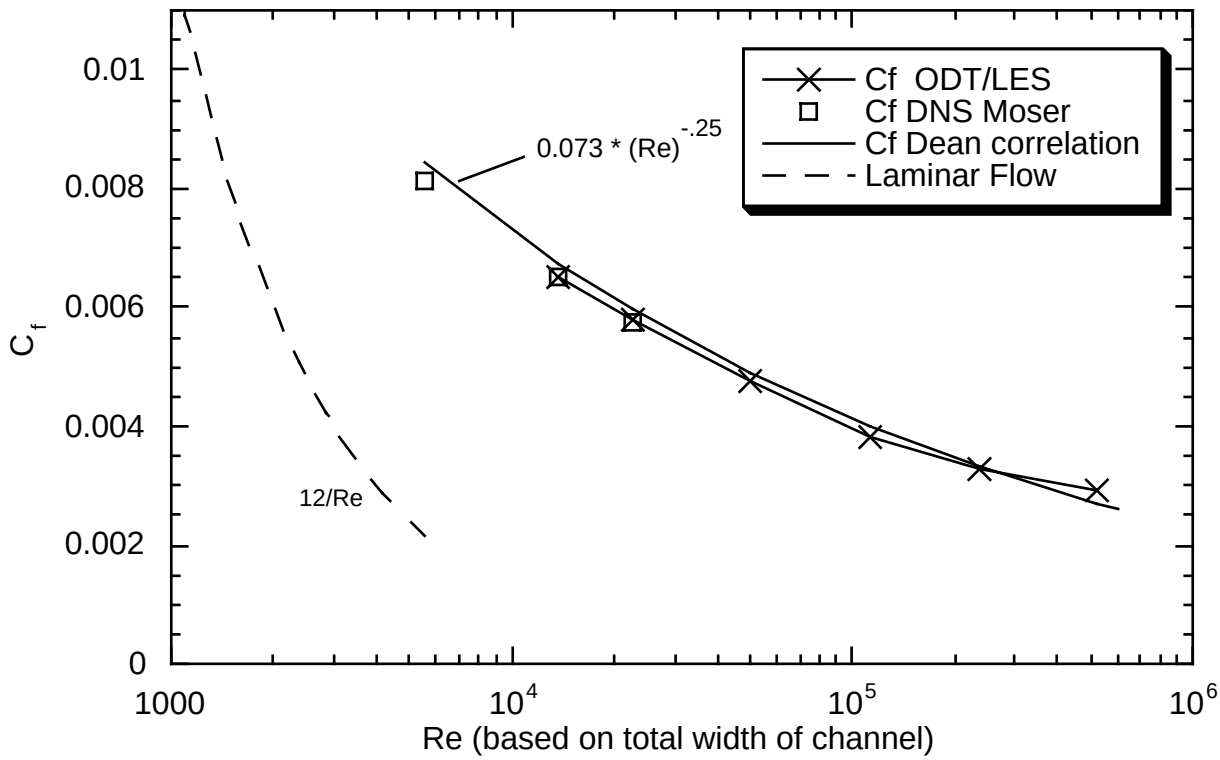

Figure 33. ODT/LES computed friction coefficient as a function of Reynolds number.

somewhat high. It is possible that this is due to the stretched grid near the wall, but it may also reflect a combination of underresolved LES effects coupled with imperfections in the overlap-region transition to the ODT near-wall domain. Further investigation will be needed to better understand the performance of the coupled model at these higher Reynolds numbers. Overall, the coupled ODT/LES model performs remarkably well at predicting the mean velocity profiles for this flow and compares very favorably with other recent work in this area (e.g., Nikitin *et al.* 2000, Kravchenko *et al.* 1996, Piomelli 1993).

Figure 33 is a semilog plot of the friction factor as a function of Reynolds number. The ODT/LES results, extending over a wide range of the bulk-flow Reynolds number, are in good agreement with DNS and experimental results.

Figures 34-43 are plots of RMS velocity profiles, normalized by u_τ. These results are important because they illustrate near-wall dynamic information that cannot be obtained from low-order RANS-based models. The dynamic fluctuations that are reflected in the RMS velocity profiles are also important to multiphysics applications where physical processes such as heat transfer and chemical reactions are strongly affected.

Note that the wall-normal RMS velocities shown in these figures are computed from the ODT advecting-velocity profile $V_2(y,t)$, not the instantaneous wall-normal ODT velocity-component profile v_2. As explained previously, this is because the instantaneous wall-normal ODT component is treated here as simply a measure of subgrid kinetic energy in the model, and does not reflect local continuity constraints.

Figures 34 and 35 compare ODT/LES computed RMS velocity profiles at $Re_\tau = 395$ with those of the DNS calculations of Moser *et al.* (1999). Figure 34 shows the entire channel halfwidth whereas Fig. 35 focuses only on the narrow ODT inner region.

Near the wall, the ODT/LES prediction of the peak in the $u_{\rm rms}$ profile is remarkably close to the DNS considering the relatively poor comparison seen in the standalone ODT results presented in Sec. 4.2 (see Fig. 9). This reflects the influence of the LES coupling to the inner-region ODT. In the LES domain, the $u_{\rm rms}$ profile is somewhat elevated as it comes closer to the wall. This is a symptom noted by many others of an underresolved LES near the wall (e.g., Kravchenko *et al.* 1996).

Near the wall, the relative magnitudes of the predicted $w_{\rm rms}$ and $v_{\rm rms}$ profiles are correct, although somewhat lower than the DNS values. In the ODT inner region, however, the profile for $v_{\rm rms}$ is very close to the DNS values. In both cases, there is a discontinuity in slope at the ODT/LES interface reflecting the abrupt jump from a finely resolved ODT mesh to the much coarser LES mesh. Overall, the magnitudes and shapes of these profiles are not strongly in error and in fact are considered quite good considering the nature of the model.

Figures 36 and 37 show results at $Re_\tau = 600$ that are analogous to those given in Figs. 34 and 35 for $Re_\tau = 395$. The only difference of note is that the ODT/LES profile for $v_{\rm rms}$ is not quite as close to the DNS values. (The DNS values are somewhat elevated.)

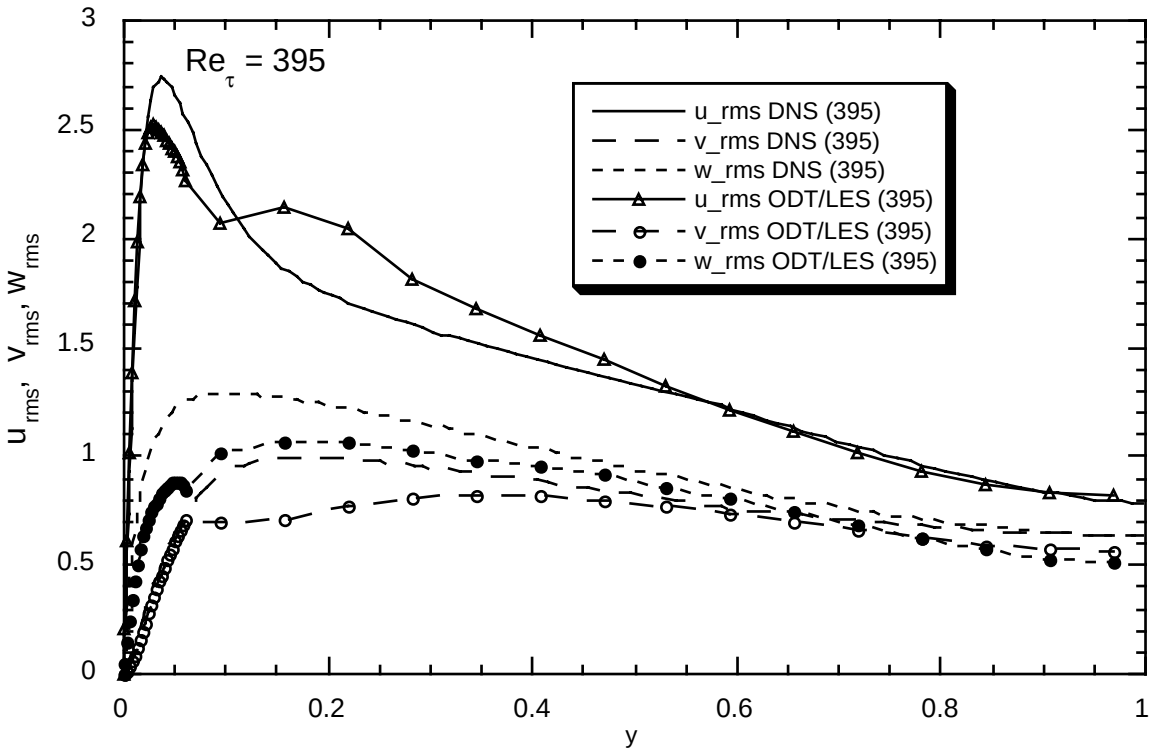

Figure 34. DNS versus ODT/LES RMS velocity profiles for $Re_\tau = 395$.

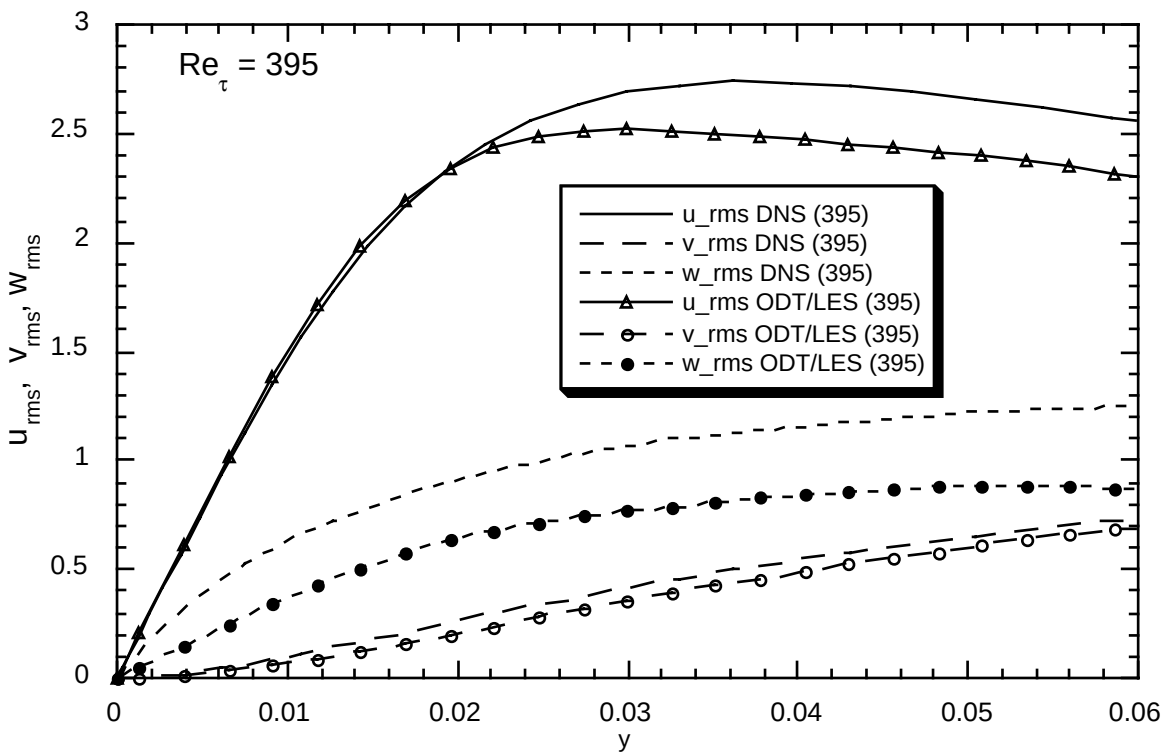

Figure 35. DNS versus ODT/LES RMS velocity profiles in the near-wall region for $Re_\tau = 395$.

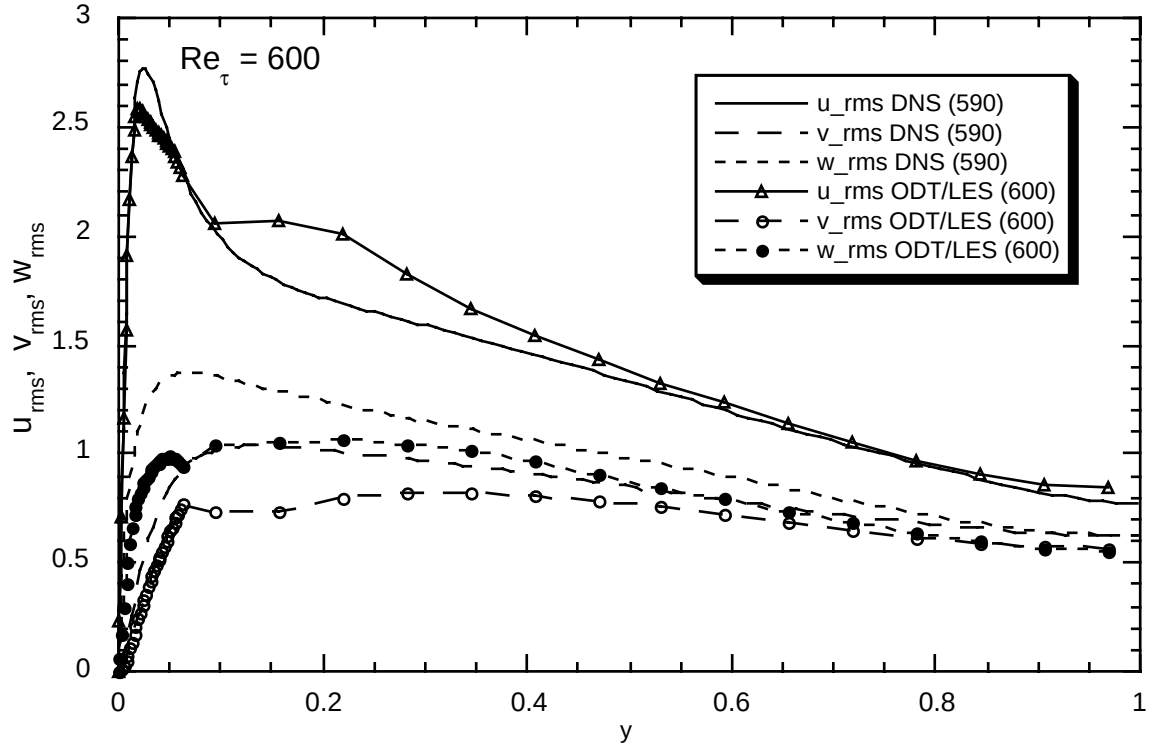

Figure 36. DNS versus ODT/LES RMS velocity profiles for $Re_\tau = 600$.

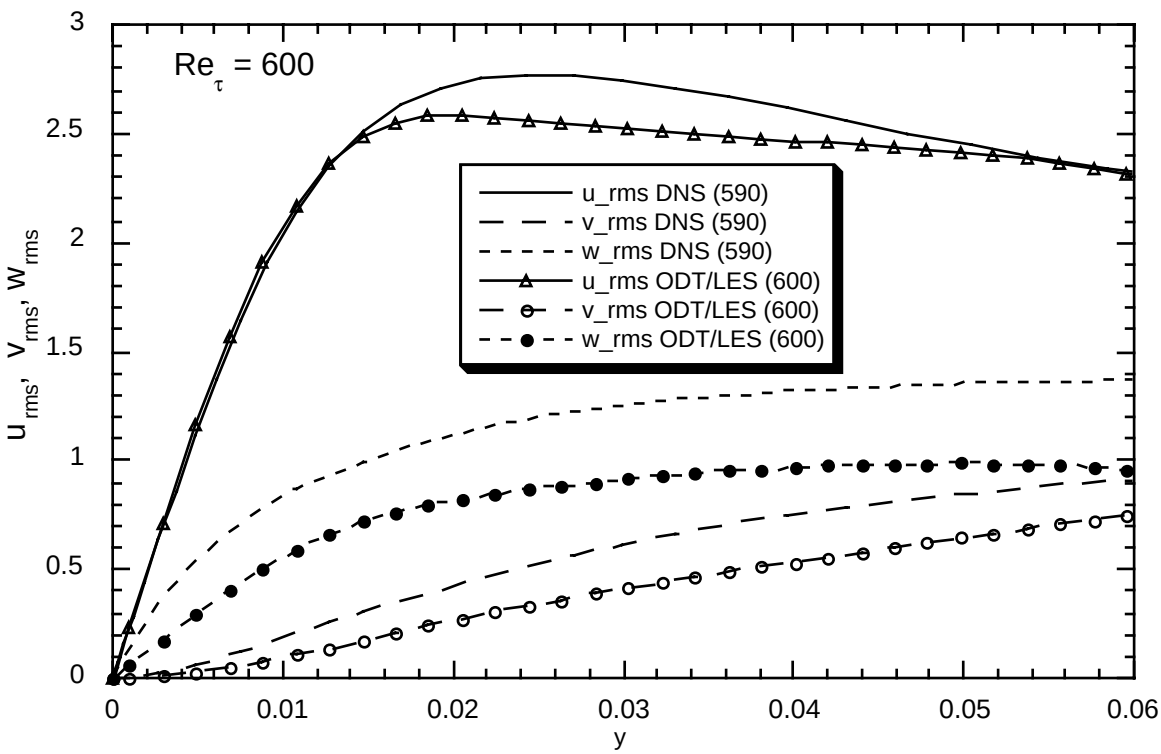

Figure 37. DNS versus ODT/ LES RMS velocity profiles in the near-wall region for $Re_\tau = 600$.

Figures 38 and 39 show the ODT/LES computed $u_{\rm rms}$ profiles for the higher-Reynolds-number flows (cases C through F). Away from the very-near-wall region, cases C and D ($Re_\tau = 1200$ and 2400) are nearly indistinguishable. Although not directly compared here, they would also compare very closely to cases A and B. This reflects the fact that cases A through D were each computed on the same uniform LES mesh with the same ODT/LES overlap region. Only in the very-near-wall region, where behavior scales on inner variables, would differences be expected (Wei & Willmarth 1989). This is exactly what is shown in Fig. 39, where we see that the $u_{\rm rms}$ profiles peak closer and closer to the wall as Re_τ increases.

For cases E and F ($Re_\tau = 4800$ and 10,000) the LES mesh has been refined and stretched in the wall-normal direction (and also refined in the other directions for Case F). Figure 38 shows that in each case, the LES profile of $u_{\rm rms}$ is somewhat elevated as it comes closer to the wall, and drops down as it transitions to the ODT inner region. However, the more highly elevated near-wall values of Case F imply that for better fidelity, the ODT domain would need to extend farther out into the flow field. This suggests that in general, the required height of the ODT inner region may not scale only on inner variables. These results highlight the need to explore the high-Re cases more thoroughly in future work.

Figures 40-43 show predicted $v_{\rm rms}$ and $w_{\rm rms}$ profiles for the higher-Reynolds-number flows (cases C through F). These results suggest similar conclusions to those drawn by looking at Figs. 38 and 39. Profiles for E and F show symptoms of being inadequately resolved in the ODT/LES overlap region, while results for cases C and D are very similar to each other and to cases A and B.

6.2 Cost/Performance Results and Extrapolation to Engineering Problems

An important issue with development of ODT as a near-wall LES subgrid model is the relative computational cost of using the model. The approach is only attractive if the model is both affordable and accurate. To assess this aspect of the model, some preliminary timing results are presented and discussed here, particularly as they relate to scaling up to bigger problems and higher-Reynolds-number flow.

As a means of comparing results from different runs, a computational cost figure-of-merit '$F_{\rm CPU}$' has been computed for each case. $F_{\rm CPU}$ is defined in such a way as to normalize out differences in each of the runs that would tend to obscure a direct comparison of timings.

The method for computing $F_{\rm CPU}$ is as follows. First, adjustments to the ODT cpu time per LES time step are made so as to estimate this value for runs at a constant CFL of 0.5, and a fractional acceptance rate of 0.05. The ODT CPU time per LES time step is then divided by the total number of ODT nodes in the calculation. These values are plotted in Fig. 44. Because of the nature of the estimation process, these results can only be taken as indicative of a general trend. However, even with a very conservative extrapolation of these

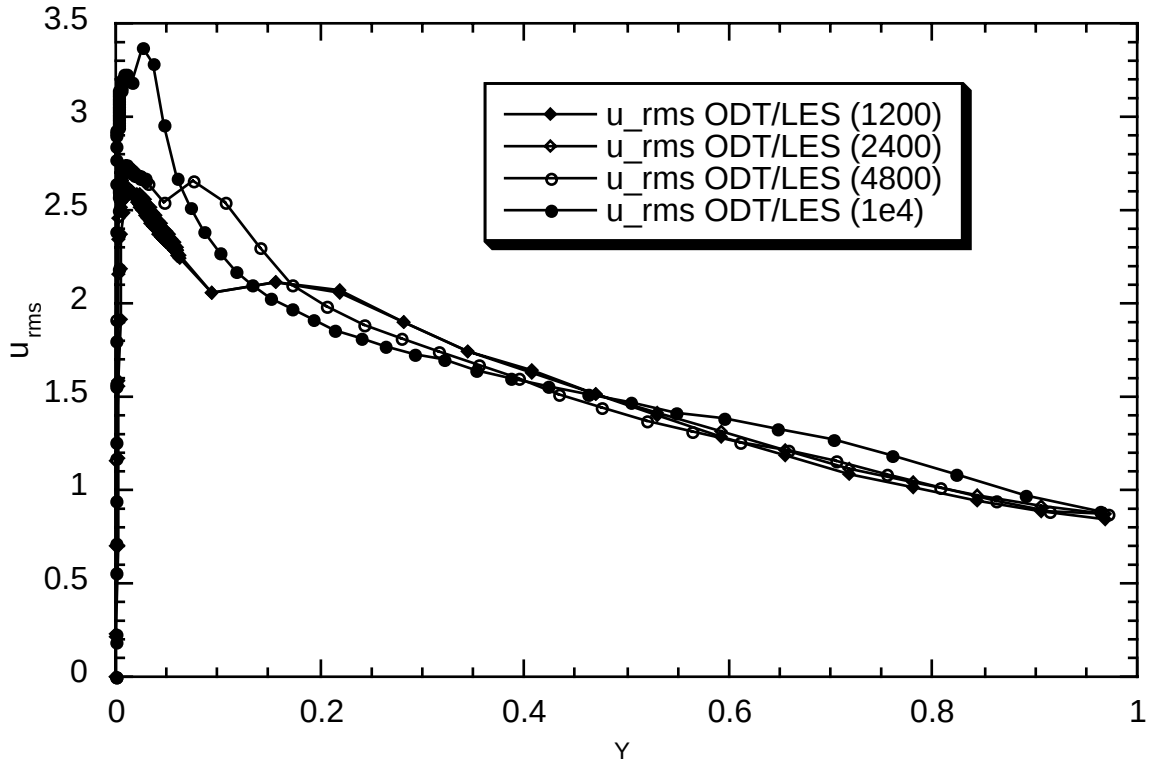

Figure 38. ODT/LES profiles of streamwise RMS velocity for higher-Reynolds-number flows.

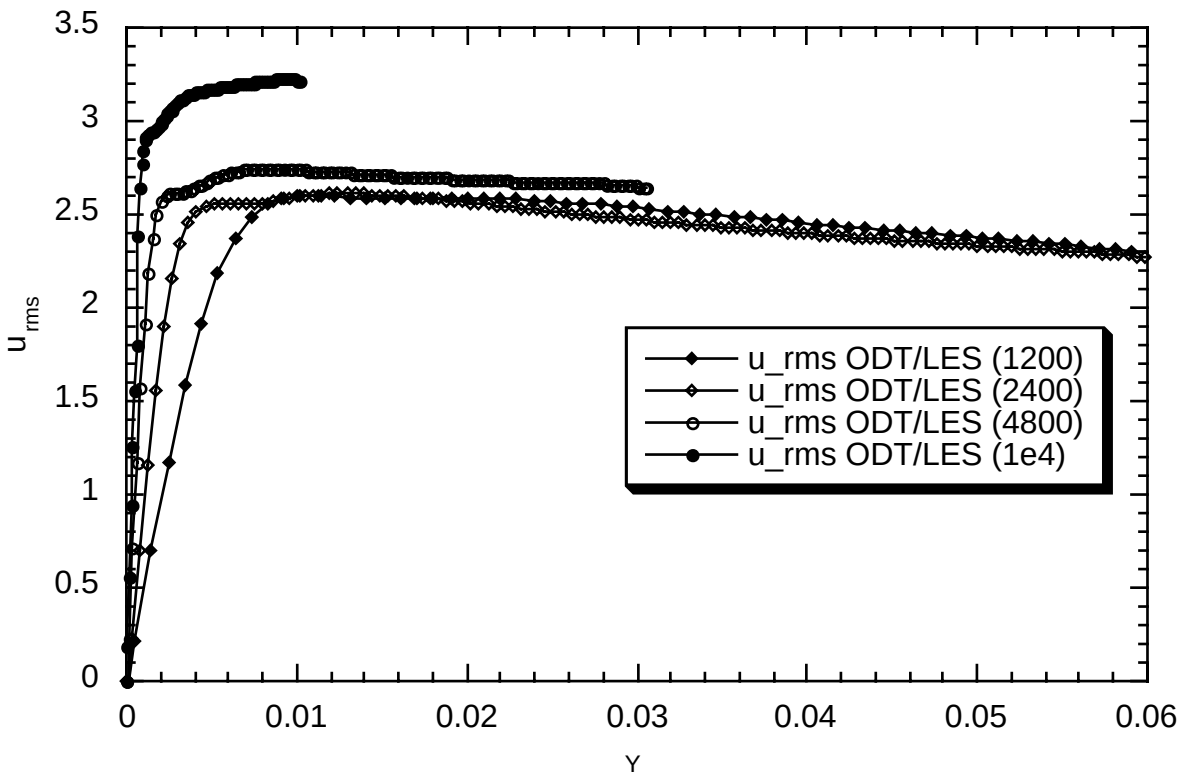

Figure 39. ODT/LES profiles of streamwise RMS velocity in the near-wall region for higher-Reynolds-number flows.

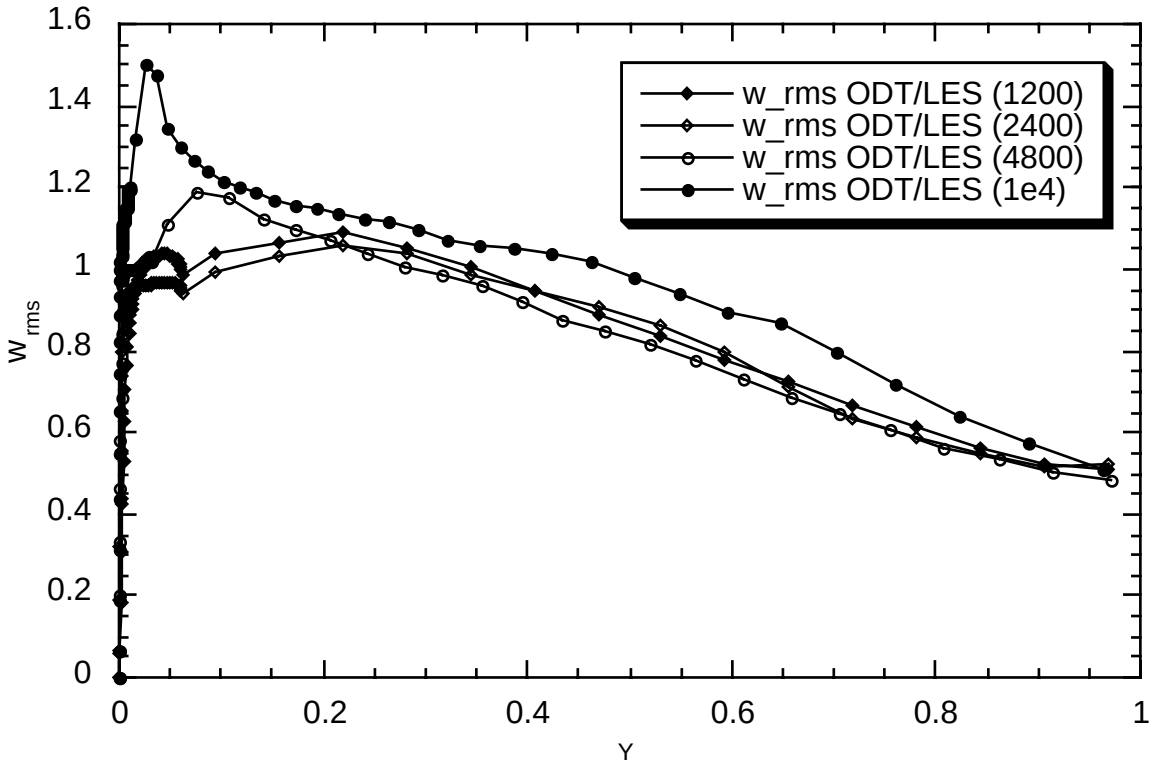

Figure 40. ODT/ LES profiles of spanwise RMS velocity for higher-Reynolds-number flows.

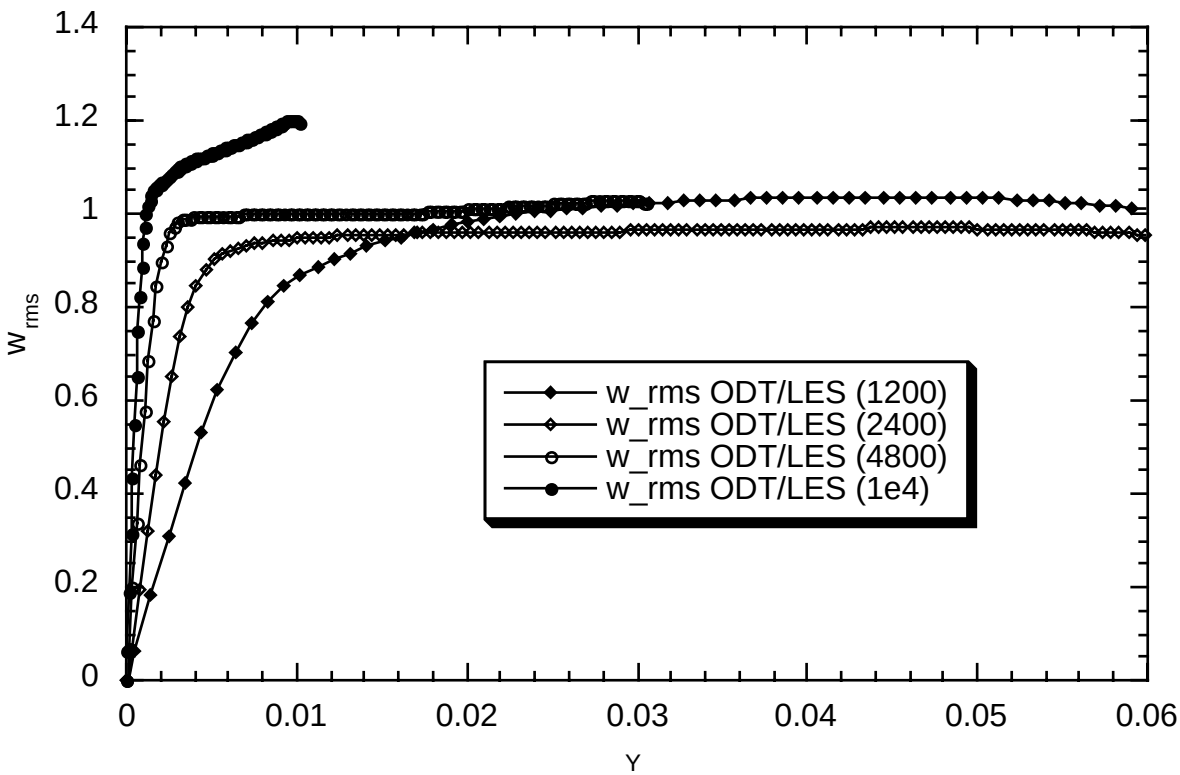

Figure 41. ODT/LES profiles of spanwise RMS velocity in the near-wall region for higher-Reynolds-number flows.

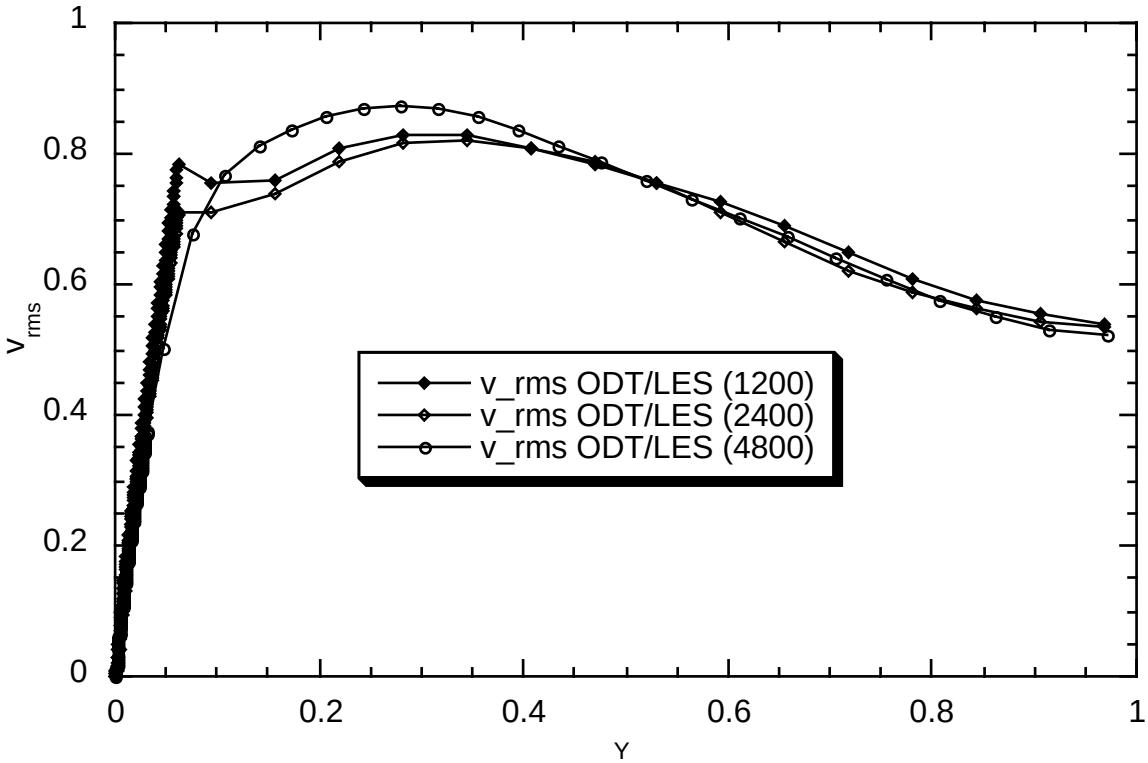

Figure 42. ODT/LES profiles of wall-normal RMS velocity for higher-Reynolds-number flows.

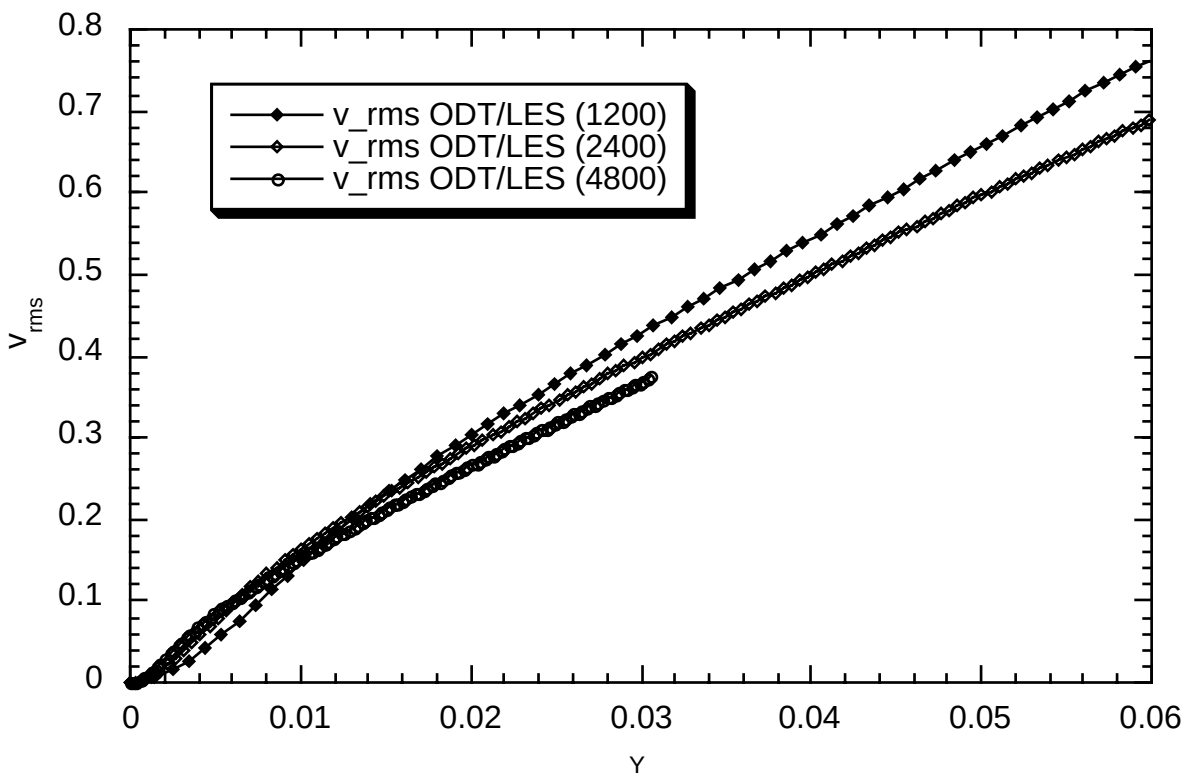

Figure 43. LES/ODT wall-normal RMS velocity profiles in the near-wall region for higher-Reynolds-number flows.

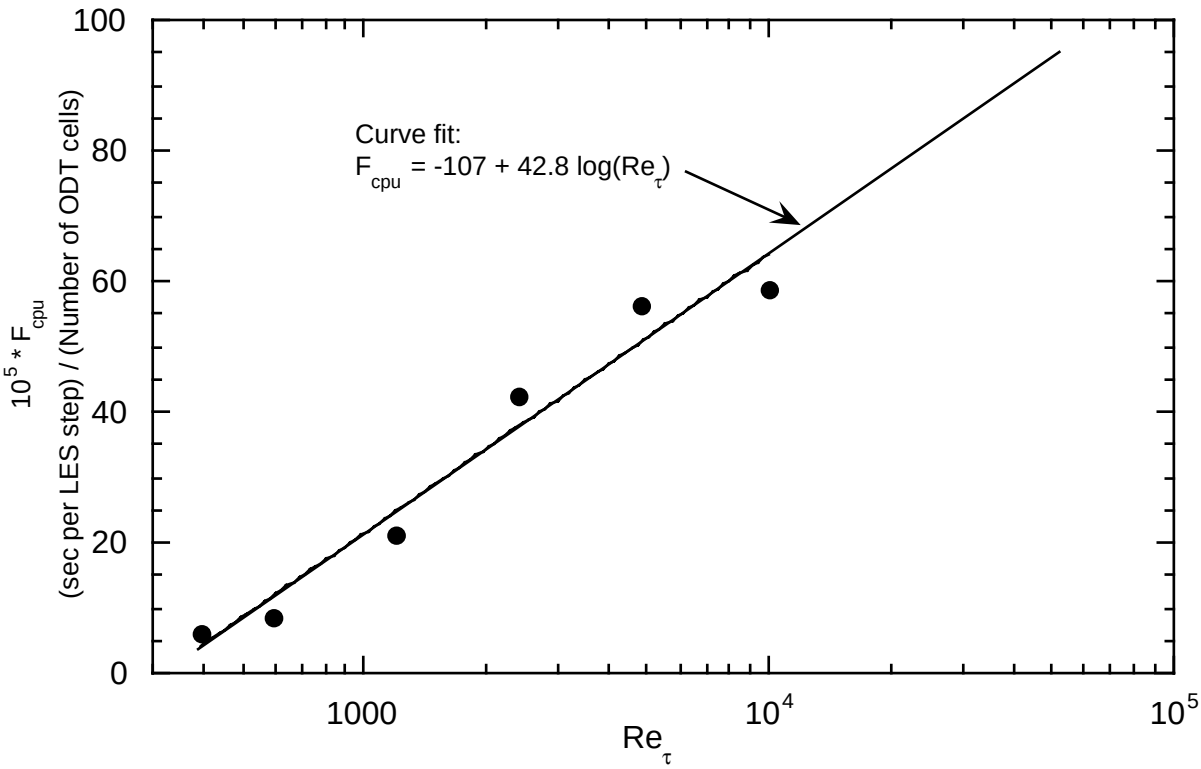

Figure 44. Normalized ODT subgrid-model CPU cost as a function of Reynolds number.

trends, the results indicate that the cost per ODT node of going from $R_\tau = 10^4$ to $R_\tau = 10^5$ would increase by less than a factor of 2.

When using these results to estimate the cost of using ODT as a near-wall model, two additional factors must be recognized. First, the cost of using ODT as a near-wall model scales with the surface area that needs to be modeled. Thus, the particular geometry of interest affects this estimate. Second, the cost of doing the LES portion of the problem scales differently with problem size than the ODT part. This scaling will depend strongly on the numerical and parallel algorithms used in the LES code, but would not be expected to scale as favorably as does the ODT part of the problem. Thus, the bigger the overall LES problem, the smaller the relative cost of doing the ODT part of the problem compared to the LES portion of the problem.

7 Discussion

The complexity of turbulent flow renders exact numerical solution unaffordable for cases of practical interest and greatly complicates efforts to develop reliable approximations. The approach introduced here is is an attempt to develop a turbulence model based on physical principles that, though empirical, are hopefully robust. To achieve this, the mixing-length concept is applied on a local time-resolved basis, rather than applying it to averaged quantities. It is hoped that this strengthens the tie between the physical concept and its formal implementation within the model.

By focusing on this attribute of the model, the connection between unfamiliar elements of the model and more familiar turbulence modeling concepts has been emphasized. The eddy events within ODT provide a concise representation of turbulence production, transport, energy-transfer, and length-scale-reduction mechanisms. The feedback resulting from the dependence of the governing random process on flow and fluid-property profiles, and modification of those profiles by eddy implementation, leads to a flow evolution process that more faithfully emulates continuum motion than might be expected at first glance. The key advantage of this construct is that it enables a 1D formulation that is computationally affordable as a subgrid model as well as a standalone tool.

Representative standalone applications have been presented that indicate the potential performance characteristics of ODT as a near-wall subgrid closure for LES. These examples address relevant energy-conversion processes, including turbulent-kinetic-energy production, dissipation, redistribution among velocity components, and conversion to or from gravitational potential energy. The complexity of the couplings among shear and gravitational forcings, boundary conditions, and fluid-property evolution (e.g., diffusive mixing of density fluctuations) result in turbulence scaling properties that defy analysis, yet are reproduced

by ODT. These results indicate that the relevant couplings are represented in ODT with a fidelity not previously achieved, short of multidimensional simulation.

To demonstrate the performance of ODT as a subgrid model for LES, ODT has been implemented as a near-wall momentum closure. A variety of physical modeling and numerical implementation issues have been addressed in this regard. Computed results have been compared to DNS of channel flow. Both the predictive capability and the computational efficiency of this formulation indicate the likelihood that ODT near-wall momentum closure will be a practical, cost-effective contribution to the fidelity of turbulence computations.

Possible extensions of the work reported here fall in two categories: incorporation of more physics into ODT and broadening of the subgrid modeling role of ODT within LES. Additional physics that may be incorporated into ODT includes nonBoussinesq variable-density effects, compressibility, and multiphase flow. New subgrid applications under consideration are bulk-flow momentum closure and closures for mixing and combustion. It may be cost-effective to implement the latter in a Lagrangian framework, using ODT to simulate the fine structure of a flame brush that is tracked on the LES grid. Investigation of some of these possibilities has begun.

References

Betts, P. L. & Bokhari, I. H. 1996 Experiments on turbulent natural convection in a tall air cavity, in: Fifth ERCOFTAC workshop on refined flow modelling, Chatou, France.

Callen, H. B. 1960 *Thermodynamics.* Wiley.

Ciofalo, M. 1994 Large-eddy simulation: a critical survey of models and applications. *Adv. Heat Transf.* **25**, 321-419.

Cioni, S., Ciliberto, S. & Sommeria, J. 1997 Strongly turbulent Rayleigh-Beńard convection in mercury: comparison with results at moderate Prandtl number. *J. Fluid Mech.* **335**, 111-140.

Dreeben, T. D. & Kerstein, A. R. 2000 Simulation of vertical slot convection using 'one-dimensional turbulence.' *Int. J. Heat Mass Transf.* **43**, 3823-3834.

Dukowicz, J. K. & Dvinsky, A. S. 1992 Approximate factorization as a high-order splitting for the implicit incompressible flow equations. *J. Comp. Phys.* **102**, 336-347.

Germano, M., Piomelli, U., Moin, P. & Cabot, W. 1991 A dynamic subgrid-scale eddy viscosity model. *Phys. Fluids* A **3**, 1760-1765.

Ghosal, S., Lund, T. S., Moin, P. & Akselvoll, K. 1995 A dynamic localization model for large-eddy simulation of turbulent flows. *J. Fluid Mech.* **286**, 229-255.

Goldstein, R. J., Chiang, H. D. & See, D. L. 1990 High-Rayleigh-number convection in a horizontal enclosure. *J. Fluid Mech.* **213**, 111-126.

Harlow, F. H. & Welch, J. E. 1965 Numerical calculation of time-dependent viscous incompressible flow of fluid with free surface. *Phys. Fluids* **8**, 2182-2189.

Kerstein, A. R. 1991 Linear-eddy modelling of turbulent transport. Part 6. Microstructure of diffusive scalar mixing fields. *J. Fluid Mech.* **231**, 361-394.

Kerstein, A. R. 1999 One-dimensional turbulence: Model formulation and application to homogeneous turbulence, shear flows, and buoyant stratified flows. *J. Fluid Mech.* **392**, 277-334.

Kerstein, A. R. & Dreeben, T. D. 2000 Prediction of turbulent free shear flow statistics using a simple stochastic model. *Phys. Fluids* **12**, 418-424.

Kraichnan, R. H. 1962 Turbulent thermal convection at arbitrary Prandtl number. *J. Fluid Mech.* **5**, 1374-1389.

Kravchenko, A. G., Moin, P. & Moser, R. 1996 Zonal embedded grids for numerical simulations of wall-bounded turbulent flows. *J. Comp. Phys.* **127**, 412-423.

Lilly, D. K. 1992 A proposed modification of the Germano subgrid-scale closure model. *Phys. Fluids* A **4**, 633-635.

Lorenz, E. N. 1955 Available potential energy and the maintenance of the general circulation. *Tellus* **7**, 157-167.

Moser, R. D., Kim, J. & Mansour, N. N. 1999 Direct numerical simulation of turbulent channel flow up to $Re_\tau = 590$. *Phys. Fluids* **11**, 943-945.

Moser, R. D., Rogers, M. M. & Ewing, D. W. 1998 Self-similarity of time-evolving plane wakes. *J. Fluid Mech.* **367**, 255-289.

Niemela, J. J., Skrbek, L., Sreenivasan, K. R. & Donnelly, R. J. 2000 Turbulent convection at very high Rayleigh numbers. *Nature* **404**, 837-840.

Nieuwstadt, F. T. M. & Versteegh, T. A. M. 1997 DNS of natural convection between two vertical differentially heated walls, in: Eleventh Symposium on Turbulent Shear Flows, Grenoble, France.

Nikitin, N. V., Nicoud, F., Wasistho, B., Squires, K. D. & Spalart, P. R. 2000 An approach to wall modeling in large-eddy simulations. *Phys. Fluids* **12**, 1629-1632.

Patankar, S. V. 1981 *Numerical Heat Transfer and Fluid Flow.* Hemisphere.

Petukhov, B. S. & Polyakov, A. F. 1988 *Heat Transfer in Turbulent Mixed Convection.* Hemisphere.

Piomelli, U. 1993 High Reynolds number calculations using the dynamic subgrid-scale stress model. *Phys. Fluids* A **5**, 1484-1490.

Pope, S. B. 2000 *Turbulent Flows.* Cambridge.

Rogers, M. M. & Moser, R. D. 1994 Direct simulation of a self-similar turbulent mixing layer. *Phys. Fluids* **6**, 903-923.

Schumann, U. 1973 Doctoral dissertation, Technical Univ. of Karlsruhe, Germany. (Summarizing English transl. by M. Love, Queen Mary College, University of London, 1974)

Schumann, U. 1975 Subgrid scale model for finite difference simulations of turbulent flows in plane channels and annuli. *J. Comp. Phys.* **18**, 376-404.

Smagorinsky, J. 1963 General circulation experiments with the primitive equations: Part I. The basic experiment. *Mon. Weather Rev.* **91**, 99-164.

Spalart, P., Moser, R. & Rogers, M. 1991 Spectral methods for the Navier-Stokes equations with one infinite and two periodic directions. *J. Comp. Phys.* **96**, 297-324.

Van Kan, J. 1986 A second order accurate pressure-correction scheme for viscous incompressible flow. *SIAM J. Sci. Stat. Comp.* **7**, 870-891.

Versteegh, T. A. M. & Nieuwstadt, F. T. M. 1999 A direct numerical simulation of natural convection between two infinite vertical differentially heated walls; scaling laws and wall functions. *Int. J. Heat Mass Transf.* **42**, 3673-3693.

Wei, T. & Willmarth, W. W. 1989 Reynolds-number effects on the structure of a turbulent channel flow. *J. Fluid Mech.* **204**, 57-95.

Wunsch, S. & Kerstein, A. R. 2001 A model for layer formation in stably stratified turbulence. *Phys. Fluids*, in press.

Initial Distribution

External Distribution:

1 Jeff Baggett
Department of Mathematics
1016 Cowley Hall
University of Wisconsin
La Crosse, WI 54601

1 Bill Cabot
L-022
Lawrence Livermore National Laboratory
Livermore, CA 94550-9234

1 Shi-Yi Chen
Los Alamos National Laboratory
MS B213 T-13: Complex Systems
Los Alamos, NM 87545

1 Paul Dimotakis
MS 301-46
Graduate Aeronautical Laboratories
California Institute of Technology
Pasadena, CA 91125

1 César Dopazo
Área de Mecánica de Fluidos
Deparatmento de Ciencia y Tecnología de Materiales y Fluidos
Centro Politécnico Superior
Universidad de Zaragoza
María de Luna 3
50015 Zaragoza
Spain

1 Thomas Dreeben
Osram Sylvania
71 Cherry Hill Drive
Beverly, MA 01915

1 Jonathan Dursi
c/o ASCI FLASH Center
5640 South Ellis, RI 468
Chicago, IL 60637

1 Steven Frankel
School of Mechanical Engineering
Purdue University
West Lafayette, IN 47907-1077

1 Peyman Givi
Department of Mechanical and Aerospace Engineering
State University of New York at Buffalo
Buffalo, NY 14260-4400

1 Rupert Klein
FB Mathematik & Informatik
FU-Berlin
Takustr. 7
14195 Berlin
Germany

1 Joe Klewicki
Department of Mechanical Engineering
University of Utah
Salt Lake City, UT 84112

1 George Kosály
Department of Mechanical Engineering
Box 352600
University of Washington
Seattle, WA 98195-2600

1 Tony Leonard
MS 301-46
Graduate Aeronautical Laboratories
California Institute of Technology
Pasadena, CA 91125

1 Andrew Majda
Courant Institute of Mathematical Sciences
New York University
251 Mercer Street
New York, NY 10012

1 Pat McMurtry
Department of Mechanical Engineering
University of Utah
Salt Lake City, UT 84112

1 Suresh Menon
School of Aerospace Engineering
Georgia Institute of Technology
Atlanta, GA 30332-0150

1 Jens Niemeyer
Max-Planck-Institut fuer Astrophysik
Karl-Schwarzschild-Str. 1
D-85748 Garching
Germany

1 Vebjorn Nilsen
Torrex Equipment Corporation
4771 Arroyo Vista
Livermore, CA 94550

1 Norbert Peters
Institut für Technische Mechanik
RWTH
Aachen
Germany

1 Jim Riley
Department of Mechanical Engineering
Box 352600
University of Washington
Seattle, WA 98195-2600

1 Robert Rosner
c/o ASCI FLASH Center
5640 South Ellis, RI 468
Chicago, IL 60637

1 Oleg Schilling
L-022
Lawrence Livermore National Laboratory
Livermore, CA 94550-9234

1 John Schmidt
Department of Chemical and Environmental Engineering
University of Arizona
Tucson, AZ 85721

1 Dave Stevens
L-103
Lawrence Livermore National Laboratory
Livermore, CA 94550-9234

1 Jost Wendt
Department of Chemical and Environmental Engineering
University of Arizona
Tucson, AZ 85721

Internal Distribution:

20	MS1111	R. Schmidt
20	MS9051	A. Kerstein
1	MS0316	S. Dosanjh
1	MS0321	W. Camp
1	MS0767	B. Boughton
1	MS0819	M. Christon
1	MS0825	F. Blottner
1	MS0825	K. Salari
1	MS0826	W. Hermina
1	MS0835	R. Cochran
1	MS0835	B. Hassan
1	MS0835	S. Kempka
1	MS0835	J. Peery
1	MS0835	C. Roy
1	MS0836	P. Desjardin
1	MS0836	E. Hertel, Jr.
1	MS0836	S. Tieszen
1	MS0841	T. Bickel
1	MS1111	J. Shadid
1	MS1111	T. Smith
1	MS1186	T. Mehlhorn
1	MS9042	C. Moen
1	MS9042	G. Evans
1	MS9051	W. Ashurst
1	MS9051	J. Chen
1	MS9051	T. Echekki
1	MS9051	J. Hewson
1	MS9051	L. Rahn
1	MS9051	S. Wunsch
1	MS0188	D. Chavez, LDRD Office
3	MS9018	Central Technical Files, 8940-2
1	MS0899	Technical Library, 4916
1	MS9021	Classification Office, 8511/Technical Library, MS0899, 4916
1	MS9021	Classification Office, 8511 for DOE/OSTI